COLD ATOM CONTROL WITH AN OPTICAL ONE-WAY BARRIER

by

ELIZABETH A. SCHOENE

A DISSERTATION

Presented to the Department of Physics
and the Graduate School of the University of Oregon
in partial fulfillment of the requirements
for the degree of
Doctor of Philosophy

December 2010

"Cold Atom Control with an Optical One-Way Barrier," a dissertation prepared by Elizabeth A. Schoene in partial fulfillment of the requirements for the Doctor of Philosophy degree in the Department of Physics. This dissertation has been approved and accepted by:

_____

Dr. Hailin Wang, Chair of the Examining Committee

_____

Date

Committee in charge: Dr. Hailin Wang, Chair
                               Dr. Daniel A. Steck, Research Advisor
                               Dr. Jens U. Nöckel
                               Dr. David M. Strom
                               Dr. Jeffrey A. Cina

Accepted by:

_____

Dean of the Graduate School

An Abstract of the Dissertation of

Elizabeth A. Schoene for the degree of Doctor of Philosophy

in the Department of Physics to be taken December 2010

Title: COLD ATOM CONTROL WITH AN OPTICAL ONE-WAY

 BARRIER

Approved: _____

Dr. Daniel A. Steck

The research presented in this dissertation aims to contribute to the field of atom optics via the implementation and demonstration of an all-optical one-way barrier for ^{87}Rb atoms—a novel tool for controlling atomic motion. This barrier—a type of atomic turnstile—transmits atoms traveling in one direction but hinders their passage in the other direction. We create the barrier with two laser beams, generating its unidirectional behavior by exploiting the two hyperfine ground states of ^{87}Rb. In particular, we judiciously choose the frequency of one beam to present a potential *well* to atoms in one ground state (the transmitting state) and a potential *barrier* to atoms in the other state (the reflecting state). The second beam optically pumps the atoms from the transmitting state to the reflecting state.

A significant component of the experimental work presented here involves generating ultra-cold rubidium atoms for demonstrating the one-way barrier. To this end, we have designed and constructed a sophisticated ^{87}Rb cooling and trapping apparatus. This apparatus comprises an extensive ultra-high vacuum system, four home-built, frequency-stabilized diode laser systems, a high-power Yb:fiber laser, a multitude of supporting optics, and substantial timing and control electronics. This system allows us to cool and trap rubidium atoms at a temperature of about 30 μK.

The results presented in this dissertation are summarized as follows. We successfully implemented a one-way barrier for neutral atoms and demonstrated its asymmetric nature. We used this new tool to compress the phase-space volume of an atomic sample and examined its significance as a physical realization of Maxwell's demon. We also demonstrated the robustness of the barrier's functionality to variations in several important experimental parameters. Lastly, we demonstrated the barrier's ability to cool an atomic sample, substantiating its potential application as a new cooling tool.

This dissertation includes previously published coauthored material.

CURRICULUM VITAE

NAME OF AUTHOR: Elizabeth A. Schoene

GRADUATE AND UNDERGRADUATE SCHOOLS ATTENDED:

    University of Oregon, Eugene, Oregon
    Harvey Mudd College, Claremont, CA

DEGREES AWARDED:

    Doctor of Philosophy in Physics, 2010, University of Oregon
    Bachelor of Science in Physics, 2001, Harvey Mudd College

PROFESSIONAL EXPERIENCE:

    Graduate Research Fellow, Department of Physics, University of Oregon, Eugene, Oregon, 6/04—6/08, 9/10—12/10

    National Science Foundation GK-12 Fellowship, University of Oregon, Eugene, Oregon, 6/08—6/10

    Graduate Teaching Fellow, University of Oregon, Eugene, Oregon, 9/03—6/04

    Peace Corps Volunteer, United States Peace Corps, Georgetown, Guyana, 6/01—8/03

GRANTS, AWARDS AND HONORS:

National Science Foundation GK-12 Fellowship, The University of Oregon, 6/08—6/10.

Outstanding Summer Research Presentation Award, The University of Oregon, 9/04.

Summer Undergraduate Research Fellowship (SURF), California Institute of Technology, 6/00—8/00.

Research Experience for Undergraduates (REU), Harvey Mudd College, 5/99—8/99.

PUBLICATIONS:

Elizabeth A. Schoene, Jeremy J. Thorn, and Daniel A. Steck, "Cooling Atoms with a Moving One-Way Barrier," *Physical Review A* **82**, 023419 (2010).

Jeremy J. Thorn, Elizabeth A. Schoene, Tao Li, and Daniel A. Steck "Dynamics of Cold Atoms Crossing a One-Way Barrier," *Physical Review A* **79**, 063402 (2009).

Jeremy J. Thorn, Elizabeth A. Schoene, Tao Li, and Daniel A. Steck, "Experimental Realization of an Optical One-Way Barrier for Neutral Atoms," *Physical Review Letters* **100**, 240407 (2008).

J. L. Hardwick, Z. T. Martin, E. A. Schoene, V. Tyng, E. N. Wolf, "Diode Laser Absorption Spectrum of Cold Bands of C_2HD at 6500 cm^{-1}," *Journal of Molecular Spectroscopy* **239**, 208 (2006).

ACKNOWLEDGEMENTS

I would like to take a moment to recognize many of the people whose support over the past seven years has been integral to my success, and without which, I probably would not have survived to write this.

First and foremost, I want to thank my advisor, Dan Steck. Under his calm and insightful guidance, I learned more than I had imagined possible, from machining and building circuitry to computer modeling and quantum measurement theory. His sheer breadth of knowledge and quiet confidence when pursing even the most difficult problems continues to amaze and inspire me.

I also owe a big thanks to all the members of the Steck Lab, past and present, including Tao Li, Jeremy Thorn, Peter Gaskell, Aaron Webster, Matthias Fuchs, Eryn Cook, Jonathan Mackrory, and Paul Martin. They made our lab not just a place to work, but defined a community and a culture. From friday night LN_2 ice cream to a lab ski trip, there was always some play to balance the work. In particular, I want to thank my partners in crime, Jeremy Thorn and Tao Li. The three of us built up the lab from day one, and I owe a huge part of my success to their hard work and help on the experiment, not to mention the occasional prank and morning discussions about Laker basketball.

To Poppy, who quietly supported me over the past seven years, and to whom I am the most proud to say "I have finished."

TABLE OF CONTENTS

LIST OF FIGURES

CHAPTER I

AN INTRODUCTION TO ATOM OPTICS

1.1.   Introduction

The idea that light can affect the motion of atoms by exerting a pressure was first described mathematically by Maxwell in 1873 [1], then later verified experimentally near the turn of the century [2–5]. However, it was only in the late 1970's that researchers started to develop schemes that harnessed these effects for useful purposes, such as cooling and trapping ions and neutral atoms [6–9]. These efforts gave birth to the field of atom optics, whose main thrust is the control and manipulation of atomic motion with laser light. This new field progressed rapidly, garnering widespread attention for the development of a relatively simple, yet robust technique for cooling atoms to microKelvin temperatures [10–12], and culminated in the achievement of dilute-gas Bose-Einstein condensation [13–15]—a new state of matter predicted by Einstein and Bose 70 years earlier that flirts with the limits of absolute zero.

Atomic cooling and motional control constitute the dual pursuits of atom-optics research, and both areas boast a myriad of notable achievements. During the late 1980's, atomic cooling schemes proliferated due to the quest for ever lower temperatures. Techniques incorporating polarization gradient cooling [16, 17] routinely came

within an order of magnitude of the recoil limit ($\sim 0.2 - 2~\mu$K depending on the atom), which corresponds to the kinetic energy imparted to an atom due to the recoil from emitting one photon. Two more schemes—appropriately dubbed "sub-recoil cooling" techniques—pushed temperatures below the recoil limit [18, 19], with one experiment reaching a temperature of 180 nK [20]. Achievements in controlling atomic motion paralleled the success of the cooling methods, as cold atoms are far easier to manipulate. This led to such novel constructs as atom gratings [21], lenses [22, 23], beamsplitters [24, 25] and interferometers [26–29], and drove advancements in the precision of atomic clocks [30, 31], the field of condensed matter physics via Bose-Einstein condensation [32] and degenerate Fermi gases [33, 34], and quantum information processing [35].

Bolstered by this wide array of accomplishments, the field of atom-optics research continues to thrive, working towards expanding cooling methods to new atomic and molecular species and probing the limits of atomic control. The work presented in this dissertation examines an all-optical one-way barrier for atoms—a type of atomic turnstile—which allows atoms to transmit when traveling in one direction, but inhibits their passage in the other direction. This work contributes to the coupled objectives of atom optics—cooling and control—as we demonstrate its ability to both direct atomic motion and reduce the temperature of an atomic sample.

1.2. Important Concepts

The notion that light can influence the center-of-mass motion of an atom should not come as a surprise, since absorption or emission of a photon necessitates a change in the atom's momentum due to the recoil from the event. We also know from classical mechanics that changes in momentum result from forces acting on a system, so that light must exert a force on the atom, even during an interaction with a single photon. Understanding the nature of these forces was crucial to the development of the multitude of clever techniques and applications that define the field of atom optics, and the pertinent physics is well documented in a number of references [9, 36, 37]. Having said that, we will briefly cover some of the important concepts particularly relevant to the work presented in this dissertation and refer the reader to the references for a more comprehensive discussion.

1.3. Light Forces on Atoms

In this section we will examine a two-level atom using a semi-classical approach, where we treat the atom quantum mechanically and the light field classically. Additionally, we will assume that the light field is monochromatic, and restrict the discussion to motion in one dimension (the z-direction) for simplicity, where z will refer to the mean atomic position. During this discussion we will draw on well established quantum optics methods and results, such as use of the rotating wave approximation, the rotating frame, and solutions of the optical Bloch equations [37–39].

Just as in classical mechanics, the force exerted on an atom is given by its change in momentum,

$$\hat{\mathbf{F}}_{\text{atom}} = \frac{d\hat{\mathbf{p}}}{dt}, \tag{1.1}$$

though here the force and momentum are quantum mechanical operators in the Heisenberg picture, such that they contain the time dependence. In this picture, the equation of motion for an operator $\hat{A}$ is given by

$$\frac{d\hat{A}}{dt} = \frac{i}{\hbar}[\hat{H}, \hat{A}], \tag{1.2}$$

where $\hat{H}$ is the Hamiltonian. Evaluating the commutator using the relationship

$$\hat{p} = -i\hbar\frac{\partial}{\partial z}, \tag{1.3}$$

yields the expression for the force

$$\hat{F}_{\text{atom}} = -\frac{\partial \hat{H}}{\partial z}. \tag{1.4}$$

For our purposes, $\hat{H} = \hat{H}_{\text{I}}$ is the Hamiltonian that describes the atom-field interaction, and is given by the expression

$$\hat{H}_{\text{I}} = \frac{\hbar}{2}\left(\Omega^*(z)\hat{\sigma} + \Omega(z)\hat{\sigma}^\dagger\right), \tag{1.5}$$

in the rotating frame, which removes the explicit $e^{i\omega t}$ time dependence of the light field. Here, $\hat{\sigma} = |g\rangle\langle e|$ and $\hat{\sigma}^\dagger = |e\rangle\langle g|$ are the atomic lowering and raising operators, respectively, while $\Omega(z)$ is the position-dependent Rabi frequency [37], given by

$$\Omega(z) = |\Omega(z)|e^{i\phi(z)}, \tag{1.6}$$

where

$$|\Omega(z)| = -\frac{2}{\hbar}\langle g|\hat{\varepsilon} \cdot \mathbf{d}|e\rangle|E_0(z)|. \tag{1.7}$$

The term $\langle g|\hat{\varepsilon} \cdot \mathbf{d}|e\rangle$ is the dipole matrix element and $\hat{\varepsilon}$ indicates the polarization direction of the electric field. The position dependence of the Rabi frequency reflects the fact that the amplitude and phase of the light-field ($|E_0(z)|e^{i\phi(z)}$) can vary spatially.

Taking the spatial derivative of the interaction Hamiltonian and then using $\langle \hat{A} \rangle = \mathrm{Tr}[\hat{\rho}\hat{A}]$ to find the expectation value produces the expression for the mean force

$$\langle F_{\mathrm{atom}} \rangle = -\frac{\hbar}{2}\Omega^*(z)\left(\frac{\partial_z|\Omega(z)|}{|\Omega(z)|} - i\partial_z\phi(z)\right)\tilde{\rho}_{eg}(z) + \mathrm{c.c.} \tag{1.8}$$

Here, we replaced the expectation value for the lowering operator $\langle \hat{\sigma} \rangle$ by the position dependent optical coherence, $\tilde{\rho}_{eg}(z)$, given by the off-diagonal matrix elements of the interaction Hamiltonian. For stationary or slowly moving atoms (slowly moving compared to their decay time), we can use the expression for the coherence from the steady-state solution of the optical Bloch equations, which is given by

$$\tilde{\rho}_{eg}(z) = \frac{-i\Omega(z)\big(\Gamma/2 + i\Delta\big)}{|\Omega(z)|^2}. \tag{1.9}$$

Here, Γ is the atomic decay rate and $\Delta = \omega - \omega_0$ is the detuning, defined as the difference between the atomic transition frequency ω_0 and the frequency of the light field ω. Substituting this expression into the equation for the mean force yields

$$\langle F_{\mathrm{atom}} \rangle = \frac{\hbar|\Omega(z)|^2}{2\big(\Gamma^2/4 + \Delta^2\big) + |\Omega(z)|^2}\left(\frac{\Gamma}{2}\partial_z\phi(z) - \Delta\frac{\partial_z|\Omega(z)|}{|\Omega(z)|}\right). \tag{1.10}$$

The expression for the force has two distinct terms that produce fundamentally different types of forces. We note that the first term is proportional to the decay rate, Γ, and results from the light field's phase dependence on position. This force is called the "radiation pressure force," and arises from momentum changes due to absorption and spontaneous emission of light. The dependence on spontaneous emission renders this force dissipative, as spontaneous emission is an irreversible process, and gives it a central role in many cooling schemes. The second term, on the other hand, is proportional to the detuning of the light, and results from the spatial variation of the optical intensity. This force is referred to as the "dipole force," and to the lowest order in $|\Omega|/\Delta$, originates from shifts in the atomic energy levels due to the electric field of the light. In contrast to the radiation pressure force, the dipole force is conservative, which makes it impractical for cooling atoms but rather a major player in optical trapping techniques. We will examine the dipole force more closely in Section 1.6.

1.4. Cooling with Light

To understand how to use the force of light on an atom to slow its motion, we must consider how velocity enters into the force calculations. An exact solution involves solving the optical Bloch equations including the mean atomic velocity, though this produces differential equations that are difficult to solve. A simpler approach treats the velocity as a perturbation to the position dependent parameters (i.e. $\Omega(z)$, $\tilde{\rho}_{eg}(z)$, etc.) and keeps only the first-order terms [36]. The resulting expression for the force

on an atom is quite complicated, so we will focus on the particular case of a plane wave.

For a plane wave of the form

$$\mathbf{E}(z,t) = \hat{\varepsilon}\frac{E_0}{2}\left(e^{i(kz-\omega t)} + e^{-i(kz-\omega t)}\right), \tag{1.11}$$

the mean force on an atom is given by

$$\langle\mathbf{F}_{\text{atom}}\rangle = \frac{\hbar\,\mathbf{k}\,\Gamma\,\Omega_0^2}{4\left(\Delta^2 + \Gamma^2/4 + \Omega_0^2/2\right)}\left(1 + \frac{2\Delta(\mathbf{k}\cdot\mathbf{v})}{\left(\Delta^2 + \Gamma^2/4 + \Omega_0^2/2\right)}\right). \tag{1.12}$$

Here, Ω_0 is the regular, real Rabi frequency

$$\Omega_0 = -\frac{\langle g|\hat{\varepsilon}\cdot\mathbf{d}|e\rangle|E_0|}{\hbar}, \tag{1.13}$$

with no position dependence nor complex components, and $\mathbf{v}$ is the velocity vector for the atom. The first term is the velocity-independent force on a stationary atom in a plane wave, which is given by the scattering rate multiplied by the momentum recoil per photon, $\hbar\mathbf{k}$. The second term gives the velocity-dependent part of the force, where we see that the magnitude of the force is proportional to the velocity. We also observe that the direction of the velocity-dependent force always *opposes* the atom's motion when $\Delta < 0$ (red-detuned light). For two counter-propagating plane waves, this feature results in a damping force that slows the atomic motion for red-detuned light. We can see this by recognizing that in the low intensity limit—when stimulated emission is negligible—the total force on an atom is given by the sum of the force for each plane wave [36]. The sum cancels out the velocity-independent term (due to the opposite $\mathbf{k}$ vectors), but leaves the damping part intact.

We can understand the origin of the damping force by considering the Doppler shift of an atom moving in the two counter-propagating plane waves for $\Delta < 0$. In particular, the plane wave directed *opposite* the atom's motion is Doppler shifted slightly closer to the atomic resonance, such that the atom scatters more light from this field than the co-propagating one, thus reducing its velocity. This cooling technique is appropriately called "Doppler cooling" due to its dependence on the Doppler shift, and is referred to as "optical molasses" [40] when implemented in three dimensions, as it is highly effective at rapidly cooling an atomic sample to microKelvin temperatures. Wineland *et al.* [41] provides a nice tutorial on the concepts behind Doppler cooling. The standard, experimental realization of optical molasses involves three, opposed pairs of laser beams, one for each dimension.

1.5.   Magneto-Optical Trapping

Though enormously successful at cooling atoms, optical molasses has no ability to trap them by constraining their position. Consequently, nothing prevents the atoms from diffusing out of the cooling beams, and hence, the region of experimental interest. The cooling utility of optical molasses stems from the velocity dependence of the detuning for a moving atom, which results in the atom scattering more light from the opposing field. A similar approach can be implemented to trap the atom as well by making the detuning position-dependent. In this case, the atom will scatter more

light from the opposing field when it is displaced from a specified origin, pushing it back towards that position.

We can make the detuning position-dependent by adding a magnetic field that changes linearly with position. An atom moving in this magnetic field will experience a position-dependent Zeeman shift of its energy levels, which effectively alters the detuning of the light and thus the scattering rate, depending on the atom's position relative to the zero of the magnetic field. Circularly polarized light is required to create asymmetric scattering rates for the two counter-propagating plane waves.

We can incorporate the effect of the magnetic field into the force calculation by including the Hamiltonian that describes the Zeeman shift [42]

$$\hat{H}_{\text{Z}} = -\hat{\boldsymbol{\mu}} \cdot \mathbf{B} \tag{1.14}$$

into the interaction Hamiltonian $\hat{H}_{\text{I}}$. Here, $\hat{\boldsymbol{\mu}}$ is the magnetic moment operator for the atom and $\mathbf{B} = B_0 \mathbf{z}$, where $\mathbf{z}$ is the atomic position vector. For an atom moving in two counter-propagating plane waves with opposite circular polarizations, this yields (to the lowest order in $\mathbf{v}$ and $\mathbf{z}$) [36]

$$\langle \mathbf{F}_{\text{atom}} \rangle = \frac{\hbar \mathbf{k} \, \Gamma \, \Omega_0^2 \, \Delta}{\left(\Delta^2 + \Gamma^2/4 + \Omega_0^2/2 \right)^2} \left(\mathbf{k} \cdot \mathbf{v} + \frac{\mu' B_0}{\hbar k} \, \mathbf{k} \cdot \mathbf{z} \right), \tag{1.15}$$

where μ' is the effective magnetic moment for the transition [36]. Similar to the velocity-dependent force, we see that the position-dependent force always pushes the atom in the direction opposite its position vector for $\Delta < 0$, driving the atom toward the zero of the magnetic field.

Implementing optical molasses in tandem with a three-dimensional, linear magnetic field creates a powerful cooling and trapping tool called a "magneto-optical trap" (MOT) [43]. The MOT has become by far the most prolific atomic cooling and trapping technique due to its relatively straightforward implementation and robustness to significant variations in the different experimental parameters. As such, it serves as the starting point for nearly all atom-optics experiments, as it does for the one-way barrier experiments discussed in this dissertation. References [10–12, 36, 44] have nice discussions on the concepts and mechanics of a MOT, which we did not cover in great detail here.

1.6. The Optical Dipole Force

The origin of the optical-dipole force discussed in Section 1.3 can be traced to the ground- and excited-state coherences generated by the atom-field interaction. To understand this, we will examine the atom-field Hamiltonian under the same idealizations outlined previously (two-level atom, monochromatic field, etc.), highlighting a few salient features.

The atom-field Hamiltonian $\hat{H}_{\text{AF}}$ in the rotating frame is given by the sum of the atomic and interaction Hamiltonians

$$\hat{H}_{\text{AF}} = \hat{H}_{\text{atom}} + \hat{H}_{\text{I}} \tag{1.16}$$

$$\hat{H}_{\text{AF}} = -\hbar\Delta\,\hat{\sigma}^\dagger\hat{\sigma} \; + \; \frac{\hbar\Omega_0}{2}\big(\hat{\sigma}^\dagger + \hat{\sigma}\big), \tag{1.17}$$

where we have not included any position dependence in the Rabi frequency Ω_0. This

Hamiltonian can be represented in the atomic-state basis (the $|e\rangle$ and $|g\rangle$ basis) by the matrix

$$\hat{H}_{\text{AF}} \rightarrow \begin{bmatrix} 0 & \dfrac{\hbar\Omega_0}{2} \\ \dfrac{\hbar\Omega_0}{2} & -\hbar\Delta \end{bmatrix}, \tag{1.18}$$

where the presence of off-diagonal matrix elements, which describe the ground- and excited-state coherences, indicate that the atomic energy levels are not eigenvalues of this Hamiltonian. We can diagonalize this matrix to find the new eigenstates, which have eigenvalues

$$E_{\pm} = -\frac{\hbar\Delta}{2} \pm \frac{\hbar}{2}\sqrt{\Delta^2 + \Omega_0^2}, \tag{1.19}$$

that shift the atomic ground- and excited-state energy levels from their non-interacting values. We can see from this expression that the optical coherences are responsible for the energy shifts, which are called "ac Stark shifts" since they originate from the oscillating (ac) electric field. Of particular importance is the case when the detuning is large ($|\Delta| \gg |\Omega_0|, \Gamma$) and the interaction is no longer resonant. Under these circumstances, the atom will remain almost exclusively in the ground state and the energy shift due to the electric field is approximated by the expression

$$\Delta E_g \approx \frac{\hbar\,\Omega_0^2}{4\,\Delta}. \tag{1.20}$$

Since Ω_0^2 is proportional to the field intensity, we see that the magnitude of the energy shift depends on both the detuning and the intensity of the field, while the direction of the shift depends on the sign of the detuning. It is not hard to see that if the intensity

of the field varies with position, such as for a focused laser beam, the magnitude of the energy shift will become position-dependent.

In this case, a conservative force must accompany the change in energy an atom experiences as it moves through the intensity gradient of the light field, since no energy is dissipated in the process (e.g. from spontaneous emission). This allows us to write the mean force as the negative gradient of a potential

$$\langle F_{\text{dipole}} \rangle = -\partial_z V_{\text{dipole}}, \tag{1.21}$$

expressed here for a one-dimensional potential. In fact, we can rearrange the dipole term in the equation for the force of light on an atom [Eq. (1.10)] to fit this form [37]:

$$\langle F_{\text{dipole}} \rangle = -\frac{\hbar\Delta}{2} \, \partial_z \log\left[1 + \frac{|\Omega(z)|^2}{2\left(\Gamma^2/4 + \Delta^2\right)}\right], \tag{1.22}$$

where V_{dipole} is given by

$$V_{\text{dipole}} = \frac{\hbar\Delta}{2} \log\left[1 + \frac{|\Omega(z)|^2}{2\left(\Gamma^2/4 + \Delta^2\right)}\right], \tag{1.23}$$

and the position dependence is built into the Rabi frequency. In the limit of a large detuning ($|\Delta| \gg |\Omega(z)|, \Gamma$), we can approximate this force and the corresponding potential by the expressions

$$\langle F_{\text{dipole}} \rangle \approx -\frac{\hbar}{4\Delta} \, \partial_z \left(|\Omega(z)|^2\right) \tag{1.24}$$

$$V_{\text{dipole}} \approx \frac{\hbar \, |\Omega(z)|^2}{4\Delta}. \tag{1.25}$$

Here, the expression for the potential replicates the result obtained for the ac Stark shift in this limit, but with a complex and position-dependent Rabi frequency. An atom interacting with the light field will navigate the potential energy curve defined by the field's intensity profile, with the strength of the potential determined by the field's detuning and intensity at any given position. The detuning also controls the sign of the potential, with red-detuned light ($\Delta < 0$) forming an attractive potential and blue-detuned light ($\Delta > 0$) creating a repulsive potential.

We also see that the magnitude and direction of the force exerted on the atom depend on both the magnitude and sign of the intensity gradient and the detuning. We can illustrate this by considering a focused, Gaussian beam with the longitudinal intensity profile depicted in Figure 1.1(a). In this situation, the *direction* of the force an atom experiences when displaced to the right of the focus (where the force is zero) depends exclusively on the sign of the detuning, since the intensity profile has a negative slope at this position [Fig. 1.1(b)]. In particular, red-detuned light produces a force *opposite* the atom's position vector, which pushes it back towards the region of highest intensity (the focus) [Fig. 1.1(c)]. The sign of the force reverses for blue-detuned light, such that the atom is repelled from the region of highest intensity.

At first glance, it appears that creating a strong potential simply involves cranking up the intensity of the field relative to the detuning. While this indeed increases the potential strength, it also increases the scattering rate, heating the atom and ruining the conservative nature of the force. Fortunately, the scattering rate is proportional
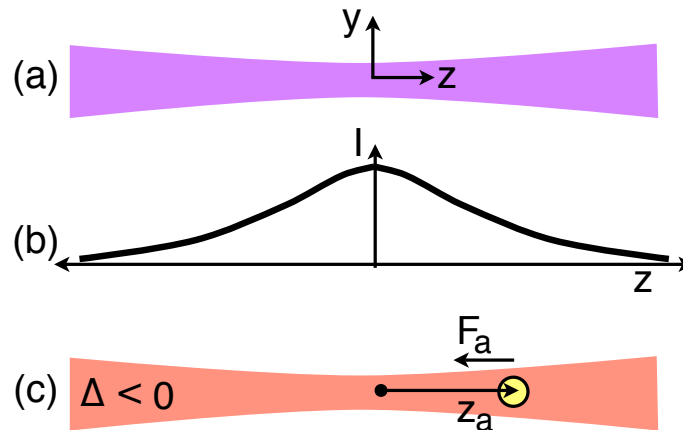
Figure 1.1. Schematic diagram showing some important features of an optical dipole trap. (a) Geometry of a focused, single-beam optical dipole trap. (b) Intensity profile along the longitudinal dimension of the trap. (c) Illustration of the force F_a acting on a trapped atom when displaced from the focus by a distance z_a for a red-detuned trap.

to I/Δ^2 (as opposed to I/Δ for the potential), so very large detunings *and* intensities can create strong potentials with minimal scattering.

A wide variety of atom traps exploiting the optical dipole potential for both red- and blue-detuned light have been implemented over the years [45–47]. These are collectively referred to as "optical dipole traps," reflecting the purely optical (e.g. not magnetic) nature of the confinement. The most simple example of an optical dipole trap is the focused, single-beam trap mentioned above, which describes the relevant physics for both applications of this phenomenon used in our experiments.

1.7. Temperature

Laser cooling techniques are powerful experimental tools due to their exceptional ability to slow atomic motion. The slow atomic speeds correspond to very low mean

kinetic energies, which we can relate to a temperature T for a one-dimensional thermal distribution using the equipartition theorem

$$\langle E_{\text{kin}} \rangle = \frac{k_{\text{B}} T}{2},\tag{1.26}$$

where k_{B} is Boltzmann's constant. Though an atomic ensemble in atom-optics experiments may not necessarily be in thermal equilibrium, it is still convenient to report a temperature to describe the ensemble's average kinetic energy. As such, the temperature quickly became an important metric for evaluating and comparing different slowing schemes, earning them the collective moniker "laser *cooling* techniques." Due to the importance of temperature measurements both in atom-optics research in general and, in particular, to the work presented in this dissertation (where we demonstrate a new cooling technique), we will outline a few methods for measuring the temperature and indicate their application in our experiments. We also note that throughout this section we discuss the temperature for a one-dimensional atomic distribution, though technically temperature is not defined unless all velocity components are considered.

A very common technique for measuring the temperature utilizes the free expansion of an atomic ensemble, and is referred to as a "time of flight" measurement. In this technique, an image of the atomic sample's spatial distribution is taken after a brief (roughly $10 - 20$ ms) period of free expansion. For sufficient expansion times, the final spatial distribution directly reflects the momentum distribution at the time of release, as each atom's momentum determines how far it will travel

during the expansion. The momentum distribution is found by converting the spatial

distribution's position coordinate to momentum using the equation

$$p = \frac{mx}{t},$$

(1.27)

where m is the atomic mass and t is the expansion time. For a Gaussian momentum

distribution, the temperature is given by the expression [47]

$$T = \frac{\sigma_p^2}{mk_{\mathrm{B}}},$$

(1.28)

where σ_p is the width of the momentum distribution. We used this method to measure

the temperature of the atoms in our MOT, though the small diameter of our laser

beams made this method less than desirable for most of our measurements, since the

atoms would rapidly expand out of the beams.

With the exception of measuring the temperature of the magneto-optically trapped

atoms, all our other temperature measurements involved atoms confined in an optical

dipole trap. For these atoms, the (steady-state) spatial density distribution in the

dipole trap is related to the temperature through the expression [47]

$$n(z) = n_0 e^{\left(-\frac{U(z)}{k_{\mathrm{B}}T}\right)},$$

(1.29)

where $U(z)$ is the one-dimensional trapping potential and n_0 is the density at the

zero of the potential. For the focused, single-beam dipole trap employed in our

experiments, we can approximate the potential near the focus (within about a third

of the Rayleigh length) as harmonic. Under these circumstances, the temperature of

the atoms directly relates to the width of the Gaussian density distribution σ_z and the harmonic trap frequency ω_z by the equation

$$T = \frac{m}{k_{\mathrm{B}}} \sigma_z^2 \omega_z^2. \tag{1.30}$$

Unfortunately, the spatial extent of our atomic ensemble reaches well beyond the region appropriate for using the harmonic approximation. In this case, the width of the distribution still indicates the temperature, however, the dependence is no longer quadratic.

Though we do not explicitly know how the temperature depends on the spatial distribution's width outside the harmonic approximation, we can still calculate the temperature by making use of the virial theorem,

$$2 \langle \, [\langle E_{\mathrm{kin}} \rangle] \, \rangle_t = - \sum_{k=1}^{N} \langle \mathbf{F}_k \cdot \mathbf{z}_k \rangle_t \,, \tag{1.31}$$

which relates the average kinetic and potential energies of N particles, in equilibrium, bound by a potential. Here, $\mathbf{F}_k$ is the force on the kth particle at position $\mathbf{z}$ due to the dipole potential, which we have assumed to be one-dimensional, and the outer angle brackets $\langle \, \rangle_t$ denote the time average. We consider the atoms to be in equilibrium because the spatial distribution does not change much. We can calculate the temperature from the average kinetic energy using Eq. (1.26).

1.8. Phase Space

Generally speaking, the phase space for the one-dimensional motion of a classical particle describes all the possible position and momentum states (x, p) accessible to the particle for a given energy. The probability of finding the particle at position x with momentum p is given by the joint probability distribution $\rho(\mathbf{x}, \mathbf{p})$, which is called the "phase-space density." For a classical particle, the position and momentum can be known with arbitrary certainty, such that $\rho(\mathbf{x}, \mathbf{p})$ is sharply peaked about those values. This is not the case, however, for an ensemble of cold atoms, where the exact position and momentum for individual particles are not known due to their small size and high density. In this situation, the position and the momentum of the *ensemble* become important, and the phase-space density is related to the ensemble's spatial and momentum distributions.

A particularly useful quantity when discussing ensembles of cold atoms is the average phase-space density, defined for one dimension as

$$\langle \rho(x, p) \rangle = \int \rho^2(x, p) dx dp. \tag{1.32}$$

We can use the average phase-space density to characterize the extent of the joint probability distribution in $x - p$ space in terms of the phase-space density ρ_{D} and phase-space volume ρ_{V},

$$\rho_{\mathrm{D}} = N \langle \rho(x, p) \rangle \tag{1.33}$$

$$\rho_{\mathrm{V}} = \frac{N}{\rho_{\mathrm{D}}}, \tag{1.34}$$

where N is the number of atoms in the ensemble. Note that we are using the term "phase-space density" to describe two different quantities; here we are referring to an actual density that incorporates the number of particles, whereas previously we were referring to the joint probability distribution $\rho(\mathbf{x}, \mathbf{p})$. We also note that the terms "phase-space density" and "phase-space volume" are both commonly used in the literature.

To compute the average phase-space density, we start by assuming the velocity distribution is independent of position, allowing us to write

$$\rho(x, p) = \rho_x(x)\rho_p(p). \tag{1.35}$$

Here, $\rho_p(p)$ is given by the Maxwell-Boltzmann momentum distribution, which links the average phase-space density to the temperature of the ensemble. This allows us to evaluate the momentum integral separately, yielding the expression

$$\langle \rho(x, p) \rangle = \frac{1}{\sqrt{2\pi m k_{\mathrm{B}} T}} \int \rho_x^2(x) dx \tag{1.36}$$

for an arbitrary position distribution. For a Gaussian position distribution, the expression for the average phase-space density simplifies to

$$\langle \rho(x, p) \rangle = \frac{1}{\sigma_x \sqrt{m k_{\mathrm{B}} T}}, \tag{1.37}$$

where σ_x^2 is the variance of the Gaussian position distribution.

When cooling atoms, we typically are not interested in the absolute phase-space volume, but rather the *change* in phase-space volume. Colder atoms correspond to

smaller phase-space volumes, and the amount of phase-space compression achieved for a cooling process is regarded as a figure of merit. Though temperature provides one measure of the effectiveness of a cooling technique, phase-space compression is a more powerful measure as it speaks to the increase in the density of the atoms as well. We can calculate the compression factor for a Gaussian position distribution using the ratio

$$\frac{\rho_V^i}{\rho_V^f} = \frac{\sigma_x^i \sqrt{T^i}}{\sigma_x^f \sqrt{T^f}}, \tag{1.38}$$

which simplifies to

$$\frac{\rho_V^i}{\rho_V^f} = \frac{(\sigma_x^i)^2}{(\sigma_x^f)^2} \tag{1.39}$$

by relating the temperature of the Gaussian distribution to its width using Eq. (1.30). Here, the superscript i indicates the initial value and the superscript f the final value.

Figures 3.7, 4.5, 4.7-4.15, 5.2, and 5.4-5.7 have been published with coauthors.

CHAPTER II

EXPERIMENTAL SETUP

2.1. Introduction

The backbone of our one-way barrier experiments is the basic experimental appa-ratus that enables us to cool and trap ^{87}Rb atoms. Designing and constructing the appa-ratus constituted a substantial component of realizing these experiments, and the apparatus will remain functional for future work beyond the one-way barrier. We devoted part of Chapter 1 to explaining the basic physics of atom cooling and trapping, and here we will describe the different aspects of implementing those tech-niques. In particular, we will detail the laser system, ultra-high vacuum system, magnetic field coils, dipole-trap laser, imaging system, and control and timing elec-tronics.

2.2. Overview

Our general design employs a double-MOT system [48], where atoms from one MOT in a higher pressure region of the chamber are rapidly transported to a second MOT in a lower pressure region. This design traps large numbers of atoms at very low background pressures. Our particular implementation of the double-MOT system

uses a pyramid MOT [49, 50] for the first MOT—which we will describe in more detail in Section 2.4.1—and the standard, six-beam MOT configuration (Section 1.4, 1.5) for the second MOT. We use anti-Helmholtz coils to create the linear magnetic field necessary for trapping (Section 1.5), and pairs of Helmholtz coils to shift the zero-field position in all three dimensions.

2.3. Laser System

The laser system needed to create a functional magneto-optical trap (MOT) for ^{87}Rb requires two specific, stable laser frequencies—one for the cycling transition and one for the repump transition (see Section 2.3.5)—adequate power, frequency tuning capability, μs on/off switching and power control, and the ability to transport the beams to specific places over long distances. Below we will discuss the various optical components and techniques we use to fulfill these requirements and form a versatile laser system.

2.3.1. Slave Lasers

We use two types of home-built diode lasers, but the most basic one is essentially a free-running (no external feedback) diode that we will refer to as a "slave laser" (see Section 2.3.3 for the origin of the name). We purchased laser diodes manufactured by Sharp Micro-electronics (P/N GH0781JA2C) with a nominal wavelength of 784 nm, a wavelength that is commonly used in CD players, making them fairly cheap and readily available. This type of laser diode typically has the back facet of the semi-

conductor material reflection coated and the front facet anti-reflection (AR) coated, and the two facets form the cavity necessary for lasing [51]. The beam produced by this laser diode has a maximum output power of 120 mW, is single mode (transversely and longitudinally), and in the absence of any optics, the beam is uncollimated, has an elliptical spatial profile, and is linearly polarized perpendicular to the major axis of the ellipse [51, 52].

Since the diode is free-running, the temperature of the diode and the current it receives are the only means to control its power and operating frequency. Typically, the power output increases linearly with the injection current over threshold [52], and reducing the temperature increases the output power as well. The dependence of the frequency on the temperature and the injection current are well documented [51, 52], showing that generally, warmer diodes and higher injection currents produce longer wavelengths. It has also been shown that colder diodes tend to have longer life spans [51].

We secure the diode in a tube with an adjustable lens at the end to collimate the beam (Thorlabs P/N LT230P-B). We then place this lens tube in an aluminum piece and hold it in place with a set screw [Fig. 2.1(a)], achieving vertical polarization of the beam by rotating the lens tube before fixing it in place. We insert two temperature sensors, a 50 kΩ glass bead thermistor (Fenwall Electronics P/N 121) and an IC temperature sensor (Analog Devices P/N AD590JH), into the aluminum piece, which sits on top of a thermo-electric cooler (Melcor P/N CP1.0-127-05L). We sandwich the

thermo-electric cooler between the aluminum piece and the aluminum base plate of the laser housing using nylon screws [Fig. 2.1(c)], ensuring thermal isolation of the aluminum piece, which is extremely important to help regulate the temperature of the diode. We feed the electrical connections for the current- and temperature-control electronics through the base plate and attach them to a small diode protection circuit board and to the thermo-electric cooler and the temperature sensors, respectively. We connect the laser diode directlyk to the protection board. The diode, lens tube, aluminum piece, thermo-electric cooler, and protection circuit are all housed inside a lid made of polycarbonate, chosen for its low thermal conductivity. The beam exits the housing through a hole with a microscope slide attached at Brewster's angle to prevent back reflections [Fig. 2.1(a)].

After exiting the laser housing we reflect the beam off two steering mirrors and then pass it through a pre-mounted, anti-reflection coated anamorphic prism pair (Thorlabs P/N PS875 2.0 X) to correct for the elliptical spatial profile. A half-wave plate then rotates the beam's polarization by $45°$ prior to entering an optical isolator (Conoptics P/N 712B/713A). The isolator guarantees that no back reflections can reach the diode, and the wave plate ensures the polarization of the light exiting the isolator is rotated back to vertical, since the isolator rotates it by $45°$ (Fig. 2.2).

The circuitry required to operate this diode laser consists of temperature stabilization and current control electronics. The temperature-control circuit is a basic proportional, integral, differential (PID) feedback controller built around Wavelength
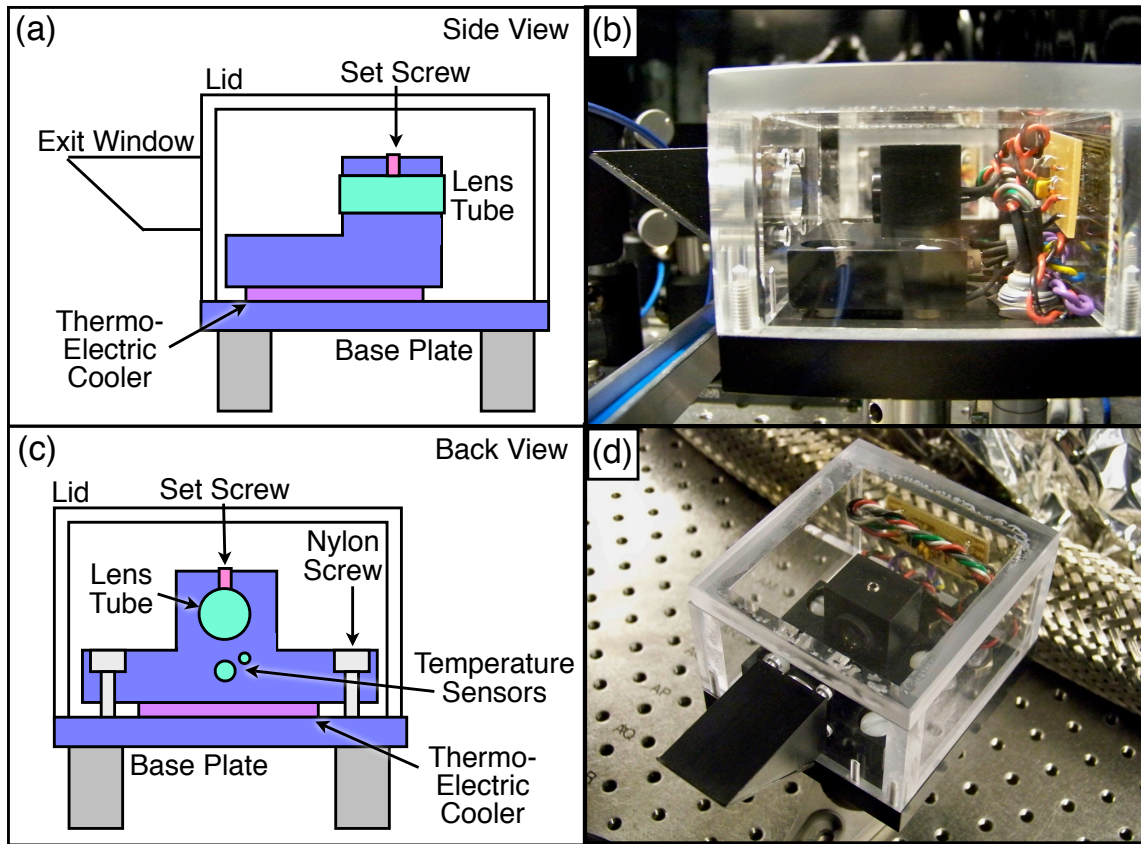
Figure 2.1. Schematic diagram and pictures of the slave laser. (a) Side view showing the lens tube, set screw, thermo-electric cooler, base-plate, polycarbonate lid and Brewster's angle exit window. (b) Side-view picture of the slave laser. (c) Back view showing most of the same features plus the temperature sensors and nylon screws. (d) Front- and top-view picture of the slave laser.
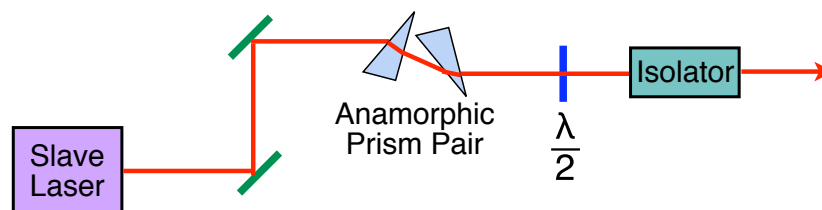
Figure 2.2. Schematic of the optical elements used to control and shape the diode laser's output beam, including the steering mirrors, anamorphic prism pair, half-wave plate, and optical isolator.

Electronics' WTC3243 chip, originally designed by Todd Meyrath, then modified for our appli-cations. The thermo-electric cooler is connected to the control circuit and it can source or sink heat from the base plate of the laser housing to the aluminum piece containing the laser diode, depending on the direction of the current flow. The temperature-feedback measurements are made by the thermistor that is embedded in the aluminum piece, and the IC temperature sensor (AD590) is connected to a separate circuit that measures and displays the temperature on an LCD screen (Lascar Electronics P/N SP-400). The user can adjust the temperature set-point via a 10-turn potentiometer, and can flip a switch to turn off the feedback control completely. With these control electronics, the temperature is stable to 3 mK over several days.

The current-controller circuit serves to provide a steady, user-controlled current to the diode, and also protects the diode from fluctuations and spikes in the power supply. The steady current supply is accomplished with a PID feedback-control circuit, and the current output is displayed on an LCD screen. The user can manually adjust the current with course- and fine-tuning 10-turn potentiometers, and flip a switch to turn the current to the diode on or off. There is also a current-modulation input that modifies the current from the value set by the adjustment potentiometers. For protection, the user can set a current limit that cannot be exceeded by the adjustment potentiometers or the modulation input. We set the current limit to 110 mA, and a red LED lights up if the current set-point goes above this value. Additionally, the diode is automatically shorted when the current turns off for any reason (including

power loss), and there is a switch that allows the diode to be shorted even while the current is on.

2.3.2. Master Lasers

The second type of diode laser we built uses a diffraction grating to feed some of the laser light back into the diode itself to allow for improved frequency tuning and to spectrally narrow the output [51]. This type of diode laser is commonly called a "grating-stabilized diode laser" or a "psuedo-external cavity" diode laser, referring to the larger cavity formed between the diode's back facet and the grating. Here we will refer to it as a "master laser" (see Section 2.3.3 for the origin of the name). Some of the properties, design, and electronics are the same as for the slave laser described above, such as the output beam characteristics, the lens tube that holds the diode, the polycarbonate housing, the Brewster's angle exit window, the temperature control, current control, and diode protection electronics, and the series of optics used to align, shape the beam, and protect against back reflections.

The diffraction grating is arranged in the Littrow configuration [53], where the zero-order diffraction beam forms the output beam of the laser, while the first-order diffraction beam is reflected back into the laser diode to provide optical feedback. The introduction of the grating to form one end of the optical cavity improves the quality factor of the cavity, and also acts as a frequency selector, since the grating angle determines the wavelength of light diffracted back into the laser diode. These improvements narrow the spectral linewidth of the laser and help with frequency

control [51]. A nice tutorial and design for a laser in the Littrow configuration is given by MacAdam [54].

To construct this laser, we used a design by Daniel Steck, Bruce Klappauf, and Windell Oskay [55–57], which was modified to accommodate 780 nm laser light. This laser design has also been described in Tao Li's dissertation [58]. The laser consists of four pieces, the diode mounting block, the grating mount, and an upper and lower base plate, all machined from 954 aluminum bronze. This material was chosen for its strength and fatigue resistance—since two of the laser pieces have thin sections that are load bearing—as well as its decent thermal conductivity, which helps with temperature stabilization.

We secure the diode in the mounting block the same way as for the slave laser. The grating mount allows the grating (Edmund Optics P/N NT43-751) to be glued onto a lever arm, which is backed by a piezoelectric stack (Noliac P/N SCMA/S2/A/-5/10/60/9/1500) and a fine-adjustment screw (New Focus P/N 9301-K) [Fig. 2.3(b)]. The piezo rotates and translates the grating, scanning the laser frequency by modifying the cavity length and grating angle. The rotation point of the grating is chosen carefully so the wavelengths selected by the cavity length and grating angle change at the same rate during scanning, increasing the mode-hop free tuning range [59–61]. The grating angle is coarsely set by the placement of the grating mount with the aid of an alignment rod, and finer adjustments are made with the set screw that resides behind the piezo stack. We glued a bar magnet (K&J Magnetics) onto the top of
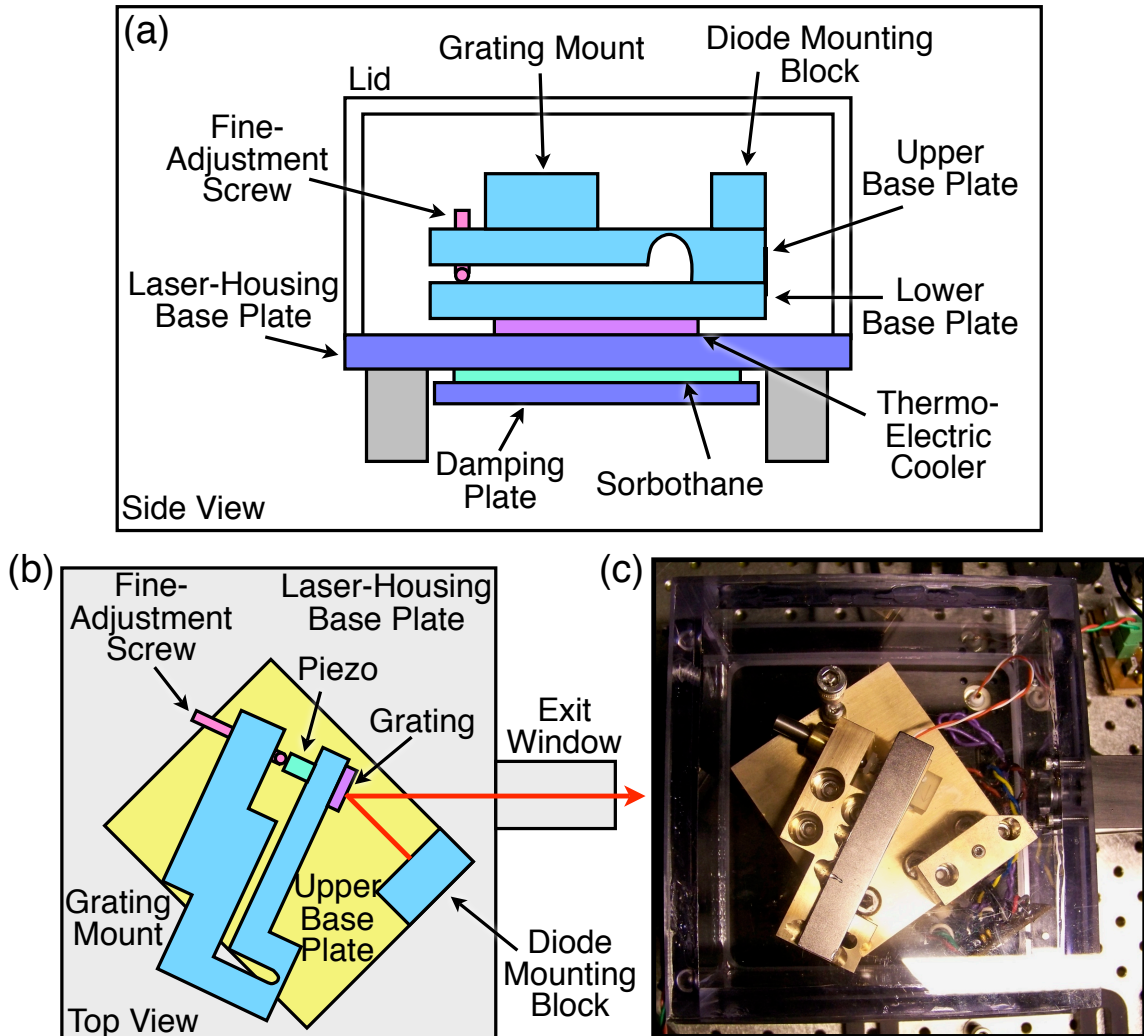
Figure 2.3. Schematic diagram and picture of the master laser. (a) Side view showing the upper and lower base plates, fine-adjustment screw, grating mount, diode mounting block, thermo-electric cooler, laser-housing base plate, sorbothane, damping plate and polycarbonate lid. (b) Top view showing the grating mount, grating, piezo, fine-adjustment screw, diode mounting block, laser-housing base plate, and exit window. (c) Top-view picture of the master laser.

the grating lever arm to help damp its vibrational resonances, improving the laser's

stability.

The upper base plate attaches to the lower base plate, and has two sections of different thickness separated by a thin connection that allows for flexing [Fig. 2.3(a)]. The grating mount and the diode mounting block attach to the upper base plate on opposite sides of the thin, flexing region. Another fine-adjustment screw (New Focus P/N 9312-K) is placed between the upper and lower base plates, which allows for vertical alignment of the grating by tilting the upper base plate. The laser housing is the same as for the slave laser, except for the larger size and the addition of a damping plate. The damping plate consists of a piece of aluminum attached to the bottom of the laser-housing base plate with a piece of sorbothane sandwiched in between [Fig. 2.3(a)]. This arrangement damps mechanical vibrations of the laser-housing base plate that affect the laser's stability.

2.3.3. Locking the Slave to the Master

The addition of the grating in the master laser reduces the output power to about 25 mW, which is not sufficient to create two MOTs after accounting for losses from the myriad of optical components needed to stabilize and control the laser frequency, and the $\sim$50% loss from transporting the light via optical fibers. To achieve the necessary power, we feed a small amount of master-laser light into two slave lasers, which forces the slave lasers to lase with the same spectral characteristics as the master laser. This process is called "injection-locking," and harnesses the power of the slave lasers (about 50 mW) while retaining the narrow linewidth and frequency stability of the master laser. Typically, we feed about 4 mW of master laser light through the second

rejection port of each slave laser's optical isolator [62] and monitor the output of the slave lasers on a 1.5 GHz, home-built Fabry-Perot cavity to verify locking. When locked, we see only one peak in the Fabry-Perot spectrum—corresponding to the master-laser frequency—while two peaks are visible if the slave laser is unlocked; one at the master-laser frequency and one at the free-running slave-laser frequency.

As we mentioned in Section 2.3, two different laser frequencies are required to create a MOT: the MOT cycling frequency, which excites the $F = 2 \rightarrow F' = 3$ ^{87}Rb D$_2$ hyperfine transition, and the repumping frequency, which excites the $F = 1 \rightarrow F' = 2$ hyperfine transition (Fig. 2.4). The MOT cycling transition, often referred to as the "MOT-trapping" transition, is responsible for cooling the atoms (Section 1.4). The repump simply returns atoms that fall into the $F = 1$ ground state back into the cycling transition so they can participate in the cooling process. Each of these frequencies has a master laser dedicated to providing frequency-stabilized laser light to the two MOTs. The frequency stabilization scheme involves active feedback control of the laser frequency by "locking" it to a narrow spectroscopic feature, as well as precise frequency shifts using acousto-optic modulators (AOMs). We will describe both of these aspects in the next two sections.

2.3.4. Acousto-Optic Modulators

We will give a brief description of acousto-optic modulators (AOMs) first [53], since they play an important role in many aspects of our experiment. An AOM uses sound waves to create a moving, periodic variation in the index of refraction
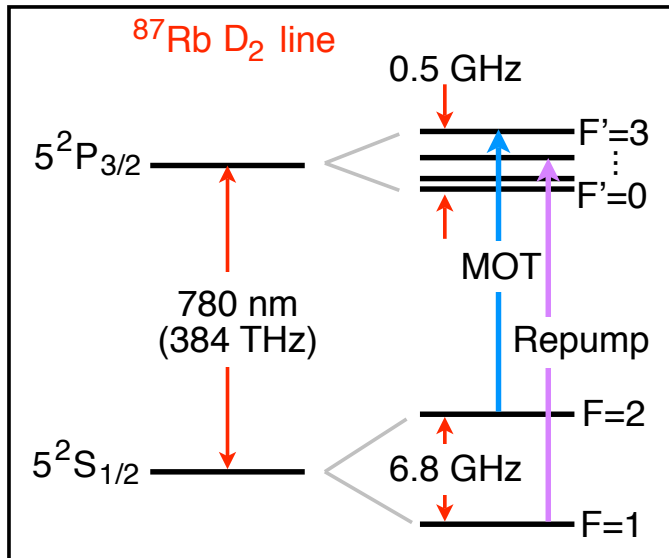
Figure 2.4. Hyperfine structure for the ^{87}Rb D$_2$ transition showing the relative frequencies of the different levels and the MOT and repump transitions.

of a crystal, which shifts the frequency and direction of an incident laser beam by diffraction from the index variation. The phonons are generated by driving a piezo affixed to the crystal at radio frequencies (RF) up to several hundred MHz. A first-order diffraction efficiency of about 80% can be achieved when the light is incident on the crystal at the Bragg angle, $\theta_B = \lambda/2\Lambda$ (for small angles), where λ is the laser wavelength and Λ is the sound wavelength. The diffracted beam forms an angle $\theta = 2m\,\theta_B$ with respect to the zero-order diffraction beam, where m is the diffraction order, thus changing the direction of the beam. The AOM also shifts the laser frequency up or down by integer amounts of the driving frequency, where the integer equals the diffraction order. In addition to frequency shifting, we use the AOM as a fast shutter (sub-μs shuttering time) and attenuator for light in the non-

zero diffraction orders by reducing the piezo's driving voltage or switching it on and off.

Driving and controlling the AOMs requires three different electronic components: an RF signal generator, a digital RF switch for shuttering, and an RF amplifier to create the power needed to drive the piezo. All three of these components were designed and built in house by Peter Gaskell. The RF signal is generated by a voltage-controlled oscillator with a $50 - 100$ MHz range, and the surrounding circuitry allows for manual and computer control of the frequency and amplitude of this signal, as well as an output for monitoring the frequency.

Since the AOM shifts the direction of the laser beam proportional to the driving frequency, applications that involve changing the driving frequency require double-passing the laser through the AOM. This technique ensures the beam remains aligned with the optics placed downstream from the AOM despite the shifting direction. The optical setup for double-passing an AOM is shown schematically in Figure 2.5. The basic idea consists of focusing the beam at the center of the AOM, retro-reflecting the first-order diffraction beam from a judiciously-placed spherical mirror back through the AOM, and then using a polarizing beam splitter cube (PBSC) to separate the frequency-shifted light. We place the spherical mirror a distance equal to its radius of curvature from the beam's focus in the center of the AOM, so that all the light is reflected back through the focus regardless of any changes in beam direction. The second pass through the AOM shifts the light's frequency again, resulting in a total
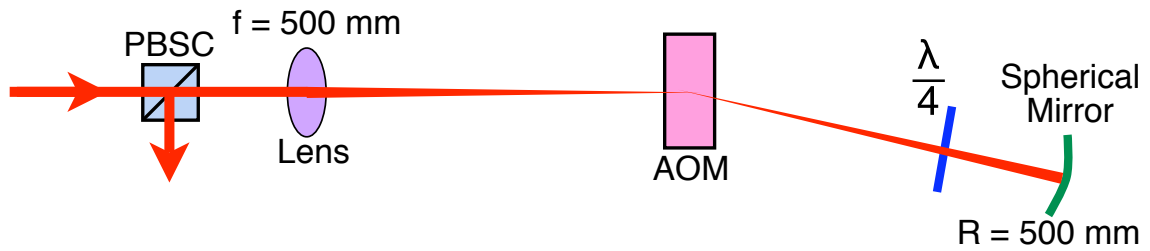
Figure 2.5. The optical setup for double-passing an acousto-optic modulator (AOM), including the polarizing beam splitter cube (PBSC), lens, AOM, quarter-wave plate, and spherical mirror.

frequency shift of twice the driving frequency. It also changes the direction of the beam a second time, such that it overlaps with the incoming, unshifted beam. To separate the beams we horizontally polarize the incoming beam and pass it through a PBSC before sending it through the AOM. A quarter-wave plate placed between the AOM and the spherical mirror rotates the polarization the same direction on each pass, resulting in vertically polarized light that the PBSC separates from the incoming, horizontally polarized light. We use a 500 mm focal length lens and an $R = 500$ mm spherical mirror with a 99% reflection coating at 780 nm from VLOC.

2.3.5. Frequency Locking

We create the MOT by exciting specific hyperfine energy levels that are separated by only a couple hundred megahertz, which requires laser frequencies stable to about 1 part in 10^9. Despite the master laser's current and temperature stabilization, the frequency of the laser still drifts significantly over time, making active feedback control of the frequency necessary. To accomplish this, we use a home-built PID feedback control circuit designed by Daniel Steck. This circuit supplies multiple components

of the laser operation and frequency control electronics, including a lock-in amplifier, a local oscillator for lock-in detection, a ramp generator and driver for the laser's piezo, and feedback control for the laser current and the piezo voltage. We use this circuit to "lock" the laser frequency to a specific hyperfine transition obtained through saturated-absorption spectroscopy [37, 54, 63, 64].

At room temperature, the atomic velocities in a rubidium vapor cell are large enough that the Doppler-broadened linewidth ($\sim$500 MHz) washes out all the hyperfine structure when using regular absorption spectroscopy. Saturated-absorption spectro-scopy involves a pump-probe setup that eliminates the problem of Doppler-broadened absorp-tion spectra, providing resolution high enough to distinguish the hyperfine structure of ^{87}Rb. The basic setup involves overlapping a strong pump beam with a weak, counter-propagating probe beam derived from the same laser, and monitoring the transmission of the probe beam. As the laser frequency is scanned, the pump and the probe come into resonance with different groups of atoms that have opposite velocities, as the positive-velocity group shifts into resonance with one beam, and the negative-velocity group shifts into resonance with the counter-propagating beam. This results in almost entire absorption of the weak probe beam, creating a Doppler-broadened absorption profile. This situation changes, however, for atoms with near-zero velocity, since the pump and probe frequencies are not Doppler shifted. When the laser frequency scans over a hyperfine resonance, the $v = 0$ atoms are resonant with both beams simultaneously, and as a result become saturated by the

strong pump, which increases transmission of the probe. This produces a Doppler-broadened transmission spectrum at most frequencies, with small peaks due to the increased transmission at the frequency of each hyperfine resonance [Fig. 2.6(a)]. These peaks are called "Lamb dips" (they appear as dips if the transmission spectrum is inverted to show absorption) [37], and their width is on the order of the natural linewidth ($\sim$38 MHz). Additional peaks are also observed in this spectrum, which occur at frequencies where atoms with a particular velocity have one hyperfine transition down-shifted into resonance with one beam, and another hyperfine transition up-shifted into resonance with the other beam. This type of resonance is referred to as a "crossover transition," and the increased transmission is due to depletion [37] rather than saturation. Depletion has a greater effect on the transmission, leading to the more prominent spectral features observed for the cross-over transitions.

2.3.6. Saturated-Absorption Spectroscopy Setup

The basic saturated-absorption spectroscopy optical setup is shown in Figure 2.7, which we use for the repumping master laser. This scheme sends a small amount of master-laser light through a $3/8''$ thick window (CVI Laser P/N PW-1037-C), which produces two parallel, weak reflections (one from each surface), while the majority of the light transmits through. The two reflected beams (probe beams) pass through a rubidium vapor cell, while the transmitted beam (pump beam) reflects from three mirrors and passes through the cell in the opposite direction, nearly overlapping one of the probe beams. We call the overlapped beam the "probe beam" and we refer to
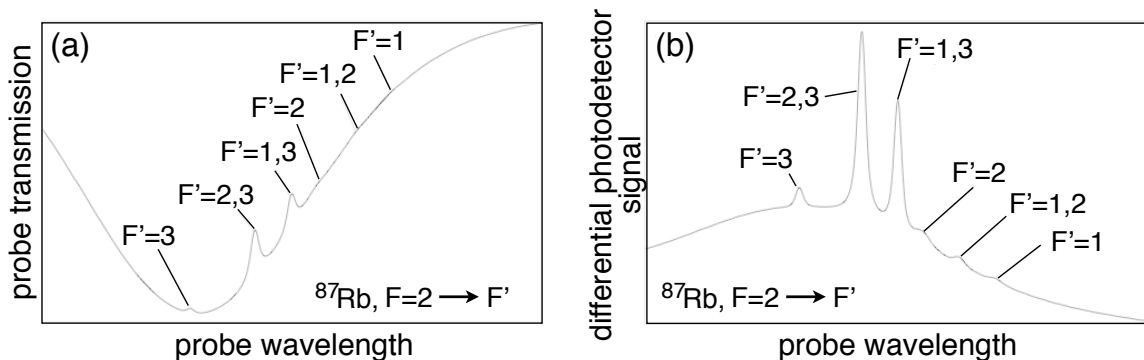
Figure 2.6. The saturated-absorption spectrum for the ^{87}Rb $F = 2 \rightarrow F'$ hyperfine transition. (a) Transmission of the probe beam as a function of the laser wavelength showing the saturated-absorption peaks. (b) Signal from the differential photodetector, which subtracts out the Doppler-broadened background, making the saturated-absorption peaks more visible. These spectra were provided by D. A. Steck.

the other beam as the "reference beam." We focus the probe beam and the reference beam onto a home-built, differential photodetector, comprised of two photodiodes and a circuit that subtracts the two signals. The reference beam simply exhibits the Doppler-broadened transmission profile, while the probe-beam spectrum also contains the saturated-absorption peaks [Fig. 2.6(a)]. The differential photodetector subtracts the Doppler-broadened background from the probe-beam spectrum, allowing us to view the saturated-absorption peaks more clearly [Fig. 2.6(b)].

We lock the repump laser to the $F = 1 \rightarrow F' = 1, 2$ crossover transition because it is the largest peak in the $F = 1 \rightarrow F'$ spectrum. The frequency of this transition is 78.5 MHz lower than the $F = 1 \rightarrow F' = 2$ repump transition (Fig. 2.4), so we use an 80 MHz AOM (IntraAction P/N ATM-801A2) to shift the frequency to resonance and to attenuate and shutter the beam as well.
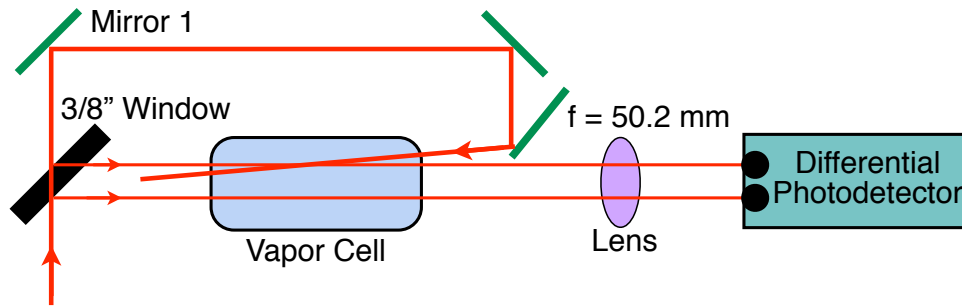
Figure 2.7. Schematic of the of the optical layout for saturated-absorption spectroscopy. A thick window splits the beam into a strong pump beam and two weak probe beams, which pass through a rubidium vapor cell and a lens into a photodetector that subtracts their signals. The pump beam wraps around and propagates through the vapor cell in the opposite direction, overlapping one of the probe beams.

To perform lock-in detection on the saturated-absorption signal, we modulate the laser injection current at 200 kHz, which in turn modulates the frequency of the laser. The photodiode signal, which registers the frequency modulation as shifts in intensity from moving on and off of resonance, is then fed into the lock-in amplifier to create an error signal for feedback control of the piezo and the current. The original saturated-absorption signal [Fig. 2.6(b)] is not a good candidate for feedback control because the desired frequency is at a maximum in intensity, so small frequency drifts produce undetectable changes in the magnitude of the signal. The error signal, however, generated from the frequency modulation and phase-sensitive lock in detection, has a dispersive line shape with a large slope at the frequency of interest [65], such that small changes in frequency create large, detectable changes in the magnitude of the signal.

An additional feature of the lock-in circuit is the ability to feed a small amount of the piezo output to the laser injection current. Though this does not improve its lock-in stability, it increases the mode-hop-free tuning range of the laser when scanning the piezo by changing the injection current to better match the frequency to the longitudinal mode of the cavity as it changes length.

The optical setup for locking the MOT master laser is slightly more complicated to avoid modulating the laser frequency directly, as in the case of the repump. MOTs are not very sensitive to the frequency of the repump light, so the small frequency modulation does not concern us. MOTs *are*, however, very sensitive to the detuning of the cycling transition, so a small amount of frequency modulation is not desirable. We modulate the saturated-absorption signal for the MOT laser by double-passing the pump beam through a 145 MHz AOM (IntraAction P/N ATM-1451A2), whose driving frequency is modulated from 143 to 147 MHz at a frequency of 200 kHz. The optical setup is the same as for the repump laser (Fig. 2.7), except we replace mirror 1 with the double-passing optics shown in Fig 2.5. Though we do not modulate the frequency of the detected reference beam directly, the frequency where the Lamb dips occur depends on the difference between the pump and probe frequencies, so the modulation moves the peak of the Lamb dip relative to the fixed probe frequency, modulating the intensity reaching the photodiode.

As with the repump, we lock the MOT laser to the largest feature in the saturated-absorption spectrum, the $F = 2 \rightarrow F' = 2, 3$ crossover transition. Due to the

frequency shift from the AOM in the saturated-absorption spectroscopy setup, the crossover transition occurs 278.3 MHz below the $F = 2 \rightarrow F' = 3$ cycling transition (Fig. 2.4). We shift the laser frequency to resonance using three 80 MHz AOMs; one that is double-passed and used to control the detuning (IntraAction P/N ATD-801A2), and one that also serves as an attenuator and shutter on the output of each slave laser (IntraAction P/N ATM-801A2). We send the zero-order diffraction beam from the AOMs on the output of each slave laser to a Fabry-Perot cavity (switching between them with a flip mirror) to verify each slave is locked to the master laser. This optical setup is illustrated schematically in Figure 2.8. We can change the frequency of the AOM that controls the detuning from 60 to 100 MHz, allowing us to detune the laser from 78.3 MHz below the cycling resonance to 1.7 MHz above it.

2.3.7. Fibers and Fiber Coupling

We divided our optical table into an optics side, containing the optical setup described above, and a vacuum-chamber side, where we perform the experiments. To transport the laser light to the experiment, we use single-mode, polarization-maintaining, FC/APC connected fibers (Oz Optics P/N PMJ3A3A-850-5/125-3-*-1) of various lengths (indicated by the *). We use Thorlabs collimators (Thorlabs P/N F220FC-B) that produce a nearly collimated, 2.1 mm diameter beam ($1/e^2$ intensity diameter) for most applications. Coupling a laser into a single-mode fiber can be a tedious process, and we typically use a setup that involves a one-to-one telescope to ensure collimation of the beam and a fixture to hold the collimator. The
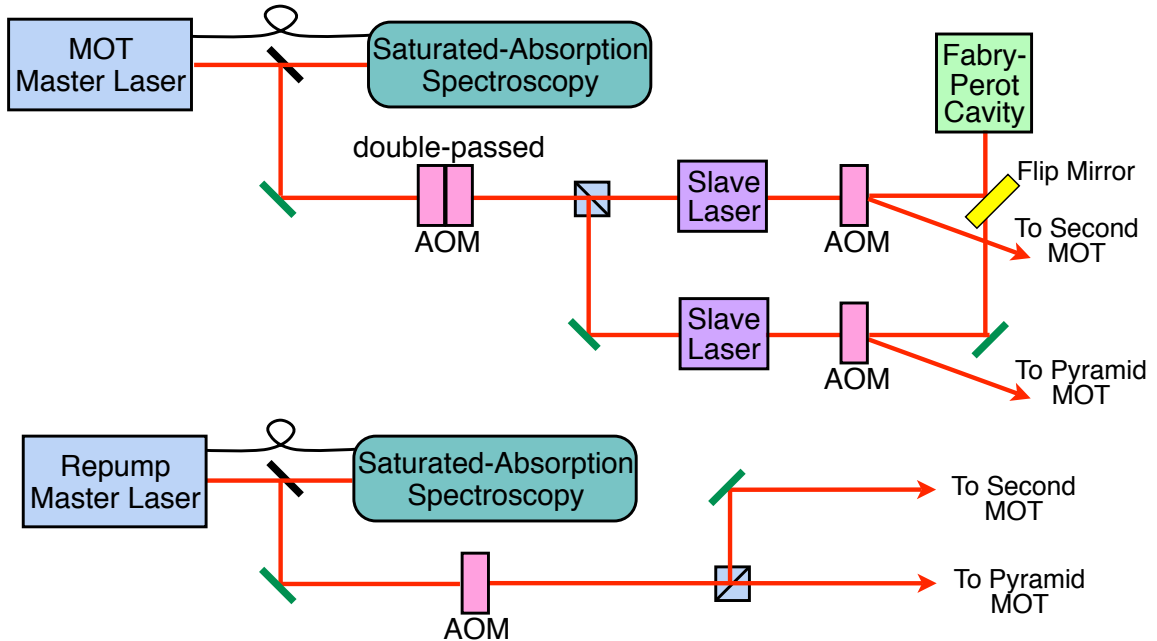
Figure 2.8. Schematic of the basic optical setup for producing the MOT-trapping and repump light, showing the relative layout of the master lasers, slave lasers, saturated-absorption spectroscopy optics, frequency-shifting AOMs, and Fabry-Perot cavity.

fixture attaches to a mirror mount and has two fine-adjustment screws that provide horizontal and vertical translation of the collimator (Fig. 2.9). The mirror mount allows for tilting, and the combination, along with appropriate placement of the second telescope lens, produces about 50% coupling efficiency for the non-Gaussian output of a diode laser.

For the pyramid MOT, we couple both the repump and MOT light into one fiber using a PBSC. We couple the repump light directly into the fiber collimator using the fixture, while we steer the MOT beam in using two mirrors. The fiber output has no collimating lens, so the light is essentially emitted from a point source, which we
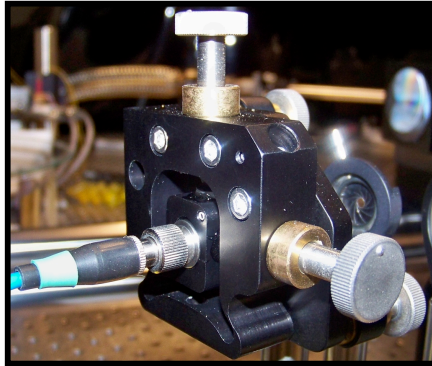
Figure 2.9. Picture of the fixture for coupling the fiber attached to a mirror mount, showing the fiber, collimator, and horizontal- and vertical-adjustment screws. The mirror-mount-adjustment screws are barely visible.

pass through a quarter-wave plate and collimate into a large diameter beam using a 200 mm focal-length, $3''$ diameter lens (Thorlabs P/N LA1353-B).

The second MOT requires the six traditional laser beams, so we purchased a six-way, fiber-optic beamsplitter array (Canadian Instrumentation and Research, custom design) with two inputs (one for the repump light and one for the MOT light) and six outputs. The power from each input is distributed fairly evenly ($\pm 3\%$ of the total output) amongst the six individual outputs, though we matched outputs with similar powers to form the three opposed beam-pairs. Temperature fluctuations of the box where the beam splitting occurs shifts the interference pattern of the overlapped, opposing beams enough to significantly distort the MOT, so we actively temperature stabilize this part of the device using a thermo-electric cooler and a laser-temperature-control board. Each output fiber connects to a large output collimator (Thorlabs P/N F810FC-780) that produces a 6.6 mm diameter beam ($1/e^2$ intensity diameter). We

secure each collimator in a mirror mount to provide steering capability, and affix a quarter-wave plate (Casix P/N WPL1225-lambda/4-780nm-M) in front of each output lens to produce the circularly-polarized light required for the MOT.

2.3.8. Optical Setup

Combined together, the different optical pieces of our experiment are impressive, covering about 25 square feet of our optics table with over 175 individual elements. A picture of the optical table is shown in Figure 2.10. Tao Li's dissertation [58] has a comprehensive schematic showing the placement of most elements.

2.4. Vacuum Chamber

To cool, trap and control atoms effectively, we carry out our experiments in ultra-high vacuum (UHV), which typically refers to pressures below $\sim 10^{-8}$ torr. Low background pressure significantly increases lifetimes of the trapped atoms by reducing the number of collisions with background gases. Our UHV system consists of a chamber divided into a high-pressure side ($\sim 10^{-8}$ torr) and a low-pressure side ($\lesssim 10^{-10}$ torr), separated by a differential-pumping tube [58]. Here, "high-pressure" simply indicates that the pressure is high relative to the low-pressure side. The differential-pumping tube consists of a cylinder, several inches long, with a tapered hole bored through the center [Fig. 2.11(a)]. Connecting the tapered end to the high-pressure side of the chamber impedes the flow of gas particles to the low-pressure side, helping to maintain a pressure differential between the two sides. The divided
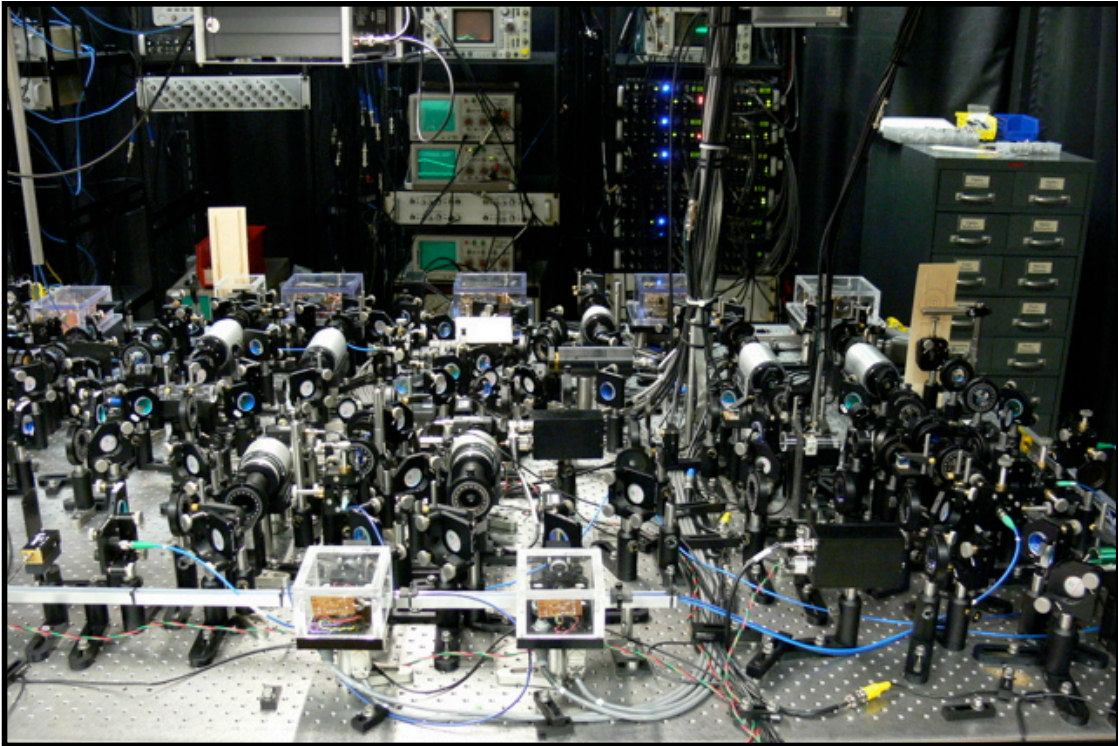
Figure 2.10. Picture of the optical table showing the lasers and multitude of optics needed to produce the MOT trapping and repump light. Two slave lasers are visible on the near side of the table and four master lasers are visible on the far side. Several racks of electronics that control and monitor the experiment can be seen in the background.

chamber allows us to trap large numbers of atoms at very low pressures, creating a versatile setup for a wide range of atom-optics experiments.

2.4.1. High-Pressure Side

The high-pressure side of the chamber includes the rubidium source, the mirrors for the pyramid MOT, an ion pump, a pair of anti-Helmholtz coils, and three pairs of Helmholtz coils. The main body of the chamber consists of a Kimball Physics "spherical square" (P/N MCF450-SS20400-A), which has two, 4.5″ conflat (CF) ports
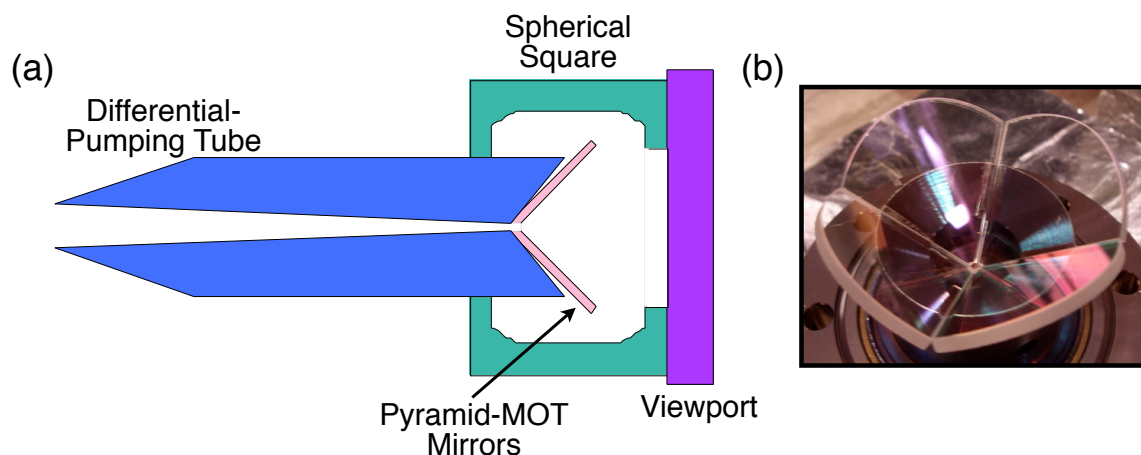
Figure 2.11. The high-pressure side of the chamber. (a) Schematic diagram of the differential-pumping tube, spherical square, pyramid-MOT mirrors, and viewport. (b) Picture of the pyramid-MOT mirrors mounted on the end of the differential-pumping tube, showing the small hole in the center.

opposite each other, plus four additional $2.75''$ CF ports spaced $90°$ apart. One $4.5''$ CF port connects to our custom-designed differential-pumping tube, which includes a structure for mounting the pyramid-MOT mirrors [Fig. 2.11(a)] that extends into the spherical square. The MOT light enters the chamber through a $4.5''$ CF, zero-length, AR-coated, quartz window (Larson Electronic Glass P/N VQZ-250-F4, AR coated by Spectrum Thin Films) that we connected to the other $4.5''$ CF port opposite the pyramid-MOT mirrors. The pyramid-MOT mirrors are tear-drop shaped Pyrex pieces with a notch at the vertex, cut with a water jet at a local company. The pyrex was reflection coated (by Spectrum Thin Films) with the constraint of minimizing the phase-shift differences of the MOT-light polarization upon reflection. We used Vacseal (SPI Supplies P/N 05100C-AB), a UHV cement, to affix the mirrors into place at the end of the differential-pumping tube prior to assembling the chamber. When

assembled, the mirrors form a pyramid with a small hole in the top [Fig. 2.11(b)]. A circularly-polarized, large-diameter beam incident on the pyramidal mirror structure will reflect in such a manner as to create the six counter-propagating beams (with the correct polarization) necessary to form a MOT inside the pyramid. Atoms trapped in the center of the structure do not experience a counter-propagating laser beam due to the small hole at the apex and get pushed through the hole and the differential-pumping tube into the low-pressure side of the chamber [66–68].

A crushed rubidium breakseal ampoule (Alfa 10315 1g) contained in a 1.33″ CF tee creates our source of rubidium vapor. We crushed the ampoule under vacuum using a steel rod welded to a 1.33″ CF blank that we attached to a 3″ long, 1.33″ CF, bellows (MDC P/N 400000) (Fig. 2.12). When the bellows are compressed, the rod makes contact with the ampoule, allowing us to crush it. We verified a successful crush by looking through a small viewport (Larson Electronic Glass P/N VPN-075-F1) attached to one end of the tee. Four small Kapton heaters (Minco P/N HK5161R78.4L12A) wrapped around the tee allow us to heat the rubidium source to increase the background pressure in the chamber and also to prevent rubidium from condensing on the viewport. We connected a valve (Varian P/N 951-5027) between the source and a 2.75″ CF port on the spherical square to control the amount of rubidium in the chamber.

We connected a 20 L/s ion pump (Varian Model VacIon Plus Starcell 20) to the top 2.75″ CF port of the spherical square to help maintain the vacuum, though we
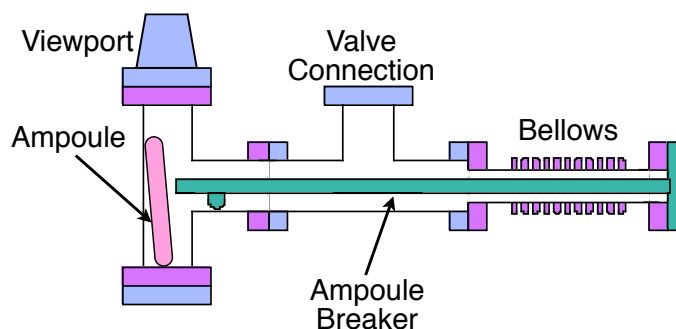
Figure 2.12. Schematic diagram of the rubidium source, showing the ampoule, viewport, valve connection, bellows and ampoule breaker.

do not use it anymore because the rubidium poisoned it early on. This does not pose a problem since we carefully control the flow of rubidium using the valve on the source, and other pumps in the system also help keep the pressure down. We attached a second valve (Varian P/N 951-5027) to the third 2.75″ CF port on the spherical square, allowing us to connect a turbo pump to the chamber for the initial pump down. The last port, located on the bottom of the spherical square, connects to a 2.75″ CF blank attached to a post for mounting on the optical table. Figure 2.13 shows the layout of the high-pressure side of the chamber.

Each anti-Helmholtz coil consists of 23 AWG, round magnet wire (purchased from MWS) wrapped 400 times around a 4.75″ diameter groove in an aluminum ring, held in place with high-temperature epoxy (Epoxy Technology P/N 343ND). The coils are spaced 4.2″ apart and generate an ~ 11 G/cm magnetic-field gradient in the trapping region with about 1.3 A of current. A temperature sensor (Analog Devices P/N AD590JH) is inserted into each aluminum ring, allowing us to monitor the temperature to ensure the coils do not overheat. We constructed three pairs
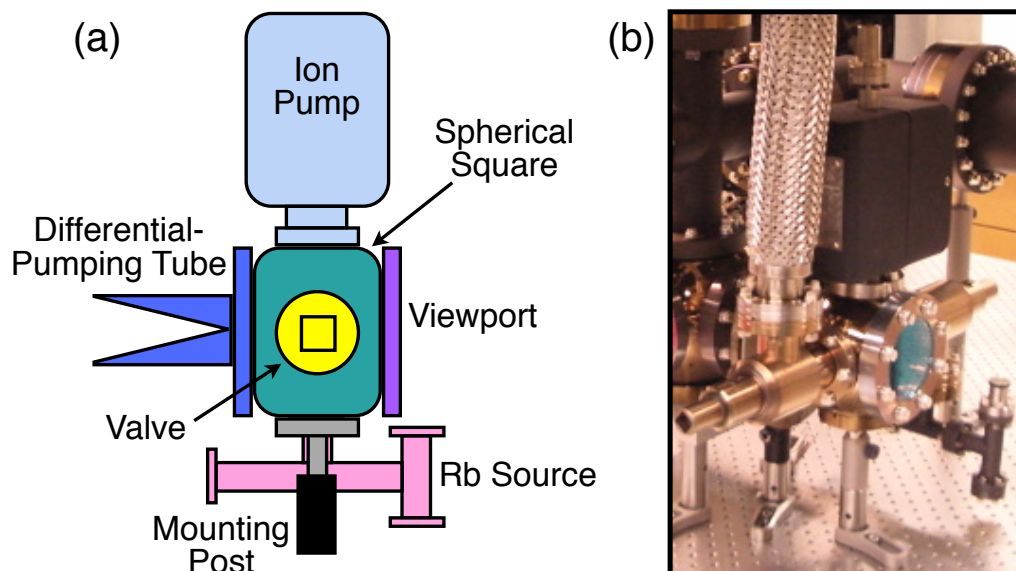
Figure 2.13. The different components connected to the spherical square. (a) Schematic diagram of the high-pressure side of the chamber, including the spherical square, differential-pumping tube, viewport, ion pump, rubidium source, valve to connect the turbo pump, and mounting post. (b) Picture of the high-pressure side of the chamber with all components visible except the differential pumping tube.

of Helmholtz coils (one for each dimension) by wrapping 10-conductor ribbon wire

(Mouser P/N 517-3801/10) around rectangular frames. We built the frames by joining

various lengths of $5/8'' \times 1/4''$ plexiglass to aluminum L-brackets with 24 hour epoxy

(GC Electronics P/N 10-347). We used double-sided tape to temporarily hold the

layers together during winding, then added small cable ties to permanently secure the

layers to the frames. The ends of the ribbon cable were outfitted with a double-row

socket (Mouser P/N 517-89110-0101), allowing us to connect the 10 conductors into

one long wire using a header (Digikey P/N 929665-09-36-N). We designed the coils

to produce at least a 1 G/A magnetic field at the center of each pair (2 G/A along

the anti-Helmholtz-coils' axial direction), with the constraint of fitting around the

spherical square and its surrounding equipment (including the anti-Helmoltz coils).
The resulting coil-pair specifications are detailed in Figure 2.14.

The current supplied to the Helmholtz and anti-Helmholtz coils comes from home-built current drivers backed by a 40 V, 10 A power supply (that we usually run at 30 V). The current drivers provide several amps of bi-directional drive capability, manual current control, a current-modulation input, digital on/off switching, and a small LCD screen that conveniently displays the amperage. Each pair of Helmholtz coils has its own dedicated driver, while the anti-Helmholtz coils have one driver for each coil (the current has to go in opposite directions). The two anti-Helmoltz-coil drivers are actually slightly different circuits, connected in a master-slave config-uration. In this configuration, the master board controls the current output of the slave board, which is proportional to the master current, and the proportionality factor can be changed manually. Though it has not really been a problem, each board has an automatic shutdown should the temperature of the coils or the high-current op amps get too high. There are three red LEDs that indicate the different modes of shutdown: user shutdown, coil overheating, and chip overheating. Additionally, an LCD screen displays the temperature of each coil if an IC temperature sensor (AD590) is affixed to the coil. Typically, we operate the anti-Helmholtz coils at -1.21 A and -0.98 A for the master and slave, respectively, while the x, y, and z Helmholtz coils are set to 0.45 A, -0.70 A, and 0.00 A respectively, which places the

Coil	Dimensions (inches)	Separation (inches)	Turns	Gauss/Amp at Center
x	12 x 9	6.5	3	1.7
y	12.4 x 10.8	6.2	3	1.7
z	13.4 x 13.4	8	6	2.6
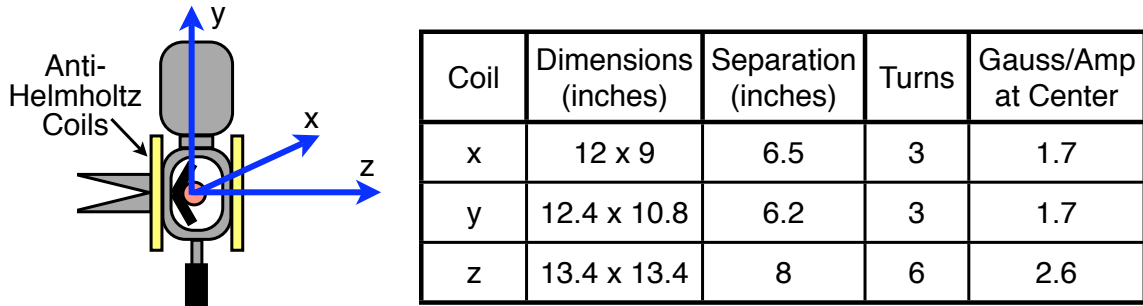
Figure 2.14. The x, y, and z Helmholtz-coil-pair specifications for the pyramid MOT, including a diagram indicating the orientation of the three dimensions relative to the anti-Helmholtz coils and the low-pressure vacuum-chamber assembly.

MOT in front of the hole in the pyramid-MOT mirrors. We note that these values may need adjustment over time to maintain the position of the MOT.

2.4.2. Low-Pressure Side

The low-pressure side of the chamber includes several vacuum pumps, mirrors for dumping the dipole-trap beam, a pair of anti-Helmholtz coils, three pairs of Helmholtz coils, and an 8″ long, fused-silica (Spectrosil 2000) vacuum cell where we conduct the experiments. The main body consists of a Kimball Physics "spherical cube" (P/N MCF450-SC60000-C), which is essentially a cube with rounded corners and a 4.5″ CF port on each face. Inside the cube we mounted two mirrors (Thorlabs P/N BB3-E03) (Fig. 2.15) to reflect the dipole-laser light out of the chamber and into a beam dump. We accomplished this by bolting a custom-built base plate and two mirror mounts to a pair of Kimball Physics groove grabbers (P/N MCF450-GG-CT02-A), specifically designed for mounting items in their chambers (Fig. 2.15). The two (opposite facing) ports dedicated to dumping the dipole-trap beam are sealed with 4.5″ CF, zero-length,
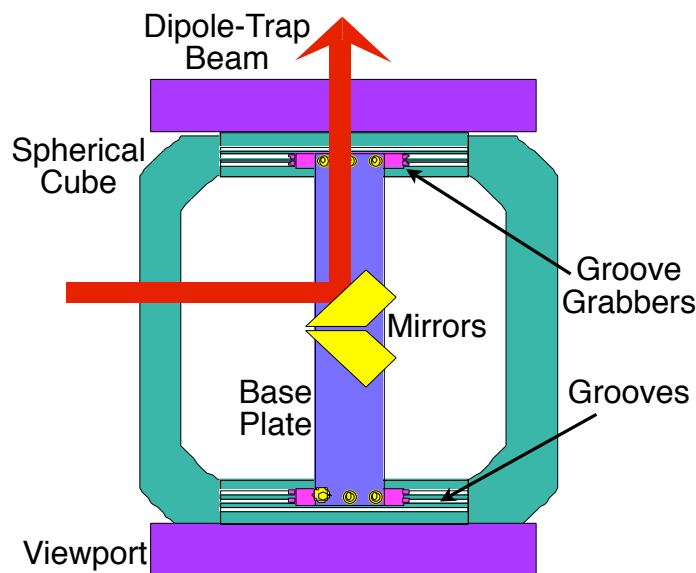
Figure 2.15. Schematic diagram of the low-pressure side of the chamber viewed from the top, showing the spherical cube, viewports, grooves, groove grabbers, mirrors, and the base plate for mounting the mirrors.

AR-coated, glass viewports (Larson Electronic Glass P/N VP-250-F4, AR coated by Spectrum Thin Films).

The top port connects to a 4.5″ CF cross, where we connected a 75 L/s ion pump (Varian VacIon Plus Starcell 75), a Ti-sublimation pump (Duniway Stockroom P/N TSP-275-003) and a valve (Varian P/N 951-5027) to connect to the turbo pump for the initial pump down (Fig. 2.16). The ion pump runs continuously after the chamber is pumped down, and is primarily responsible for keeping the background pressure low. The Ti-sublimation pump works by coating the chamber walls surrounding the titanium filament with clean titanium, which then reacts with any colliding background gases, reducing the pressure. We attached the Ti-sublimation pump to the cross via a large elbow (Fig. 2.16) to prevent the filament from spewing titanium
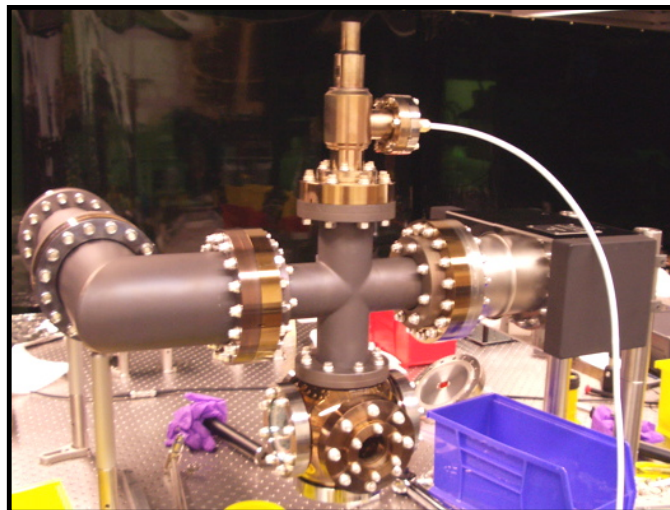
Figure 2.16. Picture of the CF cross mounted on the spherical cube, showing the attached ion pump (right), valve (top), elbow and Ti-sublimation pump (left).

into delicate parts of the chamber, and we only run it occasionally to reduce small increases in pressure. We do this by running 50 A of current through the filament several times for 2 minutes each time (a process referred to as "flashing"), which temporarily increases the background pressure for a few minutes until the released titanium begins pumping.

The bottom port connects to a 4.5″ CF blank that we modified by inserting five electrical feed-throughs where we mounted five getters (SAES P/N ST175/HI/16-30/300C). Getters provide additional vacuum pumping capability, especially for hydrogen, which dissolves and diffuses into the bulk getter material. To maintain the pressure in the chamber, we occasionally run current through the getters (8.5 A, for 2 minutes, several times), which improves their pumping efficiency after a brief, initial increase in pressure. We typically do this in conjunction with flashing the Ti-

sublimation pump, which pumps the hydrogen released by the getters. We alternate between the Ti-sublimation pump and the getters, waiting for the initial pressure increase to subside between each start. We bolted the modified blank to a steel base plate with a circular cut-through such that the getter connections are accessible, then secured the steel plate to the optical table to mount the chamber (Fig. 2.17).

The large-bore side of the differential-pumping tube attaches to one of the two remaining 4.5″ CF ports in the spherical cube. The end of the tube extends out into the chamber, over the location of the dumping mirrors (Fig. 2.17), which we placed lower than the end of the tube so as not to interfere with the exiting atomic beam from the pyramid MOT. We mounted a custom-built, square vacuum cell (by Hellma) (Fig. 2.17) onto the remaining port, opposite the differential-pumping tube. Atoms launched from the pyramid MOT through the differential-pumping tube pass into the vacuum cell, where they are captured by the second, six-beam MOT [69]. For this MOT, four of the beams are aligned parallel to the table and enter the cell at 45° angles, while the other two beams are mounted vertically above and below the cell. This design rapidly transports large numbers of atoms into the low-pressure vacuum cell while maintaining the pressure differential between the two chambers.

Initially, we valiantly attempted to construct our own vacuum cell, using pieces of Pyrex cut with a water jet and Vacseal. We started by verifying we could achieve UHV pressures with a fused-silica window Vacsealed onto a conflat flange. We refined our technique over many iterations, reaching pressures in the 10^{-8} torr range that survived
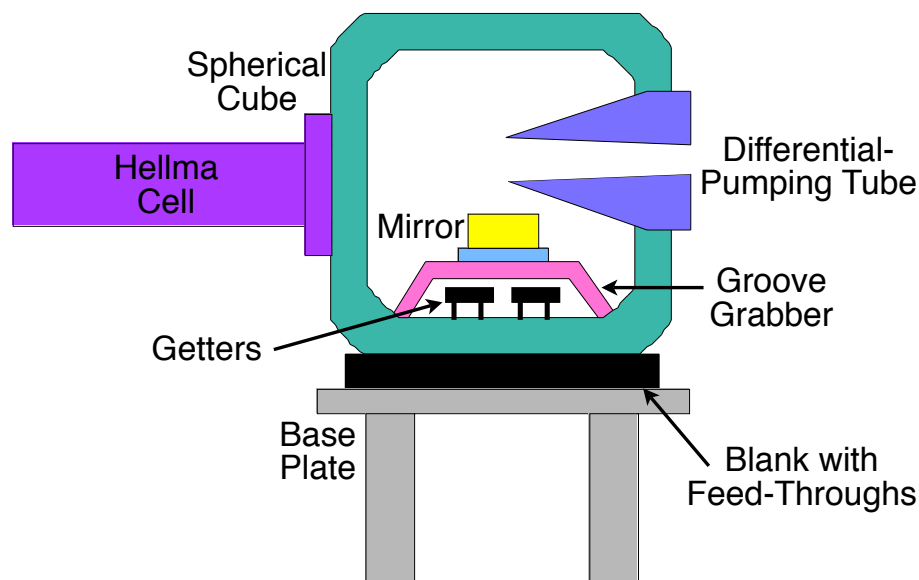
Figure 2.17. Schematic diagram of the low-pressure side of the chamber viewed from the side, including the spherical cube, differential-pumping tube, Hellma cell, dumping mirror, groove grabber, getters, the blank containing the electrical feed-throughs for the getters, and the mounting base plate.

bake outs to 200°C and passed helium leak tests on several occasions. Creating a UHV

seal with Vacseal required a meticulous, multi-step process, with four key components:

an even application of Vacseal to both contact surfaces, a quick (30 minute) bake

at 170°C to evaporate some of the solvents, contacting the surfaces while still hot,

and baking overnight at 250°C while keeping reasonable pressure on the contacted

surfaces. After experimenting with the fused-silica window, we put our efforts towards

building a Pyrex vacuum cell. The multiple pieces needed to construct the vacuum

cell significantly complicated the aforementioned sealing process. We started using

teflon tape [Fig. 2.18(a)] to guide the application of the Vacseal and restrict it from

flowing during a brief (10 minute) bake at 170°C. This brief bake was introduced to
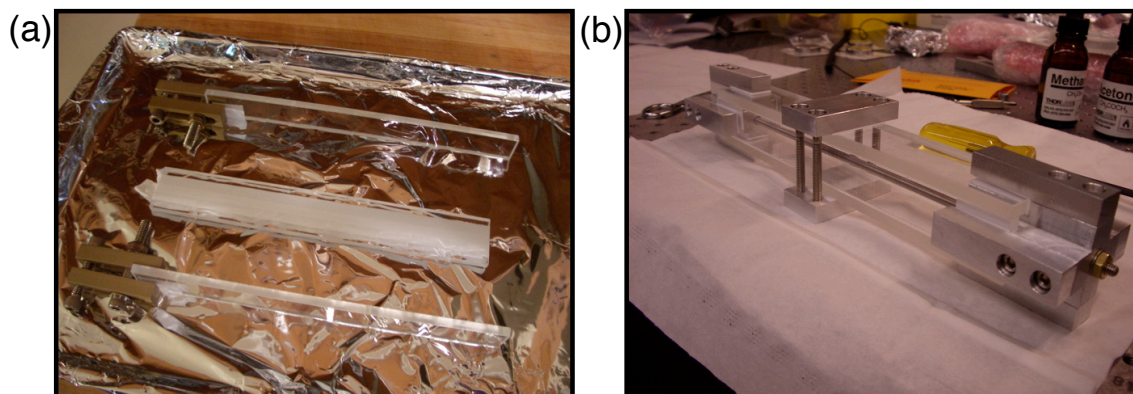
Figure 2.18. Pictures showing the assembly of our home-built vacuum cell. (a) We used teflon tape to prevent the Vacseal from flowing during a 10 minute bake. (b) The jig we designed to hold the four sides of the cell together during the baking process.

prevent the Vacseal from dripping while we mounted the pyrex pieces in a jig that held them in place during the 30 minute bake [Fig. 2.18(b)]. This jig held the pieces together during the longer bake as well. We also had to assemble the vacuum cell in two parts, first constructing the main body (including the overnight bake), then attaching the end piece to the body and the body to the circular flange with a second overnight bake. Polishing the cut edges of the pyrex pieces that contacted the flat surfaces proved advantageous as well. While we met with some success after four attempts, reaching a pressure of $\sim 1 \times 10^{-7}$ torr before baking our home-built cell (after the bake we lost a couple orders of magnitude), we were unable to reliably produce a robust, leak-free seal along all the joints. We eventually abandoned this effort and purchased a custom cell from Hellma.

A second challenge came from devising a reliable, leak-free method for connecting the Hellma cell to the vacuum chamber since the Vacseal approach did not pan out.
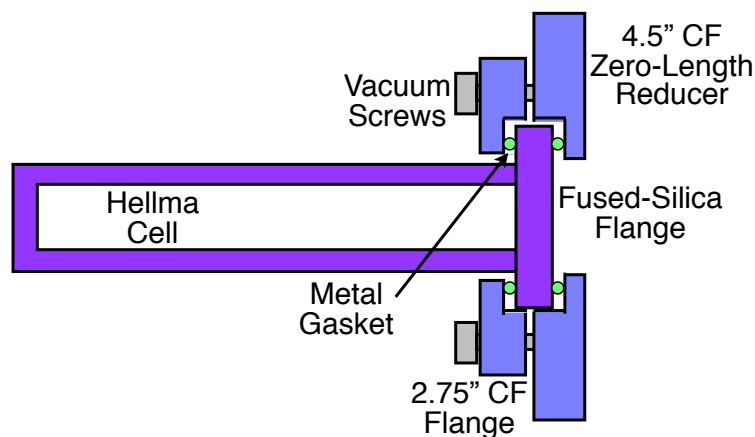
Figure 2.19. Schematic diagram showing the cross-section of the Hellma cell mounting apparatus, including the 4.5″ zero-length reducer, the 2.75″ flange, lead-alloy gaskets, vacuum screws, Hellma cell, and fused-silica flange.

To this end, we modified a 4.5″ to 2.75″ CF, zero-length reducer and a 2.75″ CF flange to have recesses that fit the circular, fused-silica flange (Fig. 2.19). We then slipped the modified, 2.75″ CF flange over the Hellma cell, sandwiching the fused-silica flange between the two steel CF flanges, with thin lead-alloy gaskets (Indium Corp Indalloy 165) placed between the metal and fused silica surfaces [70]. The gaskets are compressed with standard, silver-plated vacuum screws equipped with pairs of opposed Belleville disc springs (MSC 87779211). The gasket underneath the flange forms the vacuum seal by flattening onto the fused-silica and steel surfaces during compression, while the second gasket simply serves as padding to prevent the steel from cracking the fused-silica flange. Initially we tried using gold gaskets, which performed well on circular, fused-silica blanks, however, we cracked a Hellma cell trying to compress the gold gaskets to eliminate a leak. This led to our use of the softer lead-alloy gaskets. A picture of the mounted Hellma cell is shown in Figure 2.20.
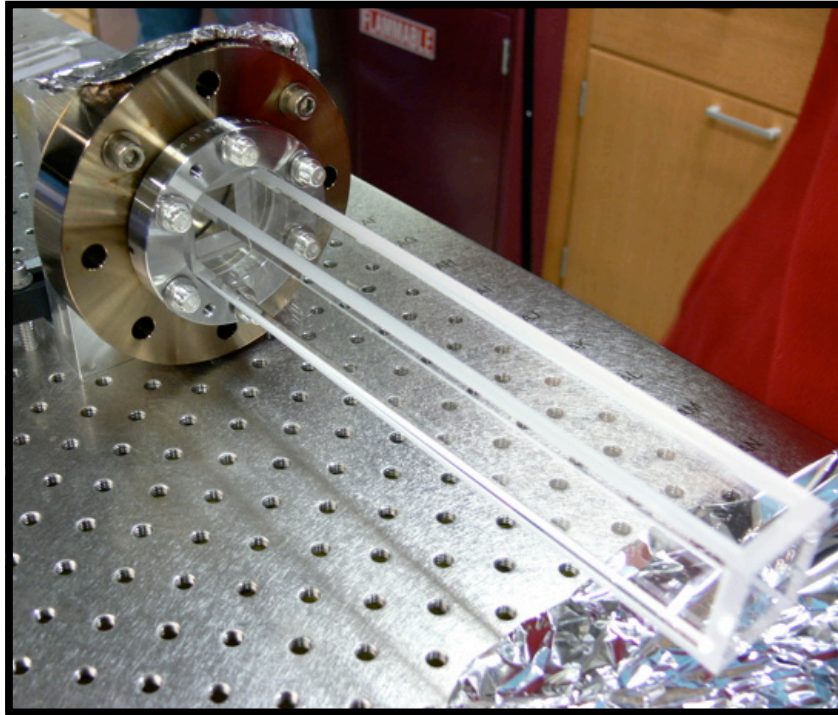
Figure 2.20. Picture of the Hellma cell mounted using the modified 2.75″ and 4.5″ CF flanges with the lead-alloy gaskets.

To assess the performance of the gold and lead-alloy gaskets, we leak-tested the various seals by attaching the component to our turbo-pump station and flooding the sealed area with helium. During the flooding we monitored the helium pressure on the turbo-pump station's residual gas analyzer to detect any leaks. We performed the leak tests before and after a brief bake at 200°C, and we applied additional compression as needed to fix any leaks that appeared.

The anti-Helmholtz coils for the second MOT are similar to those for the pyramid MOT, consisting of the same wire wrapped 216 times around a circular, Delrin frame with a 40 mm diameter. The coils attach to the 2.75″ CF flange securing the Hellma

cell, and are separated by 50 mm, such that the Hellma cell just fits in between them (Fig. 2.21). These coils generate about a 12 G/cm magnetic-field gradient in the trapping region at 0.5 A of current. We constructed the Helmholtz coils in a fashion similar to the pyramid-MOT Helmholtz coils described above, wrapping ribbon wire around an aluminum frame that we bolted to the optical table. We chose the specifications to accommodate the existing equipment, produce a field of about 1 G/A at the center of each coil pair (larger along the anti-Helmholtz-coils' axial direction), and ensure the frame formed a three-dimensional, rectangular box. The specifications for the three pairs of Helmholtz coils are given in Figure 2.21.

The coil drivers for the second set of Helmholtz and anti-Helmholtz coils are the same as described earlier, except we do not monitor the temperature of the anti-Helmholtz coils. To form a fast-loading, strong MOT in the Hellma cell, we typically operated the anti-Helmholtz coils at 0.68 A for the master and slave, and the x, y and z Helmholtz coils at 0.02 A, -0.44 A, and -0.42 A, respectively. The Helmholtz-coil values were chosen to prevent stray magnetic fields (i.e. earth's) from launching the atoms during fluorescence imaging (see Section 2.6). Our experiments relied heavily on controlling the location of the MOT, so we altered these values significantly depending on the needs of each experiment.

2.4.3. Vacuum Chamber Assembly

Achieving very low pressures in a vacuum chamber is as much superstition as it is science; every group has slightly different procedures for cleaning and prepping the

Coil	Dimensions (inches)	Separation (inches)	Turns	Gauss/Amp at Center
x	10 x 4.5	6	6	1.1
y	5.5 x 7	10	10	0.5
z	6 x 10	4.5	4	1.4
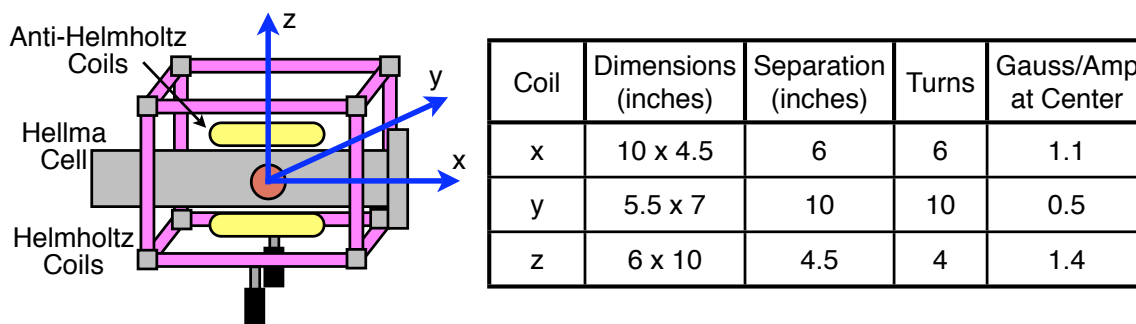
Figure 2.21. The x, y, and z Helmholtz-coil-pair specifications for the second MOT, including a diagram showing the arrangement of the Helmholtz and anti-Helmholtz coils around the Hellma cell, as well as the orientation of the three dimensions relative to the Hellma cell and optics table.

vacuum components that they swear by are critical to reaching optimum performace. The main tenets are generally the same [71–73], and here we will document our preferred practices.

Prior to assembling the different vacuum pieces (tees, crosses, valves, etc.), we adhered to a strict baking and cleaning procedure. We start by baking the components at 480°C for 48 hours, which removes some dissolved hydrogen in the stainless steel and forms an oxide layer on the surface that prevents hydrogen from diffusing through [74, 75]. Parts that were machined or modified in-house had to undergo extensive cleaning prior to baking, involving sonication in alconox and de-ionized water, then rinsing with acetone and methanol. Though all the pieces are machined from 304 or 316 stainless steel, the finishes on the outer surfaces vary by finishing method, producing remarkably different colors and hues after baking. Some of the more exoticly-hued pieces are shown in Figure 2.22. After baking, we clean each piece with spectroscopic grade acetone and then spectroscopic grade methanol, drying each
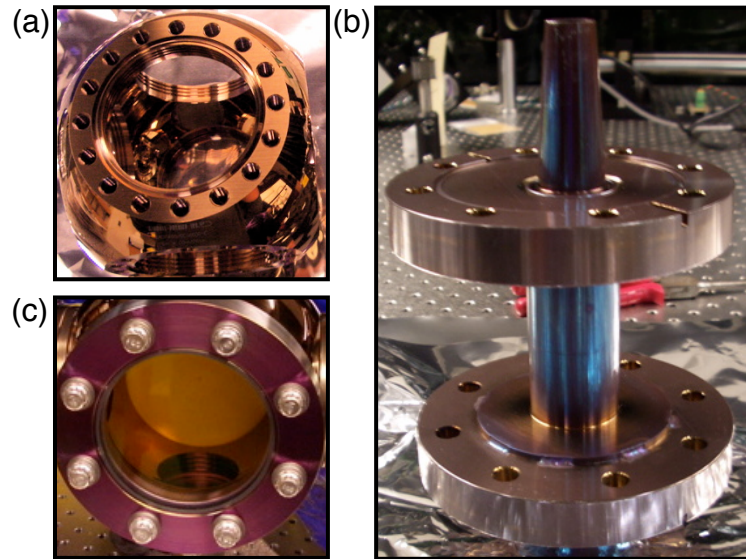
Figure 2.22. Pictures of three of the more stunning vacuum components after baking for 48 hours at 480°C. (a) the spherical cube, (b) the differential-pumping tube, and (c) an AR-coated viewport.

component after each rinse with cool nitrogen gas (from an LN_2 dewar). The cleaning removes any contamination that may have occurred during the baking process. Once clean, we wrap each component in oil-free, UHV aluminum foil (All Foils UHV aluminum foil) to await assembly.

We assembled the chamber in pieces, taking care to cover any exposed CF ports with UHV aluminum foil and clean each copper gasket with spectroscopic grade acetone and methanol to prevent contamination. Certain components required assembly in a specific order, such as placing one of the pyramid-MOT anti-Helmholtz coils around the differential-pumping tube prior to attaching the spherical cube. Additionally, we installed the other set of anti-Helmholtz coils and both sets of Helmholtz coils after baking the chamber out as they were not designed for high temperatures.

2.4.4. Baking Out the Vacuum Chamber

A common practice involves baking a vacuum chamber (typically at temperatures near or above 200°C) while pumping on it to remove excess water vapor and other residual gases. This is usually the last step in the meticulous process to achieve UHV pressures. As with cleaning the vacuum components, a plethora of bake-out methods exist, each one unique to the lab and the chamber. We baked out our chamber four times (for reasons we will explain below), and here we will describe the process.

In order to bake out our chamber, we built an oven around it made of UHV aluminum-foil-covered fire bricks (Thermal Ceramics) (Fig. 2.23). This provided sufficient insulation such that we could heat the inside to at least 200°C without posing a risk to the lab. We wrapped many meters of heater tape (Omega) around the chamber and placed more on the floor of the oven, then inserted 16 thermo-couples (wire from Omega, P/N GG-J-20-25) at various locations to monitor the temperature in different regions. We powered the heater tape with variable transformers (Circuit Specialists P/N TDGC2-2) and displayed the temperature data online with the help of two home-built, ethernet enabled thermocouple monitors that interfaced with the thermo-couples.

We initially pumped down and baked out our chamber without the Hellma cell to test all the vacuum seals and our various pumps, and to see what pressure we could achieve. To start this process, we attached our turbo-pump station to the valves on the spherical cube and the spherical square to pump on both the high-
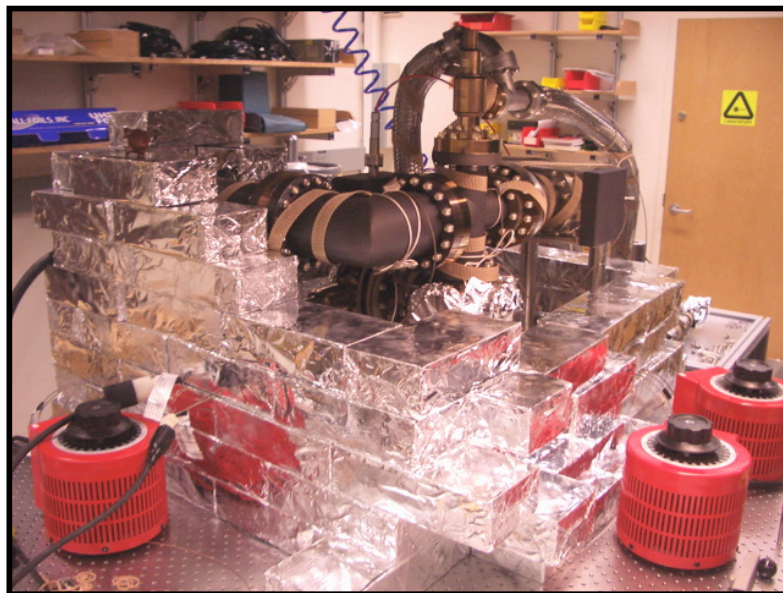
Figure 2.23. Picture of the partially-constructed oven made of vacuum-foil-covered fire bricks we used to bake out the vacuum chamber. The cross and elbow wrapped in heater tape, the top of the spherical cube and a few of the red variacs used to control the temperature are visible in this picture.

and low-pressure sides of the chamber. The turbo-pump station consists of a turbo pump (BOC Edwards P/N EXT 70H 24V) backed by a roughing pump, a residual gas analyzer (Stanford Research Systems RGA 300) and various pneumatic valves. This system can pump down to pressures on the order of 10^{-8} torr.

We started slowly heating up the oven after reducing the pressure to about 2×10^{-8} torr with the turbo pump, taking care not to raise the temperature too quickly or unevenly. This avoided rapid thermal expansion that could have compromised the vacuum seals or the integrity of various components. We raised the temperature to $215°C$ over the course of two and a half days, even though the viewports had $200°C$ temperature rating and the cable for the Ti-sublimation pump was non-bakable. We

held the temperature for seven days, turning the ion pumps on after two days, and occasionally flashing the Ti-sublimation pump and the getters. We cooled down over one day, and noticed the Ti-sublimation pump was not working well. It turns out the high temperature fried the inside of the connector, and we had to purchase a new cable and filament. Replacing the burnt one required bringing the chamber up to pressure, thus, bake out number two, which was conducted in a similar fashion. For both of these bake outs we had a quartz window sealed with a gold gasket in place of the Hellma cell. Once we installed the Hellma cell with the lead gasket, we baked out for a third and (supposedly) final time. However, the power went out briefly near the end of the bake out and partially vented the chamber, requiring a fourth, brief bake out. Our meticulous work paid off, as we achieved a pressure $\lesssim 10^{-10}$ torr on the low-pressure side of the chamber. We crushed the rubidium ampoule after all the baking was complete.

2.5. The Dipole-Trap Laser

In our experiment we employ a single-beam, optical dipole trap (Section 1.6), which requires high powers and large detunings from the atomic resonance. Initially, we tried to form a dipole-trap using light produced by a tapered amplifier designed and built by Matthias Fuchs [76]. However, the presence of resonant light in the beam lead to substantial atom loss, impacting its usefulness as a dipole-trap laser. We attempted to remove the resonant light by placing a rubidium vapor cell in the

beam path, but we only met with paltry success. Even with tripling the beam path through the cell and significant heating of the cell to increase the vapor pressure, atoms remained visible for no more than $80 - 90$ ms in the dipole trap. Eventually, we abandoned the effort and installed a high-power, Ytterbium-doped fiber laser (SPI Lasers model SP-M-20-A-1090-N-20-DC) that successfully traps the atoms.

The fiber laser has a wavelength of 1090(5) nm, yielding a detuning of over 300 nm from the 780 nm D_2 line of ^{87}Rb, and a maximum power output of 20 W. The laser emits an unpolarized, multiple-longitudinal-mode, nearly Gaussian, collimated output beam with a measured beam waist of 1.9(1) mm ($1/e^2$ intensity radius).

We control the fiber laser with a home-built interface box, which has a manual on/off switch (the laser cannot be turned on with the computer if this switch is off) and provides manual or computer control of the output power with the flip of a switch. A modulation input with digital switching capability provides the computer control. Three LCD screens display the manual CW set-point, power output and laser temperature, and the box sports a large, red emergency-shutdown button should something go catastrophically wrong (Fig. 2.24).

To create a single-beam, optical dipole trap, we focus the beam to a 30.9(5) μm waist ($1/e^2$ intensity radius) with a 200 mm focal-length lens. We considered several factors when deciding the focal length, including spherical aberration, beam waist, and positioning the lens not to be too close to the end of the Hellma cell. The output collimator and focusing lens are housed in a lens tube that we mounted on

Figure 2.24. Picture of the home-built, fiber-laser control box, including several LCD displays showing the manual CW set-point, power output and laser temperature, and the emergency stop button.

two translation stages and a precision air-bearing stage (Aerotech model ABL 10100-LT), allowing for three-dimensional control of the dipole-trap beam. The precision stage (air cart) has sub-micron accuracy and repeatability, and we are able to control its position, speed, and acceleration with the computer. This allows us to transport dipole-trapped atoms from the MOT region of the Hellma cell to other regions that have improved optical access.

We aligned the dipole-trap beam to pass through the end of the Hellma cell, intersect the MOT, then reflect from one of the dumping mirrors into a custom-built beam dump [Fig. 2.25(b)]. We placed a long-focal-length lens after the vacuum viewport to help the expanding beam fit into the beam-dump entrance. Requiring the beam to intersect the MOT and the dumping mirror resulted in a beam path that was not parallel to the table nor to the long axis of the Hellma cell (Fig. 2.25). Since we aligned the air cart parallel to the Hellma-cell axis, translating the dipole trap shifted the focus in all three dimensions (as opposed to just axially) and misaligned the beam with the dumping mirror. Initially, this did not pose a problem, but later
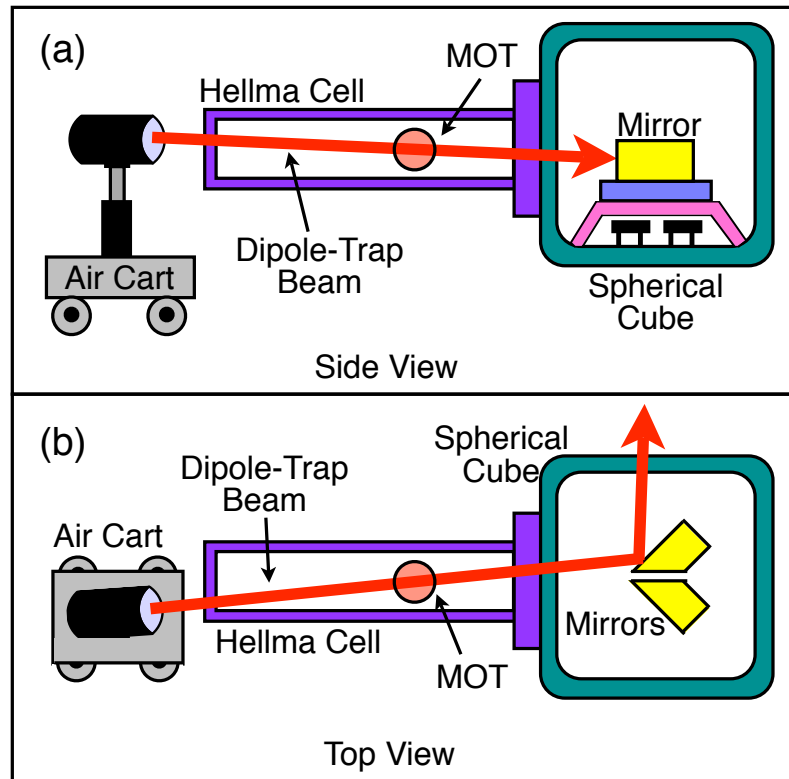
Figure 2.25. Schematic diagram showing the alignment of the dipole-trap beam with the MOT and the dumping mirrors, including the air cart, dipole-trap beam, Hellma cell, MOT, spherical cube and dumping mirrors. (a) Side view illustrating the angle between the dipole-trap beam and the Hellma-cell axis. (b) Top view illustrating how the dipole-trap beam is not parallel to the air-cart-translation direction and the Hellma-cell axis.

we had to change the air cart position and the beam height for the one-way-barrier cooling experiment, which required translating the atoms in the dipole trap.

To overlap the dipole-trap laser with the MOT, we aligned a resonant beam first, then overlapped the dipole-trap beam with the path of the resonant beam using two irises. The resonant beam easily blows the MOT atoms away without being very centered on it, making the initial alignment fairly simple. The dipole-trap beam, on the other hand, must be very near the MOT to have a visible effect due to its large

detuning. Once the dipole-trap beam is near the MOT, we use the translation stages and/or the magnetic fields (from the Helmholtz coils) to improve the overlap, looking for the position where the dipole-trap beam most greatly affects the MOT.

2.6. Imaging System

We image the atoms using a charge-coupled-device (CCD) camera (Finger Lakes Instruments MicroLine model with KAF-0402ME sensor). Though not ideal for our work, it sufficed for the duration of the one-way-barrier experiments, with the shutter posing our most significant challenge. The shutter had a penchant for sticking and wore down quickly with repeated use, requiring frequent cleaning and repair.

We placed the camera perpendicular to the dipole-trap axis (Fig. 2.26), and affixed a manual lens (Nikon Micro-Nikkor 55mm f/3.5, purchased used) on the camera to focus the light onto the CCD. In an effort to reduce unwanted light from reaching the CCD, we installed a combination of a laser-line filter (Semrock P/N LL01-780-11.9-D) and AR-coated RG715 Schott glass (Newport Industrial Glass RG 715, AR coated by CVI) in between the lens and the CCD. The laser-line filter only passed 780 nm light until ∼575 nm, at which point it became highly transmissive at shorter wavelengths. To remedy this, we added the Schott glass to remove any light with a wavelength shorter than 575 nm. Later we removed the laser-line filter as it produced significant, non-stationary fringes in our images (the Schott glass blocks light with
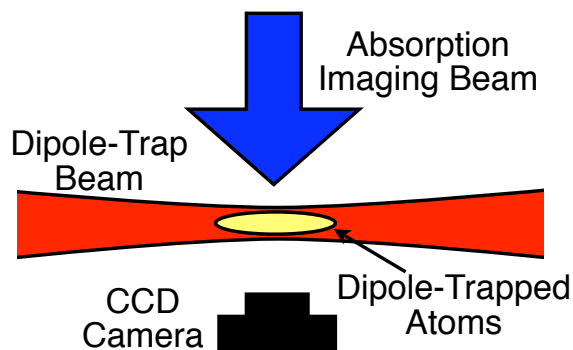
Figure 2.26. Schematic diagram showing the orientation of the CCD camera and absorption-imaging beam relative to the dipole trap.

wavelengths shorter than 700 nm). The entire imaging system (CCD, filter and lens) has a resolution of 24.4 μm/pixel.

We image the atoms using either fluorescence imaging or absorption imaging, depending on the needs of the experiment. Fluorescence imaging involves collecting the light emitted by the atoms when they are illuminated with the MOT-trapping beams. This technique is useful for calculating atom numbers and measuring temperatures, but does not have particularly good spatial resolution because the atoms move noticeably during the time of the illumination pulse. To fluorescence image the atoms, we typically flash the MOT-trapping and repump beams at the intensity and detuning used to form the MOT for 20 ms. The long interaction time ensures a strong signal for atom-number and temperature calculations despite the small number atoms. In absorption imaging, a weak, resonant beam illuminates the atoms, such that any light passing through becomes absorbed. The CCD then images the unabsorbed light, and the absence of light in the image indicates the location of the atom cloud. This

imaging method provides good spatial resolution, but is fairly sensitive to intensity fluctuations.

We placed our absorption-imaging beam on the other side of the Hellma cell opposite the camera (Fig. 2.26), and derived the light from the zero-order diffraction beam produced by the AOM that controls the second-MOT intensity. Since the absorption-imaging beam and the MOT beams are never on at the same time, using the same beam for two different functions does not pose a problem. To shift the zero-order beam to resonance and control its intensity, we pass it through another 80 MHz AOM (Isomet P/N 1205C-1) and then couple it into a fiber. We use a large output collimator (same as for the six MOT beams) to increase the width of the beam for imaging, since we need a nearly-uniform intensity over the spatial extent of the atom cloud. Next, the beam passes through a $2°$ wedge prism placed at $45°$ (Thorlabs P/N PS810), which reflects about 10% of the beam (Fig. 2.27). The wedge shape prevents fringes that can result from the surfaces of the prism forming an etalon. We focus the transmitted beam into our home-built pulse-stabilization circuit, which integrates the power of each absorption pulse up to a set value to maintain a consistent integrated intensity (as opposed to pulse length) from one pulse to the next pulse. The reflected beam illuminates the atoms after passing through an anamorphic prism pair ($\times 4$ magnification) that horizontally expands the beam even further, since the atoms spread out over a few millimeters in the longitudinal dimension of the dipole trap. The absorption imaging pulse is typically about 45 μs, and we shift the laser
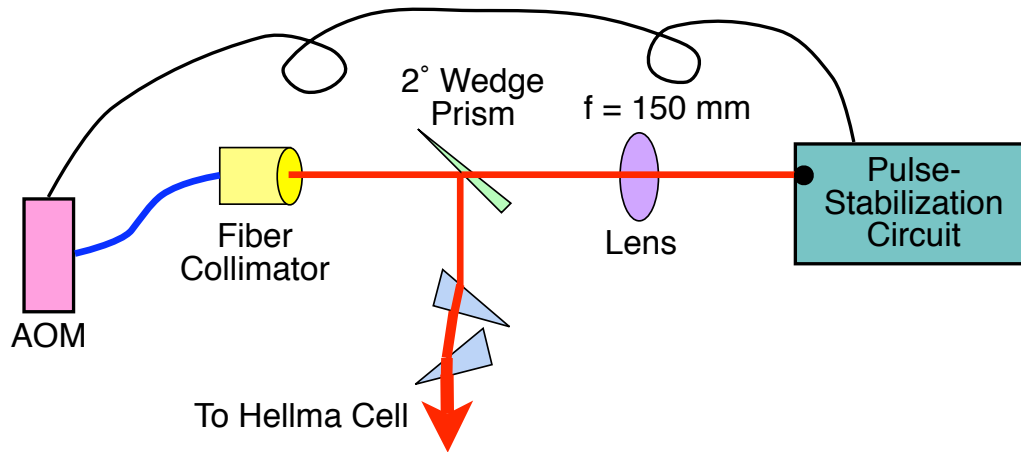
Figure 2.27. Schematic diagram of the absorption-imaging optics showing the AOM, fiber-output collimator, 2° wedge prism, anamorphic prism pair, lens, and pulse-stabilization circuit.

frequency very close to the $F = 2 \rightarrow F' = 3$ resonance. We also include a repump pulse (with the second MOT beams) to ensure all atoms atoms are in the $F = 2$ hyperfine ground state.

In addition to the data camera, we have two Sony video cameras (Supercircuits P/N SSC-M383), typically used in security applications, that monitor the pyramid MOT and the second MOT. These cameras are equipped with a 6× zoom lens [Edmund Optics NT52-274 (discontinued)], and we monitor the output on small LCD monitors. These cameras provide us an easy way to verify the MOT(s) are working, and play a critical role in overlapping the MOT and the dipole trap.

2.7.   Control and Timing Electronics

Our entire experiment is computer controlled (except for locking the lasers and overlapping the MOT and the dipole trap) using an open-source, home-built system, affectionately referred to as ZOINKS (Zee Open Interface Networked Kontrol System) [77]. This system was designed to eliminate the need for expensive proprietary software and hardware, providing a versatile and easy-to-construct system for controlling atom-optics experiments. The main idea is to connect one control computer to several micro-processors, which then communicate with interface boards that control multiple digital- and analog-output channels. These channels control the various pieces of equipment in our experiment, such as the CCD camera, shutters, AOMs, and magnetic coils. The desired timing and control sequence is set in a Perl script executed by the user at the control computer, using an extensive library of Perl modules and subroutines designed specifically for our experiment by Jeremy Thorn. The control computer sends this information via ethernet to the microprocessors, which then pass the information to the interface boards that precisely execute the sequence. The interface boards are synchronized to a 10 MHz atomic clock and provide timing accurate to 0.02 μs with a 4 μs resolution. This system has allowed us to control virtually all aspects of our experiment with precision timing, greatly simplifying various alignment procedures, troubleshooting, and data collection.

CHAPTER III

THE ONE-WAY BARRIER PART I: THE MECHANICS

Figure 3.7 was published in the coauthored work, Ref. [78].

3.1. Introduction

The field of atom optics has catapulted to the forefront of physics research as a result of its success at controlling and manipulating the motional states of atoms, and it continually strives to develop new and more broadly applicable methods. The "one-way barrier," or "atom diode" [78–90] is a welcome addition to its arsenal, as it can be implemented with a wide range of atomic and molecular species. Additionally, this new control tool has potential application in emerging cold-atom technologies such as atom chips [91, 92]. Proposed independently by Raizen *et al.* [79] and Ruschhaupt and Muga [80], the one-way barrier, composed of two laser beams, allows atoms traveling in one direction to pass through, but reflects atoms traveling in the other direction. In this chapter we will discuss the concept of the all-optical one-way barrier, its relation to Maxwell's Demon, and our experimental implementation of the barrier [78, 90].
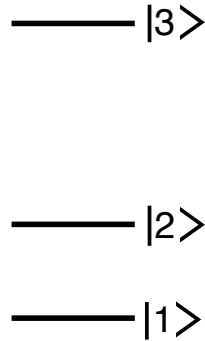
Figure 3.1. Energy level structure for the three-level atom with two ground states and one excited state used to introduce the concept of the one-way barrier.

3.2. How It Works

We will explain the concept of the one-way barrier in the context of the three-level atom shown in Figure 3.1, which has two ground states and one excited state, though it potentially has broad application to almost any level configuration given careful consideration of the atomic structure and laser frequencies. Several schemes for different two- and three-level systems have been outlined by the original authors [79, 80], and Thorn *et al.* [78] outlines a possible scheme for a four-level system.

The optical dipole potential, discussed in Section 1.6, embodies the main physics involved in the one-way barrier. In this phenomenon, the ac electric field of a non-resonant laser beam interacting with an atom shifts the atom's energy levels proportional to I/Δ. Here, I is the laser intensity and $\Delta = \omega - \omega_0$ is the laser detuning, defined as the difference between the laser frequency ω and the atom's resonance frequency ω_0. The intensity profile of the laser beam dictates the magnitude of the shift, while the sign of the detuning determines the direction of the shift, and

thus the nature of the resulting potential. For example, a focused, Gaussian laser beam with a negative detuning (red-detuned) presents an attractive potential to the atom, centered on the position of the focus, while a positively-detuned laser beam (blue-detuned) presents a repulsive potential (Section 1.6).

To create the one-way barrier for the three-level atom, we start by tuning the frequency of a laser beam part way between the two resonant frequencies for states $|1\rangle$ and $|2\rangle$ [Fig. 3.2(a)]. For this frequency, an atom that encounters the laser beam in state $|1\rangle$ will see an *attractive* potential and pass through, while an atom in state $|2\rangle$ will see a *repulsive* potential and reflect [Fig. 3.2(b)]. To make the barrier unidirectional, we add a second laser beam, positioned to the right of the first [Fig. 3.2(c)], that is resonant with the transition from state $|1\rangle \rightarrow |3\rangle$. We refer to the first beam as the main barrier beam and the second beam as the repumping barrier beam. In this configuration, we start the atoms in state $|1\rangle$ (the transmitting state), such that atoms impinging on the barrier from the left-hand side see an attractive potential and pass through unimpeded. After transmitting through the main barrier beam, the repumping barrier beam immediately optically pumps the atoms to state $|2\rangle$. Once in state $|2\rangle$ (the reflecting state), the main barrier beam presents a repulsive potential and the atoms reflect from it. Atoms starting on the right-hand side of the barrier get optically pumped to the reflecting state by the repumping barrier beam before encountering the main barrier beam, ensuring they reflect from it and remain on the right-hand side. The operation of the barrier is
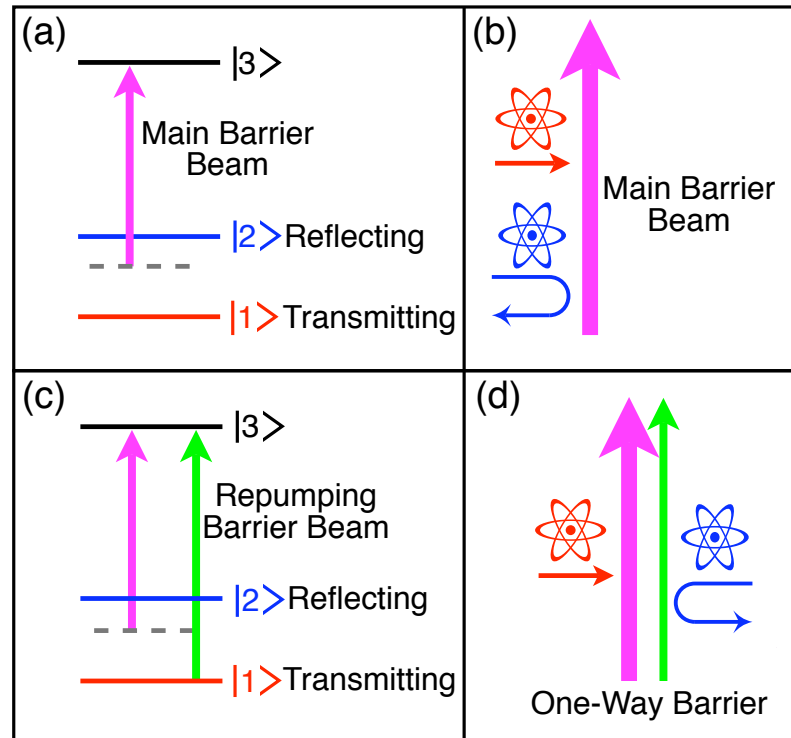
Figure 3.2. Schematic diagram illustrating different aspects of the one-way barrier. (a) The detuning of the main barrier beam relative to the transmitting and reflecting states. (b) Atoms in the red-detuned state (state $|1\rangle$) will pass through the barrier, while atoms in the blue-detuned state (state $|2\rangle$) will reflect from it. (c) The frequency of the main barrier beam and the repumping barrier beam for the three-level atom. (d) Atoms approaching the barrier from the left in the transmitting state will pass through, where the repumping barrier beam optically pumps them to the reflecting state.

illustrated schematically in Figure 3.2(d). In the remaining chapters, the left side of the barrier will always correspond to the transmitting side, while the right side will correspond to the reflecting side.

3.3. Maxwell's Demon

Beyond its potential as a tool for controlling the motion of atoms, the one-way barrier is intrinsically fascinating as a physical realization of Maxwell's demon [78, 85, 90]. In 1871, Maxwell pondered a paradox, positing a creature capable of making heat flow from cold to hot without performing any work, a violation of the second law of thermodynamics [93–95]. He imagined a container filled with gas particles, partitioned by a wall containing a trap door. A small creature operated this trap door, opening it to allow warmer particles to travel to the right-hand side of the container and cooler ones to travel to the left-hand side, but closing it to prevent them from passing back through. The creature, later referred to as Maxwell's demon, thus creates a flow of heat from cold to hot, generating a temperature differential where previously the system had been in equilibrium. Intuitively, we know this is only possible if energy (in the form of work) is supplied to create and sustain the temperature differential, such as the electricity used to run a refrigerator or an air conditioner. In the case of the demon and its trap door, there appears to be no energy supplied to the system to create and maintain the temperature gradient, thus creating the paradox of the demon's existence and its apparent violation of the second law of thermodynamics.

The heart of the conundrum lies with the second law of thermodynamics, which at its most fundamental level states that the entropy of the universe must increase or remain the same, and is tied to the concept of reversibility. Reversible processes

leave the overall entropy of the universe unchanged, so any increase in one system must be balanced by a decrease elsewhere, while irreversible processes increase the total entropy of the universe. Entropy provides a measure of the number of states accessible to that system, expressed as $S = k_\text{B} \ln g$, where k_B is the Boltzmann factor, and g is the number of accessible states. Changes in the entropy of that system are related to its temperature and any heat transfer between it and another system. When heat flows from a hot system to a cold system, the entropy increase of the cold system is greater than the corresponding decrease of the hot system, such that the net effect increases the total entropy of the universe, rendering the process irreversible. The demon and trap-door system conceived by Maxwell is problematic in that it does the *opposite*: separating the warm and cold atoms without performing work requires a *reduction* in the overall entropy of the universe, a violation of the second law of thermodynamics.

A variation of Maxwell's thought experiment involves the demon operating the trap door as a one-way barrier, opening it to allow gas particles to travel to the right-hand side, but closing it to prevent the particles from traveling to the left-hand side, thereby collecting all the particles on one side of the container (Fig. 3.3). Though this version does not involve temperature gradients, the entropic nature of the paradox remains the same. The system depicted in Figure 3.3 is isolated, such that no heat can be transfered to or from its surroundings, and any change it undergoes is described as adiabatic. Reversible, adiabatic processes occur at constant entropy ($\Delta S = 0$),
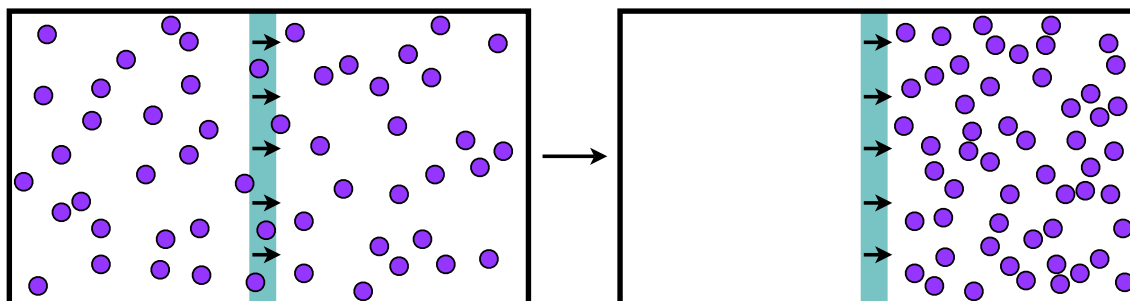
Figure 3.3. Illustration of the one-way barrier compressing the volume of a sample of gas, modified from an original created by J.J. Thorn.

since any change in entropy is intimately tied to the transfer of heat, which does not occur in an adiabatic process. During reversible, adiabatic compression (such as that performed by the demon), the reduction in volume is accompanied by a rise in the temperature, such that any decrease in entropy from the reduced volume is exactly balanced by the increase in entropy from the higher temperature. But herein lies the rub: studying the demon and trap door system, we see no increase in temperature—the speed of the particles has not increased—yet the volume has definitely been reduced. However, no work has been performed to carry out this reduction in volume either. There is no obvious increase in entropy elsewhere in the system to balance the decrease involved in compressing the volume. So the question remains: how do we reconcile Maxwell's demon and the second law of thermodynamics?

The answer to this question emerged over a century later, resulting from work on the thermodynamic implications of information storage and disposal in context of computing [94, 95]. Of particular importance is the concept that erasing stored information, such as the bits making up a computer's memory, is a thermodynamically

irreversible process that dumps entropy into the environment surrounding the device. The connection to Maxwell's demon lies within the fact that the demon must make a measurement on, and thus gain information about, each gas particle as it whizzes toward the trap door. If it has one bit of memory, after determining which side of the container the particle is on, its memory has two possible states—"on the left-hand side" or "on the right-hand side"—which yields an entropy of $k_{\mathrm{B}} \ln 2$. Before it can observe the next particle, its memory must be reset, which reduces the two possible states to one possible state—"the reset state"—which has zero entropy. To compensate for the reduction in entropy of the demon's memory, the corresponding amount of entropy must be dumped to the environment during the resetting process to guarantee compliance with the second law.

More realistically, assume the demon's memory has just enough storage space to retain position information about all N gas particles, and starts in the state where each bit is set to "on the left-hand side." This initial state has zero entropy since there is only one possible configuration of bits that produces this state. Assuming the particles have an equal probability of residing in the left-hand or right-hand side of the container, the demon's memory will be in one of the 2^N possible states after measuring all N particles, resulting in an entropy increase of $N k_{\mathrm{B}} \ln 2$. We calculate the corresponding entropy decrease experienced by the gas particles by considering the entropy difference between the 2^N possible ways to distribute N particles between the two sides of the container, and the one possible way to distribute the atoms when they

all reside in one side of the container. This calculation shows an entropy decrease of $Nk_\mathrm{B}\ln 2$, which is the exact amount by which the demon's memory increases, and the exact amount that would be dumped to the surrounding environment if the demon's memory is erased. Neither of these situations violate the second law of thermodynamics, so the demon and the laws of physics are able to coexist.

In reality, the experiment has several sources of heat and entropy that arise during the compression process, including photon recoil, unwanted scattering events, laser beam jitter, random spontaneous emission directions, and frequency changes in the scattered repumping-barrier-beam photons due to the switching process. Interestingly though, we can ignore all of these contributions except the last one, and entirely balance the entropy decrease of the atoms solely by examining the entropy increase of the repumping barrier beam due to frequency changes during the trapping process. The frequency changes arise from the slight energy difference between the transmitting and reflecting states, because every atom that becomes trapped by the barrier must absorb a repumping-barrier-beam photon that is resonant with the $|1\rangle \rightarrow |3\rangle$ transition, while the photon emitted back into the repumping barrier beam has a lower frequency, as it is resonant with the $|2\rangle \rightarrow |3\rangle$ transition. As a result, studying the frequency of the repumping-barrier-beam photons provides a record of the number of atoms trapped by the barrier, while each photon produced by the irreversible state change each atom undergoes during the switching process carries away the entropy necessary to balance any decrease experienced by the atom during the process.

Mathematical expressions for the change in entropy of the atoms and the repumping barrier beam during the trapping process have been derived in Thorn *et al.* [78], and in the large-atom-number approximation it has been shown that the entropy increase of the repumping barrier beam is at least as large as the corresponding decrease in the atoms' entropy, thus ensuring compliance with the second law of thermodynamics [78].

3.4. Implementation

We realize the all-optical one-way barrier with ^{87}Rb atoms using the D_2 transition (Fig. 2.4), which has hyperfine structure (Fig. 3.4) very similar to the three-level atom described above. In this case, the $F = 1$ and $F = 2$ hyperfine ground levels correspond to states $|1\rangle$ and $|2\rangle$ respectively, while the F' hyperfine manifold effectively corresponds to state $|3\rangle$ due to the small hyperfine shifts. We generate the main barrier beam by locking a third master laser to the largest spectral feature in the ^{85}Rb $F = 3 \rightarrow F'$ saturated-absorption spectrum, which conveniently lies in between the two ^{87}Rb hyperfine transitions (Fig. 3.5). Using the ^{85}Rb transition provides an opportune way for us to obtain a stable laser frequency with an appropriate detuning for each ground state because we already have its saturated-absorption spectrum due to the presence of both isotopes in our vapor cells. Stabilizing the main-barrier-beam laser to this transition (the $F = 3 \rightarrow F' = 3, 4$ crossover) yields a
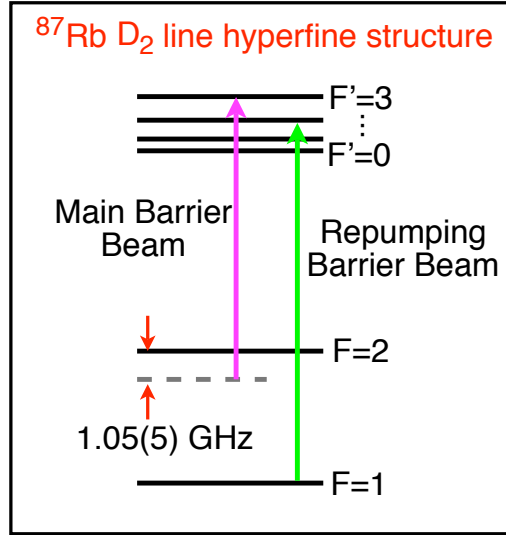
Figure 3.4. Hyperfine structure for the ^{87}Rb D$_2$ transition showing the relevant laser frequencies for the main barrier beam and the repumping barrier beam.

detuning 1.05(5) GHz blue of the ^{87}Rb MOT-trapping transition (Fig. 3.4). We lock the repumping barrier beam to the ^{87}Rb $F = 1 \to F' = 2$ repump transition.

Initially, we stabilized the main barrier beam to the ^{85}Rb $F = 2 \to F' = 2$ transition, which appeared to be an obvious choice since it lies nearly halfway in between the ^{87}Rb $F = 1$ and $F = 2$ hyperfine transitions (Fig. 3.5). This choice of detuning, however, created a poorly performing one-way barrier, because atoms in the $F = 1$ state still scattered a significant amount of main-barrier-beam photons during transmission. As a result, atoms traversing the barrier in the $F = 1$ state were frequently pumped to the $F = 2$ state, at which point the main barrier beam presented a very strong, repulsive potential, imparting a substantial amount of kinetic energy to the atoms. Unwanted heating during transmission, and thus the performance of the barrier, improved significantly by choosing a frequency further red-detuned from the
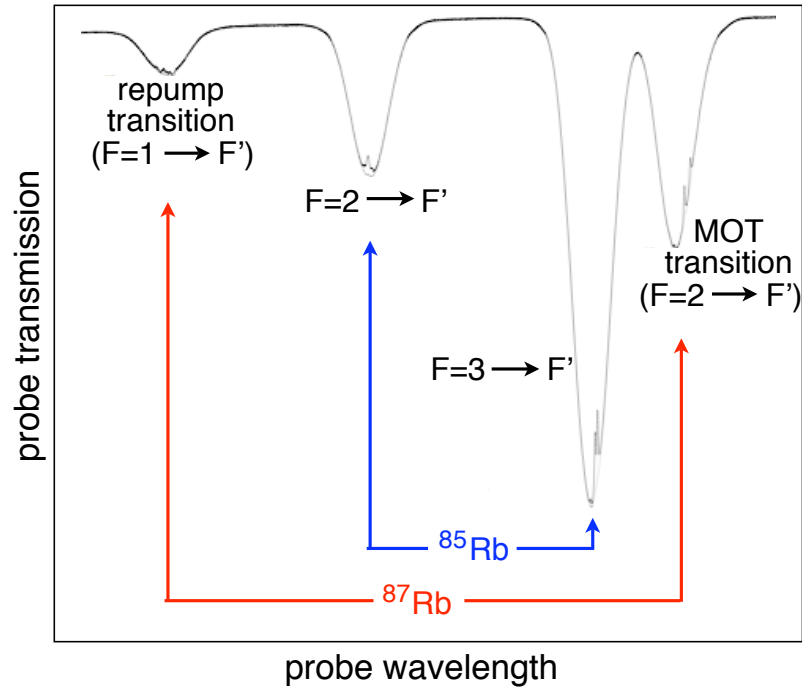
Figure 3.5. Saturated-absorption spectrum for the rubidium D_2 transition showing the relative frequencies for the ^{85}Rb and ^{87}Rb isotopes. This figure is modified from an original provided by D.A. Steck.

$F = 1$ ground state. Fortunately, the ^{85}Rb $F = 3 \rightarrow F' = 3, 4$ crossover transition proved to be an effective choice for the main-barrier-beam frequency, allowing us to avoid implementing a separate frequency stabilization scheme. We will discuss the topic of scattering and the main-barrier-beam frequency in more depth in Section 4.4.

In order to demonstrate the one-way barrier, we need to restrict the atoms to a region of space containing the barrier. We accomplish this by confining the atoms in the single-beam optical dipole trap described in Section 2.5, and intersecting its focus nearly perpendicularly with the barrier beams (Fig. 3.6). The 12(3)° angle between the barrier beams and the dipole trap's perpendicular allows optical access
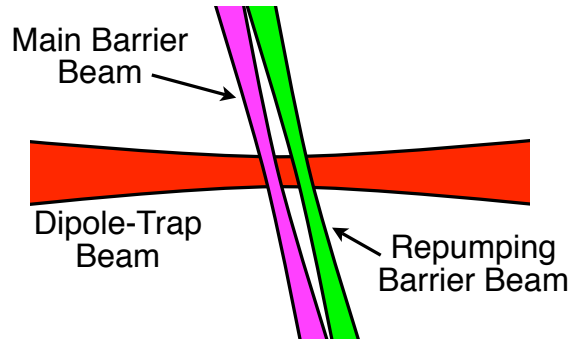
Figure 3.6. Schematic diagram illustrating the orientation of the barrier beams relative to the dipole-trap axis and focus. This figure was adapted from an original created by J. J. Thorn.
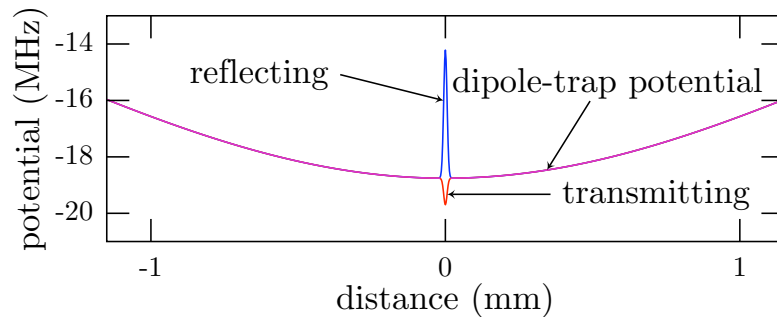
Figure 3.7. Optical potentials experienced by the atoms along the dipole-trap axis due to the dipole-trap beam and the main barrier beam. The wide, shallow potential results from the dipole-trap beam, while the narrow, attractive and repulsive potentials in the center result from the main barrier beam. The attractive (repulsive) potential corresponds to that seen by the atoms in the transmitting (reflecting) state. This figure was created by J. J. Thorn.

for the absorption imaging beam. Since the dipole trap tightly confines the atoms

in the radial direction, we have an effectively one-dimensional, nearly harmonic trap

divided by the one-way barrier. The optical potentials generated by the dipole-trap

beam and the main barrier beam are shown in Figure 3.7.

Several factors (beyond the detuning of the main barrier beam) play an important role in the barrier's performance, including the size, separation, and power of the barrier beams. The size requirements of the beams deserve careful consideration in that we need the beams to span the width of the dipole-trap beam at its focus, yet we also want them as narrow as possible along the dipole-trap axis (Fig. 3.6). It is important to have the beams as small as possible along the dipole-trap axis to decrease the time it takes for an atom to traverse them, which reduces unwanted scattering events that lead to heating and trap losses. The combination of the two size requirements led us to use elliptically-shaped barrier beams. The separation of the two barrier beams also requires some thought. Too much overlap leads to optical pumping of the atoms to the reflective state while still in the presence of the main barrier beam, while too much separation may prevent the atoms from switching to the reflecting state before turning around and heading back towards the barrier (since the atoms are attracted to the focus where the barrier is located). Initially, we set the separation such that the Gaussian tails of the barrier beams overlapped slightly, with the centers almost three beam waists apart. The main barrier beam does not require a significant amount of power because we focus it to a narrow waist and the potential barrier it forms only needs to be higher than the kinetic energy of the dipole-trapped atoms. The repumping barrier beam requires even less power since only a few scattering events are necessary to optically pump the atoms to the reflecting state (see Section 3.5 for these parameter values).

We oriented the linear polarization of the main barrier beam and repumping barrier beam parallel and perpendicular to the longitudinal axis of the dipole trap, respectively. We set the barrier-beam polarizations orthogonal to each other originally because we initially combined the beams with a polarizing beam splitter cube, but later switched to a standard beam splitting cube. We later changed the polarizations to match and observed its effect on the performance of the one-way barrier (see Section 4.6).

3.5. Optical Setup

As mentioned above, we used a third master laser, equipped with a saturated-absorption-spectroscopy setup, to generate the light for the main barrier beam. Since the power requirements of the main barrier beam are not very stringent, we coupled the remaining light not used in the saturated-absorption setup directly into a fiber for use in the experiment. We placed a home-built shutter, constructed from a speaker coil [96], and several neutral density filters in front of the fiber input that enabled us to turn the barrier beam on and off and control its power, respectively.

Obtaining the repumping-barrier-beam light was more complicated, as we derived the beam from the master laser that produces the repump light for the MOT setup. To accomplish this, we picked off the zero-order diffraction beam from the AOM in the repump setup and immediately fiber coupled it due to space constraints on the table. We still needed to shift the frequency to achieve resonance with the $F = 1 \rightarrow F' = 2$

repump transition, so we used the fiber to transport the beam to a more spacious location on the table, where we passed it through an 80 MHz AOM (Isomet P/N 1205C-1) and back into another fiber. Since the repumping barrier beam does not require a lot of power, losses from the AOM and multiple fiber couplings did not pose a problem. We also used the AOM to attenuate the intensity of the repumping barrier beam further. Using the repump-laser light for both the MOT and barrier setups works well because we typically do not operate the MOT and the barrier at the same time.

We constructed the optical setup for the barrier beams on a small, $6'' \times 12''$ optical breadboard mounted on $4''$ legs that had several advantages over using the main optical table. First, it allowed us to align and characterize the barrier beams elsewhere before inserting them near the Hellma cell, which limits our optical access. Second, it enabled us to use much shorter optical mounts, thereby improving stability, since the dipole-trap beam is located about $7.5''$ above the main optical table. Third, it played a crucial role in overlapping the dipole-trap focus with the foci of the barrier beams by allowing us to move the foci of the barrier beams without having to adjust the individual optics, but by simply moving the whole table. Despite these benefits, we encountered some drawbacks as well, which we will discuss shortly.

The optical layout of the small table is shown in Figure 3.8. We combine the beams on a $50 - 50$ beam splitter cube (Newport P/N 10BC17MB.2), then send them through a $6\times$ magnification anamorphic prism pair to increase the beam width
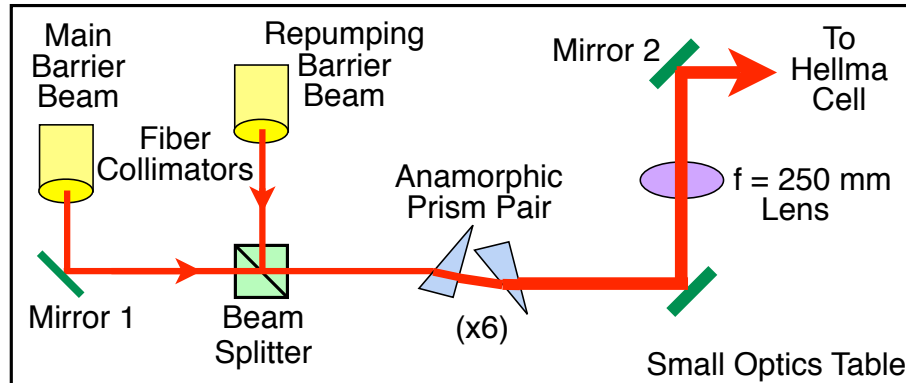
Figure 3.8. Optical layout for producing and controlling the geometry of the barrier beams, including the fiber output collimators, critical steering mirrors, beam splitter, anamorphic prism pair and lens.

in the horizontal direction. Next the beams pass through a 250 mm focal length lens and reflect from a mirror into the Hellma cell. The main barrier beam focuses to an 11.5(5) μm waist ($1/e^2$ intensity radius) along the dipole-trap axis and an 80(7) μm waist perpendicular to the dipole-trap axis. The repumping barrier beam focuses to 13(2) μm and 60(7) μm waists parallel and perpendicular to the dipole-trap axis, respectively. The depths of focus for the two beams are slightly different, which results from imperfect collimation by the fiber collimators, and also explains the slightly different beam waists (we actually positioned and glued the plugs of these collimators ourselves, resulting in small variations). The power of the main barrier beam (inside the Hellma cell) varies depending on the experiment, but it generally ranges from $24 - 40$ μW of power, while we typically ran the repumping barrier beam at about 0.35 μW of power (inside the cell).

3.6.   The Separation of the Barrier Beams

Controlling and measuring a tens-of-microns separation between two laser beams with about 12 μm waists proved technically challenging, requiring several modifications to develop a viable method.

Initially, the optical setup did not include mirror 1 (Fig. 3.8), and we attempted to control the relative height and separation of the two beams by securing the fiber collimators in the fiber-coupling fixtures (Section 2.3.7), which provided vertical and horizontal translation and tilt. Unfortunately, these mounts were not very stable, such that small bumps to the collimators or the fibers permanently altered the beam positions. Additionally, there was too much coupling between the different degrees freedom, so we had difficulty independently controlling the vertical alignment and the horizontal separation. We later secured the fiber collimators in stationary mounts and added mirror 1, which is our only means of controlling the beam separation and relative height.

Another challenge involved devising a method to accurately adjust the separation so we could set it close to a desired value, as we found it difficult to reproducibly turn the mirror mount knob (New Focus P/N 9773) a small, fixed amount. To remedy this, we glued an unusable scanning-tunneling-microscope tip (just the small needle) above the knob and colored every other groove (Fig. 3.9), with the red groove marking the ideal separation. This allows us to visibly track how many grooves and ridges we turn the knob each time, and to reliably set the separation to a reasonable value.
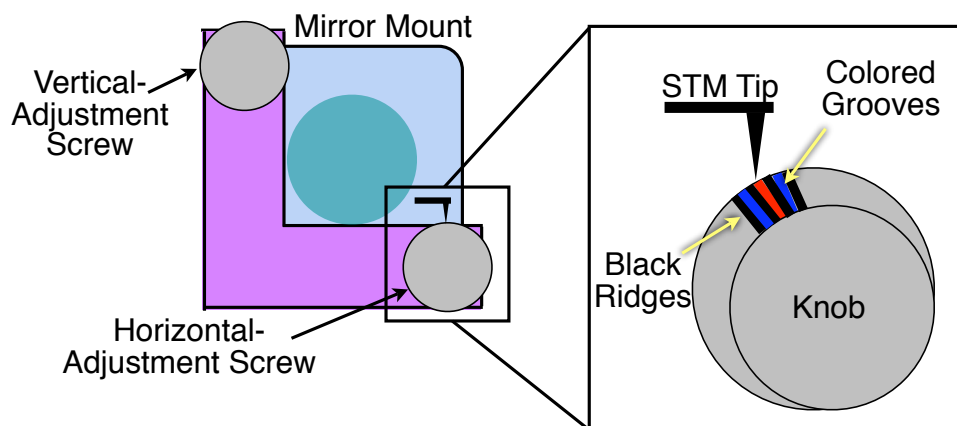
Figure 3.9. Illustration of the mirror mount knob used to control the barrier beam separation, modified to provide visual tracking of how far the knob is turned, including the mirror mount, knob, scanning-tunneling-microscope tip and colored grooves on the knob.

We determined that one groove-to-ridge turn (or vice versa) produces about a 4 μm change in the separation. Typically we operated the barrier with about a 34 μm separation.

Originally, we set and measured the separation with the small optical table removed from its position near the Hellma cell. To do this, we sent the beams into a power meter and used a razor blade attached to the air cart to find the center of each beam. While we were able to accurately measure the separation, moving the small optical table proved problematic. First, frequently moving the table was a hassle, and small bumps during the move sometimes shifted the separation and relative height of the two beams, leaving us unsure of the actual beam geometry during the experiment. Second, we noticed that simply bolting the legs of the table in place caused it to flex, significantly affecting the vertical alignment. This led us to develop a method for

measuring the beam separation without removing the small optical table from the experimental setup.

To accomplish this, we placed a mirror in the beam path and reflected the barrier beams into a beam profiler affixed to a three dimensional translation stage. The beam profiler consists of a web cam (Panasonic BL-C1, designed for people to observe their pets remotely) that we modified into a profiler by removing the lens and attaching neutral density filters. In the spirit of its originally intended use, we refer to it (as does Panasonic) as the "petcam." The CCD has a resolution of 5.6 μm/pixel, which is insufficient to accurately determine the location of each focus (and thus the separation), since the beam waists are on the same order of magnitude as the camera resolution. To circumvent this problem, we image each beam profile at several locations along the beam axis on both sides of the focus, then interpolate to determine its position.

Generally, we found that the relative height of the barrier beams is very sensitive and shifts quite a bit over short periods of time, on the order of a week or two. As a result, we regularly observed the beams on the petcam and visually adjusted for any vertical shifts using mirror 1. Figure 3.10 illustrates the extent of the vertical shifts we frequently observed. Since mirror 1 changes the vertical position of the main barrier beam, it inevitably necessitated realignment of the main barrier beam with the dipole-trap beam (Section 3.7). We also checked the horizontal separation after
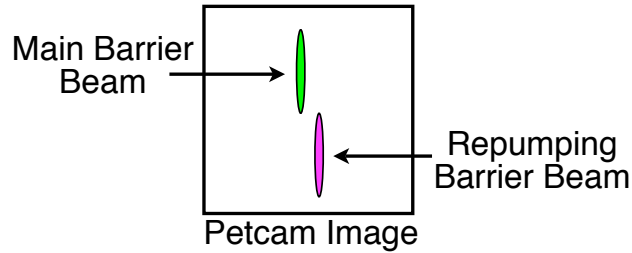
Figure 3.10. Depiction of the typical vertical shifts we observed on the petcam for the relative height of the main barrier beam and repumping barrier beam.

each vertical adjustment because there is a small amount of coupling between the mirror's vertical and horizontal degrees of freedom.

3.7. Alignment

One of the more challenging aspects of implementing the one-way barrier was devising techniques for accurately aligning the focus of the main barrier beam with the focus of the dipole-trap beam. To set the context, we needed to intersect the 30.9 μm waist of the dipole-trap beam with the 11.5×80 μm waist of the elliptical main barrier beam inside a vacuum cell where we have no physical access. In this section we will detail the method we finally settled on, though this discussion will not reflect the continuous refinement of our alignment techniques that led to this method, necessitated by our quest for a functioning one-way barrier.

We perform this alignment procedure with the repumping barrier beam blocked, and we assume the relative height and horizontal separation of the two barrier beams has already been set.
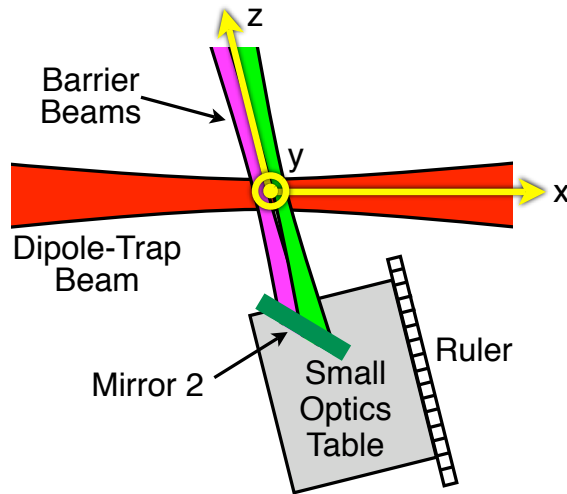
Figure 3.11. Schematic diagram showing the orientation of the x, y, and z alignment dimensions relative to the dipole-trap axis and barrier beams, including the small optics table, mirror 2, and the ruler used to measure the table's position in the z-direction.

Mirror 2 on the small optical table gives us vertical and horizontal control (the x- and y-dimensions in Figure 3.11) of the barrier beams, while sliding the small optical table closer or farther from the Hellma cell changes the z-position. We bolted a rail with a ruler on top next to the table's feet so that we could restrict the translation to the z-dimension and quantify the changes (Fig. 3.11). We generally avoided using the translation stages that control the dipole-trap-beam position to help with alignment because we wanted to preserve the dipole trap's alignment with the MOT and the dumping mirror, though we did use them to achieve finer adjustments in the z-position than the sliding-method's resolution afforded.

We achieve crude alignment of the main barrier beam by overlapping the MOT with the focus of the dipole-trap beam, and then aiming the main barrier beam where

it most greatly affects the MOT. We do this with the main barrier beam tuned (not locked, just floating) slightly blue of the MOT cycling transition, because at this detuning small beam powers can blow most of the MOT atoms away. We start with the small table in a z-position where the main-barrier-beam is out of focus with the MOT, because the larger beam size aids in the initial overlap of the MOT and the barrier beam. We steer the barrier beam with mirror 2 until we find the position where it most greatly affects the MOT. We then incrementally slide the small table to a z-position near where the main-barrier-beam focus and the MOT overlap, using mirror 2 to keep the beam aligned on the MOT in the x- and y-dimensions. We know we are close to the focus when the barrier pokes a small hole in the MOT.

Once we have the main barrier beam and the dipole trap beam in the same vicinity, we set about precisely adjusting the z-position by looking for the location where the dipole-trapped atoms best reflect off of the main barrier beam [Fig. 3.12(a)]. To accomplish this, we increase the power of the main barrier beam and lock it to the ^{87}Rb repump transition because it makes an excellent barrier for atoms in the $F = 2$ state due to the 6.8 GHz detuning. We then load the atoms away from the center of the dipole trap and observe how well they reflect off the barrier, then incrementally change the barrier's vertical position with mirror 2, looking for the position that has the best reflection. If we achieve 100% reflection for several vertical positions, we reduce the power and repeat the procedure. Next we move the z-position of the small table, and repeat, until we find the z-position that produces the best reflection with
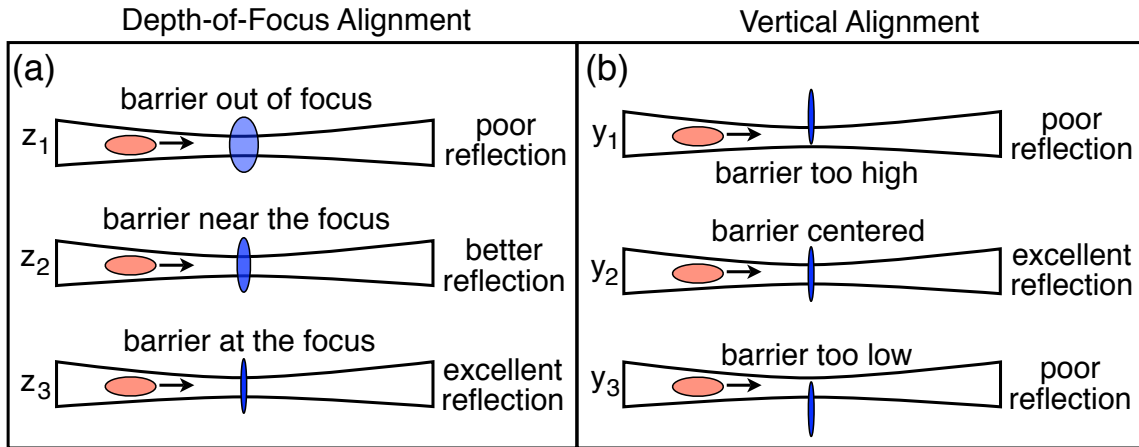
Figure 3.12. Illustration of the reflection-based alignment technique for overlapping the dipole-trap focus with the blue-detuned barrier-beam focus. (a) The depth of focus (z-direction) alignment concept, illustrating that an out of focus barrier beam creates a poorly reflecting barrier. (b) The vertical (y-direction) alignment concept, depicting how poor vertical alignment of the barrier beam diminishes how well the barrier reflects atoms.

the lowest power. In our last experiment (Chapter 5) we made finer adjustments to the z-position using the translation stages that control the dipole-trap position.

We align the vertical position of the barrier using the method outlined above, finding the y-position of the barrier where the atoms reflect best with the lowest power [Fig. 3.12(b)]. We set the position of the barrier along the dipole-trap axis (the x-position) similarly, except we load the trap full of atoms, and then observe the position where the main barrier beam pokes a hole in the nearly Gaussian atomic distribution (Fig. 3.13). We use mirror 2 to overlap the main barrier beam with the peak of the distribution.
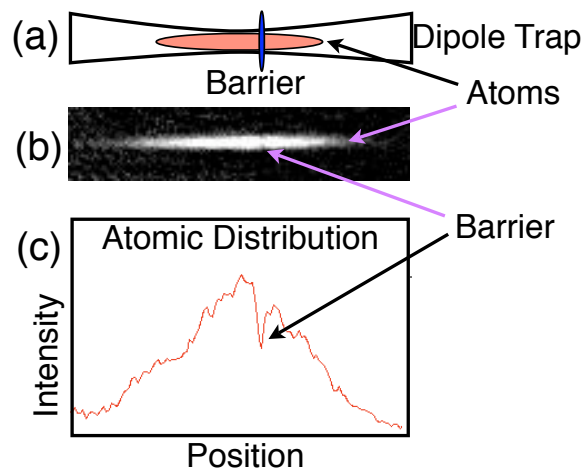
Figure 3.13. Images demonstrating the horizontal (x-direction) alignment concept for intersecting the blue-detuned barrier-beam focus with the dipole-trap focus. (a) Diagram showing the barrier beam misaligned horizontally from the dipole-trap focus. (b) An actual image the blue-detuned barrier beam poking a hole in the atoms confined in the dipole trap. (c) The atomic distribution for the average of several images [like those in (b)], showing the misalignment of the barrier with the dipole-trap focus.

CHAPTER IV

THE ONE-WAY BARRIER PART II: DEMONSTRATION AND

CHARACTERIZATION

Figures 4.5 and 4.7-4.15 were published in the coauthored works, Refs. [78, 90].

4.1. Introduction

Now that we have discussed the mechanics of creating and implementing an all-optical one-way barrier, in this chapter we will cover the experimental procedures used to demonstrate successful barrier operation, present our results, and study its robustness to variations in several of the experimental parameters [78, 90]. In particular, we will look at how changing the barrier-beam separation, effective barrier height, repumping-barrier-beam power and main-barrier-beam detuning impact the barrier's performance.

4.2. The Dipole Trap

As mentioned perviously, we confine the atoms in a single beam, far off-resonant, optical dipole trap (Section 3.4), which we focus to a 31.0(5) μm waist ($1/e^2$ intensity radius) and operate at a power of 9.3(5) W. This produces a nearly conservative, nearly harmonic trapping potential with axial and radial oscillation frequencies of

24 Hz (42 ms period) and 3.0 kHz, respectively. The 2 orders of magnitude difference between the axial and radial oscillation frequencies allows us to effectively treat the atomic motion as one-dimensional. For ^{87}Rb in either hyperfine ground state, these parameters yield a $k_{\mathrm{B}} \times 0.9$ mK trap depth and a maximum scattering rate of 3 s^{-1}.

We load the atoms into the dipole trap from our six-beam MOT, with the goal of loading as many atoms as we can at the lowest temperature easily achievable with our system. To this end, we start by creating a decent-sized, relatively cold MOT. We typically form the MOT near the center of the Hellma cell, though we figured out that moving the MOT higher places it near the center of the atomic beam coming from the pyramid MOT, significantly increasing its size. We accomplish this by shifting the zero-field position of the anti-Helmholtz coils by increasing the slave-coil current relative to the master-coil current. We use this trick to our advantage, shifting the MOT into the atomic beam to bolster its numbers prior to loading the dipole trap. Once gorged, we implement an additional cooling stage for the MOT before the loading process. We achieve additional cooling by reducing the intensity of the MOT trapping light by about 25% and red detuning its frequency further by another ~ 54 MHz, implementing a process called "polarization gradient cooling" [97, 98]. After the polarization-gradient-cooling stage, we have about 2×10^5 atoms (measured using fluorescence imaging) at a temperature of about 30 μK (measured using time-of-flight methods).
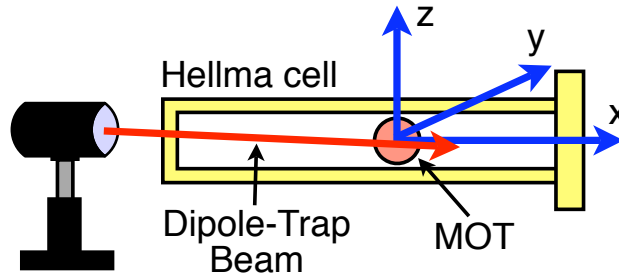
Figure 4.1. Diagram showing the orientation of the x-, y-, and z-dimensions relative to the dipole-trap-beam.

We use the magnetic bias fields produced by the Helmholtz coils to move the MOT in the y- and z-dimensions so that it overlaps with the dipole-trap beam for the loading process (Fig. 4.1). To accomplish this, we turn the dipole-trap beam on and off at 0.5 Hz, then use the computer to shift the MOT in the y-z plane until we find the location where the dipole-trap beam has the greatest effect on the MOT. Due to the large detuning of the dipole-trap beam, we often have to reduce the size of the MOT to more easily see the effect of the dipole-trap beam. We also had to check the overlap several times a day during our one-way-barrier experiments as a yet-to-be-discovered piece of dust on one of the six-beam MOT fiber outputs slowly shifted the position of the MOT.

The actual loading process involves turning on the MOT and dipole trap simultaneously for a period of time $(5 - 110 \text{ ms})$ while overlapping the MOT with the focus of the dipole trap. Once the MOT-trapping light and magnetic fields are switched off, the MOT atoms that did not load into the dipole trap rapidly disperse.

We use the magnetic bias field in the x-dimension to change the loading position of the MOT along the dipole-trap axis, which allows us to change the initial kinetic energy and ensuing dynamics of the atoms. For example, since the dipole trap creates a nearly harmonic potential, loading in the center generates a symmetric distribution with little collective motion (possibly a little "breathing"), while loading briefly ($\sim$ 5 ms) off to one side produces a small group of atoms that collectively oscillate about the center of the trap (Fig. 4.2). Loading off to the side for longer periods of time results in the atoms spreading out spatially to uniformly fill the trap, creating an atomic distribution that is difficult to distinguish from a center loaded distribution. Using the bias fields, we can vary the loading position along the dipole-trap axis by more than 1 mm to either side of the dipole-trap focus.

Initially, we located the axial (x-dimension) position of the dipole-trap focus relative to the position where the MOT forms by loading the atoms into the dipole trap and observing their collective motion. We moved the air cart to adjust the position of the focus until we found the location where the atoms exhibited almost no oscillatory motion (just breathing) after loading.

Studying Figure 4.2, we see that the actual oscillation period of the atoms is about 50 ms, which is longer than the 42 ms predicted from the trap parameters in the harmonic approximation. This discrepancy arises from the both the loading position of the atoms, which lies in the mildly anharmonic region of the trap, and angular momentum. In the case of the latter, atoms can acquire a significant amount
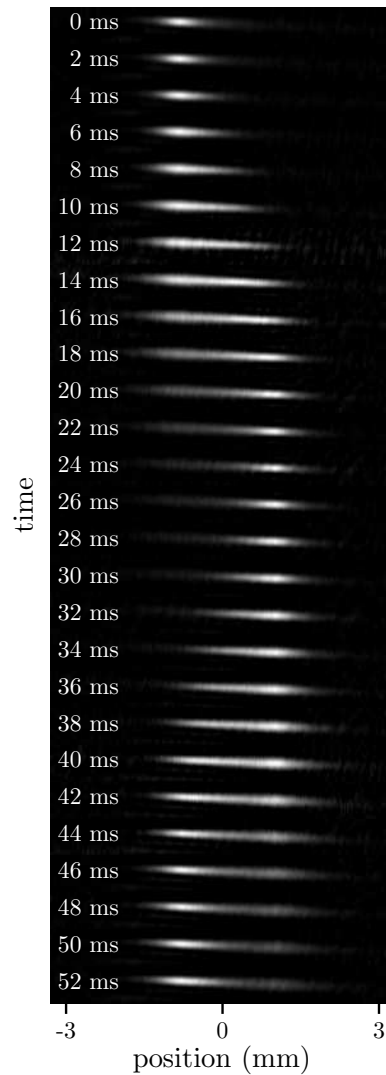
Figure 4.2. Image sequence showing the atomic cloud oscillating about the center of the dipole trap.

of angular momentum about the dipole-trap axis during the loading process, which detailed simulations reveal can reduce their axial velocity considerably [78]. Both of these factors contribute to the atomic cloud's loss of spatial coherence visible by the end of the oscillation period.

Loading the dipole trap full of atoms (110 ms load time) and taking a fluorescence image every second, we calculate a 20 s $1/e$ lifetime for the atoms in the dipole trap. The long lifetime affords us ample time to perform our experiments.

Once we have successfully loaded the atoms into the dipole trap, we control their initial hyperfine ground state via optical pumping. To create an ensemble entirely in the $F = 1$ ground state, we simply leave the MOT trapping light on for several milliseconds after loading the atoms into the dipole trap and turning off the repump light. Reversing the order in which we extinguish the beams produces an ensemble entirely in the $F = 2$ ground state. To verify that the optical pumping worked, we imaged atoms (supposedly) pumped to the $F = 2$ state with an absorption-imaging pulse that did not include a repump pulse. Typical optical pumping times range from $7 - 15$ ms.

4.3. Demonstrating the One-Way Barrier

The procedure for demonstrating the one-way barrier is as follows: First, we load the atoms into the dipole trap 0.95(5) mm to either side of the focus for 5 ms (Fig. 4.3), after which we have about 3×10^4 atoms in the dipole trap at about $\sim 100~\mu$K. Next, we optically pump the atoms into either ground state for 7 ms. We then let the atoms evolve in the trap for about half an oscillation period (~ 20 ms), after which the atomic ensemble is near its turning point on the opposite side of trap (Fig. 4.3). We inserted this extra half an oscillation period into the sequence
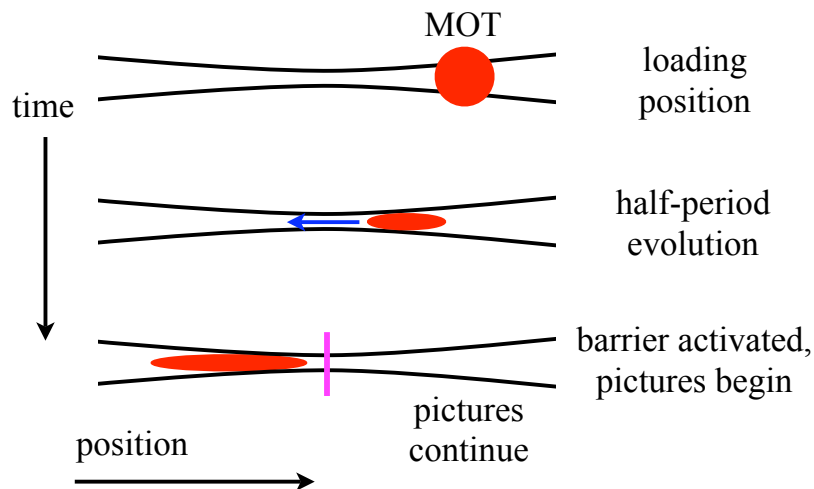
Figure 4.3. Illustration of the one-way barrier demonstration procedure showing the loading, evolution, and barrier activation sequence.

of events to prevent the dispersing, un-trapped MOT atoms from appearing in the first few images. The atoms spread out during this half-period delay, reducing their effective mean displacement from the trap center to 0.65(8) mm (averaged between the left- and right- start values), despite the initial displacement of 0.95(5) mm (Fig. 4.3). From this point forward, the initial loading position will refer to the displacement of the atomic cloud *after* this half-period delay, such that atoms starting on the left-hand side of the barrier were actually loaded on the right-hand side of the trap. After the half-period delay, we turn on the barrier beams (time $t = 0$ in Figure 4.5) and take an absorption image of the atoms using an $\sim$45 μs absorption imaging pulse. Since each image is destructive, we repeat this procedure, extending the time between turning the barrier on and taking the image from $0 - 100$ ms.
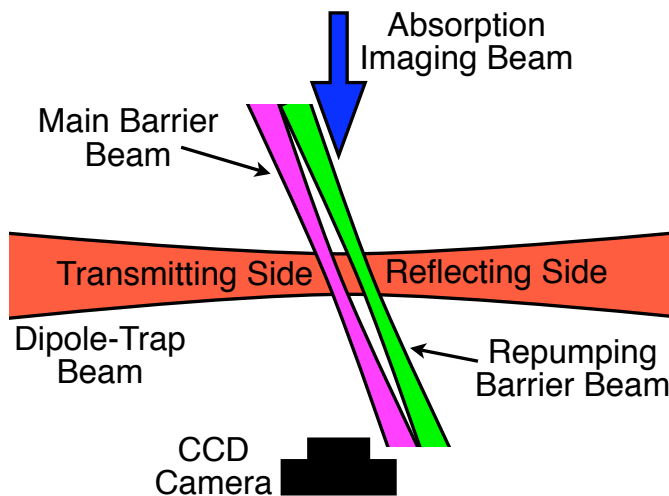
Figure 4.4. Schematic diagram showing the optical arrangement identifying the transmitting (left) and reflecting (right) sides of the one-way barrier, including the dipole-trap beam, barrier beams, CCD camera and absorption imaging beam. This figure is a modification of an original diagram created by D. A. Steck.

Figure 4.5 presents our main results for the one-way barrier, showing the dynamics of the atomic ensemble in response to the one-way barrier. The barrier is located at the origin of each column, with the main barrier beam positioned to the left of the repumping barrier beam (Fig. 4.4), identifying the transmitting side as the left-hand side of the barrier and reflecting side as the right-hand side. To elucidate the effects of the barrier, Figure 4.5(a) shows the atomic motion in the *absence* of the barrier, which simply exhibits the expected oscillatory behavior and loss of spatial coherence due to the trap anharmonicity and angular momentum.

The data presented in Figure 4.5(b) reveal the atomic evolution in the presence of the barrier. In this case, the atoms start from the left-hand side of the trap in the $F = 1$ transmitting state, such that we expect them to pass through the
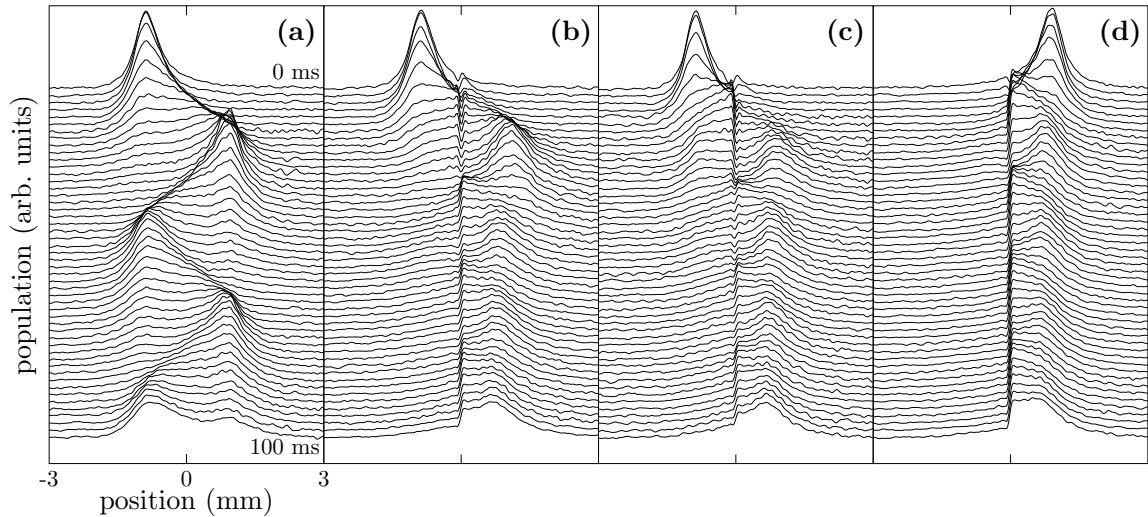
Figure 4.5. Atomic distributions in the dipole trap interacting with the barrier, which is located in the center of each column. Each image is an average of 78 repetitions of the experiment. Column (a) Atoms loaded on the left-hand side of the trap in the $F = 1$ transmitting state without the barrier. Column (b) Atoms loaded on the left-hand side of the trap in the $F = 1$ transmitting with the barrier present. Column (c) Atoms loaded on the left-hand side of the trap in the $F = 2$ reflecting state with the barrier present. Column (d) Atoms loaded on the right-hand side of the trap in the $F = 1$ transmitting state with the barrier present.

barrier and subsequently become trapped on the right-hand side. We observe the atoms transmitting through the barrier to the right-hand side as expected, turning around, and then reflecting from the barrier a couple times before reaching a steady state. However, we do not observe a significant number of atoms return to the left-hand side of the trap, as the barrier successfully obstructs their passage. Figure 4.6 shows the populations on both sides of the barrier as a function of time for the same initial conditions. Again, we see the population on the right-hand side of the barrier increase and then remain high as the atoms pass through barrier and become trapped on its right-hand side. The right- and left-side populations exhibit some oscillation,
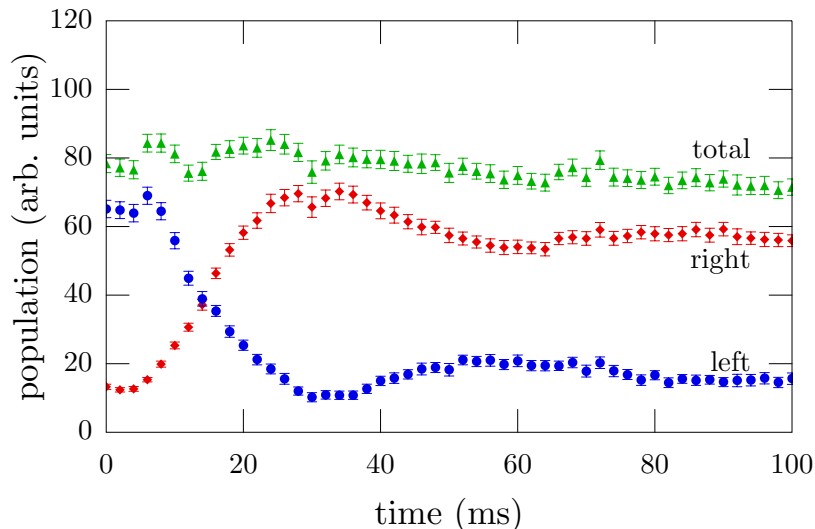
Figure 4.6. Populations on the left- and right-hand sides of the barrier as function of time for atoms initially in the $F = 1$ transmitting state starting on the left-hand side of the trap. The error bars indicate statistical error for 78 repetitions of the experiment.

however, indicating that some atoms manage to pass back through the barrier. The initial population on the right-hand side is not zero because a small portion of the atomic cloud extends into the right side of the trap when we turn the barrier on at $t = 0$.

Figure 4.5(c) shows the resulting dynamics when the atoms begin on the left-hand side of the trap but in the "wrong" initial state, the $F = 2$ reflecting state. Under these conditions, we expect the atoms to *reflect* from the barrier because it presents a repulsive potential regardless of the side of incidence. Interestingly though, we see that while the barrier reflects the atoms initially, they start to transmit to the right-hand side of the trap despite the barrier (the few atoms visible at $t = 0$ on the right-hand side of trap result from the atomic cloud extending beyond the dipole-

trap focus when the barrier is activated, rather than atoms transmitting through the barrier). As the evolution continues, the atoms proceed to slowly leak through the barrier, such that nearly all of them become confined to the right-hand side of the trap after 100 ms. We can explain this counterintuitive behavior by recalling that the main barrier beam is more nearly resonant with the $F = 2 \rightarrow F'$ transition than the $F = 1 \rightarrow F'$ transition (Section 3.4), resulting in an appreciable amount of scattering. Atoms in the $F = 2$ reflecting state that come into contact with the main barrier beam will initially reflect, however, the barrier will optically pump some of these atoms to the $F = 1$ transmitting state during the reflection. These atoms will then pass through the barrier unimpeded on their next interaction. The main barrier beam eventually optically pumps all the reflected atoms to the $F = 1$ transmitting state during subsequent reflections, allowing the atoms to accumulate on the right-hand side of the trap. This interesting phenomenon is a direct consequence of choosing the main-barrier-beam detuning to optimize transmission.

To verify the unidirectional performance of the barrier, Figure 4.5(d) shows the evolution for atoms initially in the $F = 1$ transmitting state starting on the *right-hand* side of the trap. In this instance, the barrier successfully reflects the atoms since they encounter the repumping barrier beam first, which optically pumps them to the $F = 2$ reflecting state, prior to reaching the main barrier beam. We achieve comparable reflections for atoms starting in the $F = 2$ reflecting state.

An interesting (and possibly versatile) feature of our one-way barrier is its ability to transmit atoms approaching from the left-hand side and reflect atoms impinging from the right-hand side *regardless* of the atomic state. This feature, which is a direct result of the 6.8 GHz ground-state hyperfine splitting for ^{87}Rb, potentially broadens its utility to applications with little or no state control. However, this particular benefit also comes at a cost, which manifests in the form of increased heating and trap losses.

4.4. Scattering

The most salient challenge in implementing the one-way barrier results from the excessive scattering of barrier photons due to the constraints placed on the main-barrier-beam detuning by the relatively small, 6.8 GHz ground-state hyperfine splitting of ^{87}Rb. These unwanted scattering events contribute directly to heating via hyperfine state changes and atom loss due to excited-state, collisional-loss mechanisms, beyond the heating expected from the recoil. These processes diminish trap lifetimes in the presence of the barrier, potentially jeopardizing its wide-spread applicability.

As mentioned in Section 3.4, tuning the main barrier beam about half way in between the $F = 1$ and $F = 2$ ground states proves to be a flawed (albeit obvious) choice, as its ability to optically pump a sizeable number of atoms to the $F = 2$ reflecting state during transmission remains high. An atom that undergoes such a

state change while traversing the main barrier beam experiences a sudden increase in potential energy, resulting in heating on the order of the barrier height. We observed substantial atom loss during transmission for this choice of detuning, prompting us to employ an asymmetric detuning much closer to the $F = 2 \to F'$ hyperfine transition. We investigate the barrier's performance for different main-barrier-beam detunings in Section 4.6.4.

Though the asymmetric detuning significantly reduces devastating state changes during transmission (as evidenced by our functioning barrier), we reasoned that it would compromise the barrier's performance during reflection for the same reason it improves transmission: The main-barrier-beam frequency is very close to the $F = 2 \to F'$ hyperfine resonance. Under these conditions, we believed the main barrier beam would optically pump reflecting atoms (in the $F = 2$ state) back to the $F = 1$ transmitting state, allowing them to leak through the barrier (indeed, this is the same reason our barrier eventually transmits atoms in *either* state, as discussed in Section 4.3). This state change (from $F = 2$ to $F = 1$), however, does not pose the same heating problem that the $F = 1$ to $F = 2$ state change causes, as the atom's potential energy is *lowered* during the process, reducing the overall energy of the atom.

To address the anticipated problem of a leaking barrier, we slightly overlapped the Gaussian tails (by about 3 $1/e^2$ intensity radii) of the main and repumping barrier beams. With this geometry, the tail of the repumping barrier beam rapidly pumps

any atoms that have been flipped to the $F = 1$ transmitting state during reflection *back* to the $F = 2$ reflecting state, before they have a chance to reach the main barrier beam again. Section 4.6.1 examines in detail how the separation affects the barrier's performance.

With careful selection of the main-barrier-beam detuning and separation, the one-way barrier functions as advertised. However, the overlap we employ between the barrier beams comes at the price of increased scattering. For example, simulations of the atoms interacting with the barrier that do *not* take into account the effect of the repumping barrier beam (state changes or scattering) reveal that an atom experiences ~ 0.7 and ~ 8 scattering events during a single transmission and reflection, respectively. We note that despite the significant detuning between the main barrier beam and the $F = 1$ ground state, scattering during transmission is not negligible. Including heating, state changes and scattering from the repumping barrrier beam as well as the spatial overlap in the simulations, the number of scattering events during a single transmission and reflection increases to ~ 3 and ~ 10, respectively [78, 90].

Though the increased number of scattering events may seem innocuous since many of them, as described earlier, actually *decrease* the energy of the atoms, a more insidious consequence of scattering in general comes from trap losses associated with light-assisted collisions. The moniker "light-assisted collisions" encompasses several kinds of excited-state, density-dependent collision processes in cold-atom traps, including fine-structure-changing collisions [99], hyperfine changing collisions [100],

photo-association [101], and radiative escape [98, 102], all of which result in atom losses. In particular, we believe the primary culprit responsible for our trap losses is radiative escape, since this mechanism becomes dominant at trap depths of ~ 1 mK. Here, an atom promoted to an excited state interacts much more strongly with its neighbors, rapidly accelerating towards them due to its increased polarizability. The strong interaction stops once the atom has returned to its ground state, but the kinetic energy gained by each atom during the process is often enough to eject one or both of them from the trap.

The lifetime for atoms trapped against the barrier speaks to the trap-loss issue. Figure 4.7(a) shows the population of atoms on both sides of the barrier, initially in the $F = 1$ state and loaded to fill the entire trap. At short time scales, the lifetimes vary from $300 - 500$ ms, depending on the temperature of the atoms. Lifetimes measured after about 200 ms, once the warmest atoms have left the trap, range from $700 - 900$ ms, with the data in Figure 4.7(a) yielding a lifetime of about 750 ms. Though these lifetimes are sufficient for our purposes, they stand in stark contrast to the 20 s lifetime of atoms in the dipole trap alone (no barrier), illustrating the magnitude of the losses produced by the excessive scattering of barrier photons during transmission and reflection.

To support the idea that light-assisted collisions play a role in the observed atom losses, we included a density-dependent loss mechanism in the simulations that model the data presented in Figure 4.7(a) [78]. The results of the simulations both with
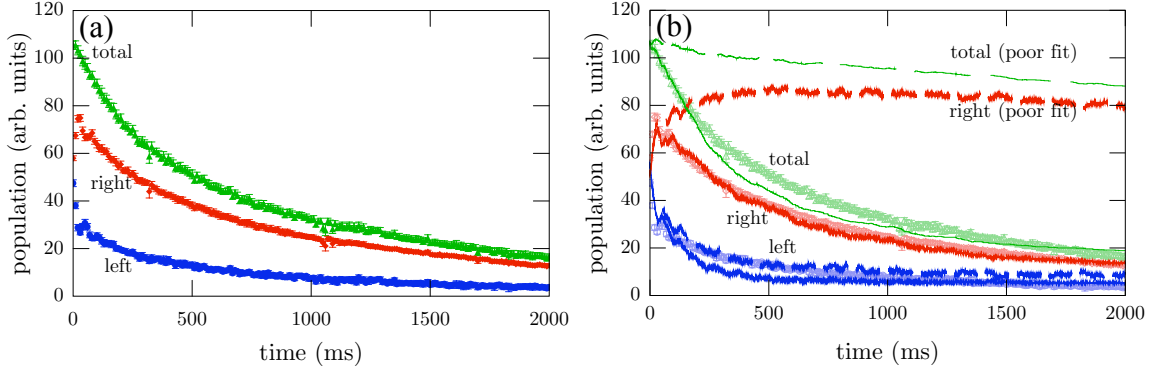
Figure 4.7. Measured and simulated populations on the left- and right-hand sides of the barrier up to 2 seconds after initially loading the trap full of atoms. (a) Data collected showing the lifetime of atoms trapped against the barrier. The error bars indicate statistical error for 18 repetitions of the experiment. (b) Comparison of simulations to the data shown in (a). The dashed curves show the results of simulations not including light-assisted collisions, while the solid curves show the results of simulations including light-assisted collisions. The simulation data were provided by J. J. Thorn.

and without the density-dependent loss mechanism are shown in Figure 4.7(b). The simulations that model the light-assisted collisions, which had one scaling term that was fit to the data, are in excellent agreement with the measured lifetime data. In contrast, simulations that do not model the light assisted collisions fit the data extremely poorly. This suggests that light-assisted collisions are the dominant loss mechanism for our one-way barrier.

Improving the performance of the barrier almost exclusively depends on increasing the detuning of the main barrier beam from the transmitting and reflecting states. One possible scheme for ^{87}Rb [103] makes use of the fine structure and exploits the $F = 1$ magnetic sublevels. In particular, it works out that at a wavelength of 792.5 nm, the optical dipole potential for the $m_F = +1$ state vanishes, while it

is positive for the $m_F = 0, -1$ states. Therefore, atoms starting in the $m_F = +1$ sublevel will transmit through the barrier as they experience no potential well or barrier, while atoms in the $m_F = -1$ sublevel will see a potential barrier blue-detuned by 2.5 nm from the 795 nm D_1 transition. Circularly polarized light resonant with the $F = 1 \rightarrow F' = 1$ D_2 hyperfine transition optically pumps atoms between the $m_F = \pm 1$ states. Another option for increasing the detuning of the main barrier beam involves implementing the one-way barrier with a different atomic or molecular species that has a more accommodating level structure. Thorn *et al.* [78] details a specific example using ^{88}Sr.

4.5.   A Maxwell's Demon

We devoted a portion of Chapter 3 (Section 3.3) to discussing the one-way barrier as a physical realization of Maxwell's demon, and indeed, our barrier is capable of compressing the phase-space occupied by a sample of atoms. Figure 4.8 shows the population of atoms on both sides of the barrier after loading the dipole trap off center for 110 ms, then waiting 200 ms before activating the barrier. The longer load time fills the trap symmetrically and nearly uniformly with about 9×10^4 atoms. Waiting 200 ms for the atoms to settle washes out most of the residual collective motion gained during the loading process. We lowered the main-barrier-beam power to 18(2) μW to reduce heating from scattering, since the atoms approach the barrier with less kinetic energy than in the barrier-demonstration experiments described previously.
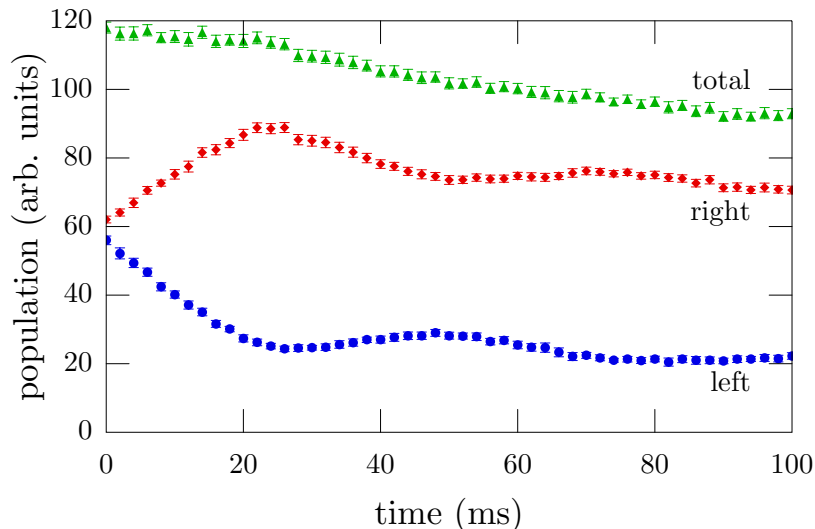
Figure 4.8. Populations on the left- and right-hand sides of the barrier as a function of time for atoms initially in the $F = 1$ transmitting state, loaded to fill the entire trap. The error bars indicate statistical error for 38 repetitions of the experiment.

After activating the barrier, the population on the left-hand side of the trap begins to decrease as the atoms pass through the one-way barrier and accumulate on the right-hand side of the trap. Though not all the atoms become trapped, the one-way barrier is clearly compressing the volume occupied by the atoms in a manner similar to Maxwell's demon. The spatial compression results in a 7(2)% decrease in phase-space volume, which is smaller than might be expected because heating from scattered barrier photons counteracts a substantial amount of the compression. Optimizing the barrier parameters for compression would likely improve the reduction in phase-space volume. Currently, however, the parameters optimize the barrier for transmission (Section 3.4, 3.5, 3.6).

4.6.   The Robustness of the Barrier

To characterize the one-way barrier, we evaluated its performance while varying four key experimental parameters:

1. the separation between the main barrier beam and the repumping barrier beam, from $8 - 74$ μm;

2. the initial loading position of the atoms along the dipole-trap axis from $0 - 0.9$ mm on both sides of the focus, which represents an effective change in barrier height;

3. the power of the repumping barrier beam, from $0.002 - 8.7$ μW; and

4. the detuning of the main barrier beam from the ^{87}Rb $F = 2 \rightarrow F' = 3$ MOT trapping transition, blue detuned by $+0.75$ GHz and $+4$ GHz from the $F = 2$ hyperfine ground state.

When assessing the barrier's performance, we are looking for ideal unidirectional behavior: namely, all the atoms should reside on the right-hand (reflecting) side of the barrier after 100 ms of evolution.

In addition to the parameters listed above, we rotated the polarization of the main barrier beam to match that of the repumping barrier beam, such that both beams were linearly polarized perpendicular to the dipole-trap axis. This had no obvious

effect on the barrier's performance, implying that main barrier beam's polarization is not crucial to the functionality of the barrier.

Throughout the remainder of this chapter, we will frequently refer to the particular parameter values we utilized during the barrier-demonstration experiments that produced the data presented in Figure 4.5. Those parameter values produce a nearly optimum-performing barrier, providing an excellent basis for comparing the effects of altering these parameters on the barrier's performance. We will collectively refer to these parameter values as the "standard values," corresponding to a 34(1) μm separation, a 0.65(8) mm loading position, a 0.36(4) μW repumping-barrier-beam power and a 1.05(5) GHz detuning from the MOT cycling transition.

4.6.1. The Separation

As discussed in Section 4.4, we expect the separation between the main and repumping barrier beams to play a significant role in the performance of the barrier. In particular, we reason that too little separation will allow the repumping barrier beam to pump atoms to the reflecting state before they successfully cross the barrier, while too much separation will prevent atoms which undergo a state change during reflection from reaching the repumping barrier beam to correct the state change, causing atoms to leak back through the barrier. Figure 4.9, which shows the populations as a function of beam separation on the left- and right-hand sides of the barrier after 100 ms of evolution, gives insight into the validity of this reasoning.

Figure 4.9. Populations on the left- and right-hand sides of the barrier as a function of barrier-beam separation after 100 ms. (a) Atoms starting in the $F = 1$ transmitting state on the left-hand side of the trap. (b) Atoms starting in the $F = 2$ reflecting state on the left-hand side of the trap. (c) Atoms staring in the $F = 1$ transmitting state on the right-hand side of the trap. (d) Atoms starting in the $F = 2$ reflecting state on the right-hand side of the trap. The error bars indicate statistical error for at least 20 repetitions of the experiment.

Figures 4.9(a) and 4.9(b) show the effect of the separation on the barrier's performance for atoms starting on the left-hand side of the trap in the $F = 1$ and $F = 2$ states, respectively. For separations below about 25 μm, the barrier's ability to transmit atoms becomes severely impaired, evidenced by the majority of atoms that remain on left-hand side of the barrier after 100 ms. This result confirms our reasoning that at small separations, the Gaussian tail of the repumping barrier beam extends far enough on the transmitting side of the barrier to optically pump atoms to the

reflecting state on *either* side of the barrier. This undermines the barrier's asymmetry, causing it to reflect atoms incident from either direction. Surprisingly though, the barrier's performance at large separations does not suffer significantly. The barrier successfully transmits atoms to the right-hand side of the trap at separations above 30 μm, however, the effectiveness of the barrier does decline slightly beyond about 50 μm. We attribute the decline to the reasoning that at smaller separations, most atoms will pass back through the repumping barrier beam after reflection, ensuring that any atoms pumped to the transmitting state while interacting with main barrier beam return to the reflecting state. At larger separations, however, some atoms may not reach the repumping barrier beam to correct for any state changes that occurred during reflection. This enables them to pass back through the barrier, reducing the population on the right-hand side of the trap. This effect is not as pronounced as we had anticipated, though, indicating that while overlapping the beams is necessary to optimize reflection from the barrier, it is not critical to barrier operation.

Section 4.4 explored the main drawback of employing some spatial overlap between the main and repumping barrier beams, highlighting the concomitant trap losses. Interestingly, this phenomenon is manifest in the data presented in Figures 4.9(a) and 4.9(b). Examining the total population data for both plots reveals a marked decrease in the total normalized population (the population at $t = 100$ ms compared to the population at $t = 0$) for separations that have non-negligible overlap (about 3 $1/e^2$ radii, or 40 μm apart). We believe the increased losses reflect the additional

scattering of photons due to the stronger repumping-barrier-beam component in the region of the main barrier beam. This produces more state changes, as the beams are more likely to optically pump the atoms between the two hyperfine ground-states during transmission. The stronger repumping-barrier-beam component also increases heating from scattering, since the atoms are more likely to change state in the middle of the barrier beam (as opposed to the side), where the potential energy increase associated with switching to the $F = 2$ reflecting state is substantial.

Figures 4.9(c) and 4.9(d) show how the separation impacts the reflectivity of the barrier for atoms starting on the right-hand side of the trap in the $F = 1$ and $F = 2$ states, respectively. Unlike the transmitting ability of the barrier, its reflectivity is quite robust to the beam separation, showing no dramatic changes throughout the range of separations. The effectiveness of the barrier decreases mildly above about 50 μm, exhibiting the same phenomena observed for larger separations (above 50 μm) in the left-hand-side results discussed earlier. These data suggest that as long as the repumping barrier beam is present to the right of the main barrier beam, the barrier's ability to reflect atoms remains largely intact.

4.6.2. The Loading Position

We also examined how loading the atoms at different positions along the dipole-trap axis affects the performance of the barrier. Altering the loading position of the atoms relative to the trap center changes the kinetic energy of the atoms, which we use as substitute for varying the height of the potential barrier. Though we can adjust
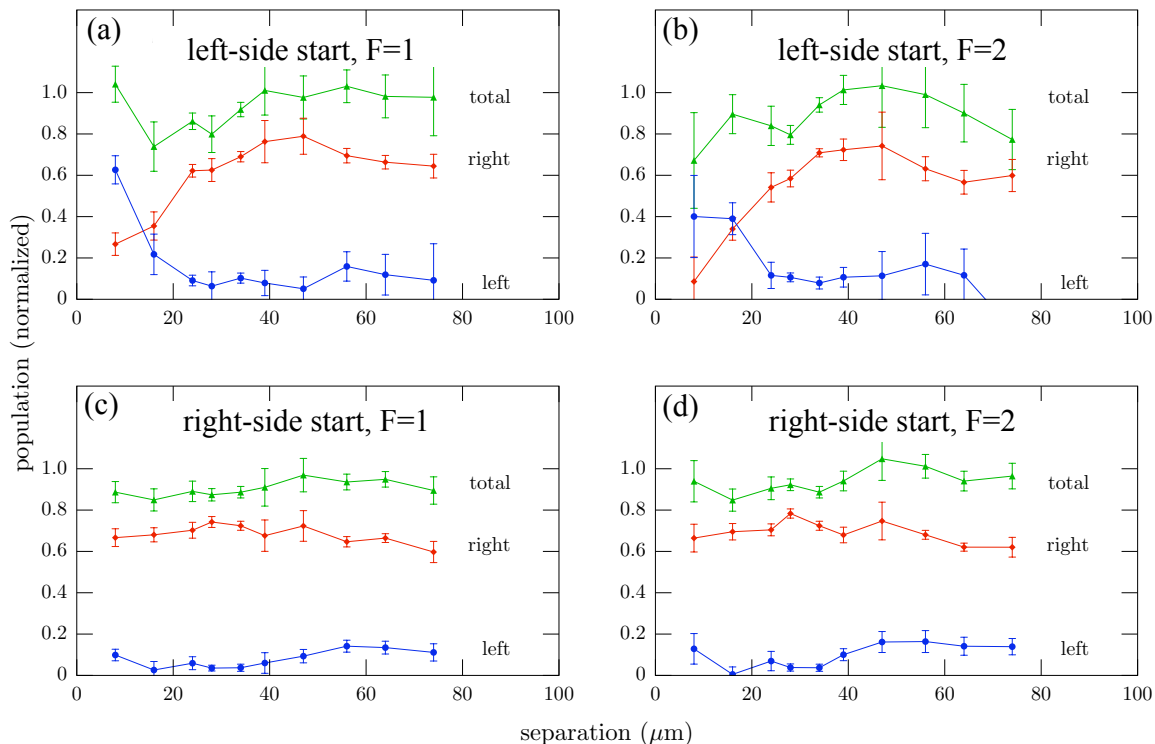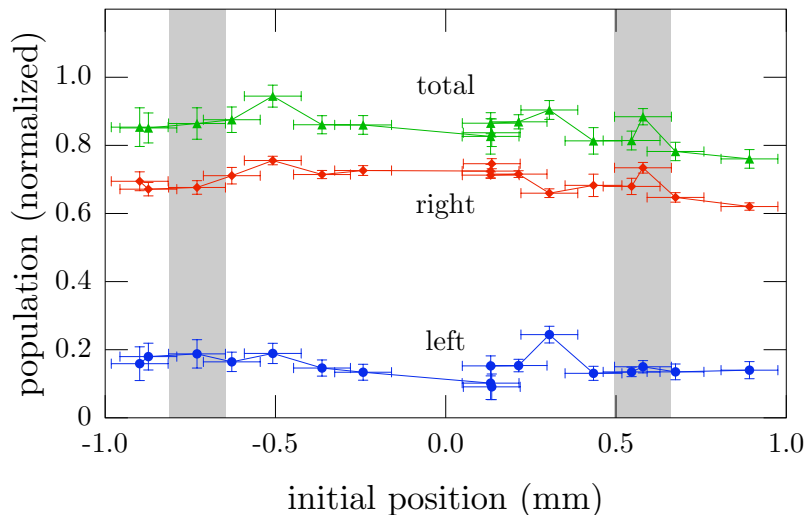
Figure 4.10. Populations on the left- and right-hand sides of the barrier as a function of loading position after 100 ms for atoms started in the $F = 1$ state. Negative (positive) loading positions indicate atoms starting on the left-hand (right-hand) side of the trap. The vertical, gray bars delineate the standard value for the starting position. The vertical error bars indicate statistical error for 38 repetitions of the experiment, and the horizontal error bars reflect the uncertainty in measuring the center of the MOT to determine the displacement.

the ratio of atomic kinetic energy to barrier height by changing either the loading position or the power of the main barrier beam, each change has a different effect on the number of scattering events expected as the atoms traverse the barrier. Appendix B in Thorn *et al.* [78] examines this topic in detail.

Figure 4.10 presents the populations on the left- and right-hand sides of the barrier (for atoms starting in the $F = 1$ state) as a function of loading position after 100 ms of evolution. The initial loading position is given by the difference between the center of the atomic cloud after the half-period delay (Section 4.3) and the focus of the dipole trap (position zero), measured in millimeters. This is defined such that negative loading positions start atoms on the left-hand side of the barrier and

positive ones start atoms on the right-hand side. The vertical, gray bars indicate the standard value for the starting position, which had an initial displacement of about $\pm 0.65(8)$ mm (averaged between the left- and right- start values). We see that the populations on either side of the barrier remain constant regardless of the loading position, indicating that the barrier functions equally well for a wide range of atomic velocities. Figure 4.11 shows a sample of the type of data aggregated to create Figure 4.10, which monitors the populations on both sides of the barrier as function of time for various initial loading positions. The atoms in data sets (a), (b), and (c) start on the right-hand side of the barrier and proceed to remain there, while the atoms in data sets (d) and (e) start on the left-hand side, then successfully transmit through the barrier where they remain trapped. Little distinguishes the five data sets after about 30 ms, reinforcing the conclusion that the barrier operates effectively regardless of the atomic kinetic energy.

4.6.3. The Repumping-Barrier-Beam Power

The repumping barrier beam plays a crucial role in the functioning of the one-way barrier in that it is responsible for the desired unidirectional behavior. Without it, the barrier would exclusively transmit or reflect atoms depending on their initial state, barring any optical pumping due to the main barrier beam. We varied the power of the repumping barrier beam by more than three orders of magnitude to assess its effect on the performance of the barrier. Figure 4.12 presents our results, showing the populations on both sides of the barrier after 100 ms as a function of repumping-
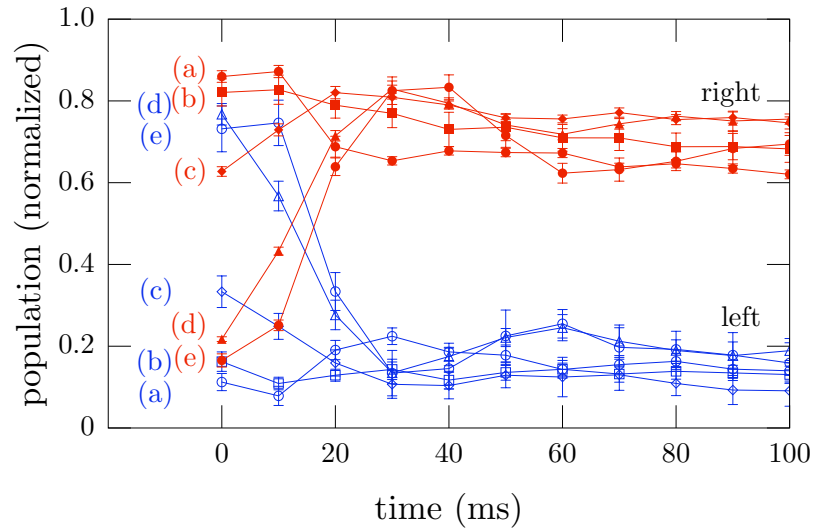
Figure 4.11. Populations on the left- and right-hand sides of the barrier as a function of time for several different loading positions for atoms started in the $F = 1$ state. The initial displacement for the five different data runs are (a) 0.89(8) mm, (b) 0.43(8) mm, (c) 0.14(8) mm, (d) $-0.51(8)$ mm and (e) $-0.90(8)$ mm. The error bars indicate statistical error for 38 repetitions of the experiment.

barrier-beam power for atoms starting on the left- [Fig. 4.12(a)] and right-hand [Fig. 4.12(b)] sides of the trap. For comparison, the vertical lines indicate the standard repumping-barrier-beam power, while the horizontal bars show the populations after 100 ms for data collected with no barrier. In this case, the collective motion of the atoms produces the unequal populations visible on each side of the barrier [see Figure 4.13(a) and 4.13(b)]. Overall, the functionality of the one-way barrier remains intact over the wide range of repumping-barrier-beam intensities we studied, though the minimum and maximum intensity extremes substantially impact its efficiency.

Figure 4.12(a) reveals that the barrier retains at least some ability to transmit and subsequently reflect atoms over the broad range of repumping-barrier-beam powers,
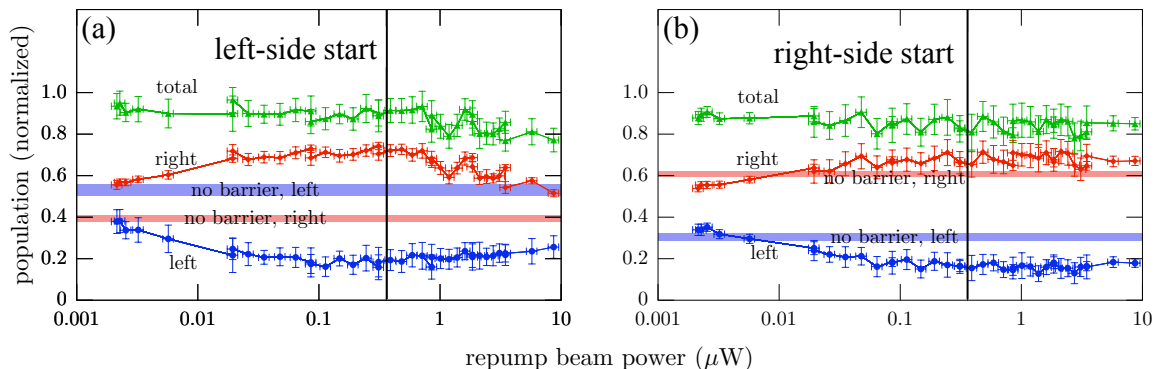
Figure 4.12. Populations on the left- and right-hand sides of the barrier as a function of repumping-barrier-beam power after 100 ms. (a) Atoms starting in the $F = 1$ transmitting state on the left-hand side of the trap. (b) Atoms starting in $F = 1$ transmitting state on the right-hand side of the trap. The vertical line marks the 0.36 μW standard value for the repumping-barrier-beam power. The horizontal bars show the populations after 100 ms for data collected with no barrier. The error bars indicate statistical error for at least 38 repetitions of the experiment.

evidenced by a majority of atoms collecting on the right-hand side of the barrier regardless of the power. A weak optimum also exists in the left-hand-side data, indicating that the barrier's unidirectional behavior starts to break down at very low and very high intensities. We expect the barrier to lose its asymmetry at very low repumping-barrier-beam intensities, since the repumping barrier beam becomes too weak to efficiently pump atoms to the reflecting state after they transmit through the barrier, allowing them to pass back through. In this limit, the collective motion of the atoms determines the populations on each side of the barrier, eventually reaching a steady state of 50%. Though we do not reach this limit in our experiment, we still observe that the barrier's unidirectional performance diminishes at low intensities. Despite this reduction in efficiency, a small amount of asymmetry persists in the

populations in Figure 4.12(a) at the minimum power, demonstrating that the barrier remains weakly functional even at extremely small repumping-barrier-beam intensities. At very high intensities, the Gaussian tails of the repumping barrier beam, which extend to the left side of the main barrier beam, contain a significant amount of power. This enables the repumping barrier beam to optically pump atoms to the reflecting state prior to encountering the main barrier beam, such that the atoms reflect off the barrier and remain trapped on the left-hand side. Though the data presented in Figure 4.12(a) do not approach this limit as some asymmetry remains visible, we observe the expected downward trend in the right-hand-side populations at higher powers.

The data presented in Figure 4.12(b) show how the intensity of the repumping barrier beam affects the reflectivity of the barrier. The population on the right-hand side of the barrier exhibits a notable decrease at smaller intensities, which is another manifestation of the low-intensity behavior described previously for the left-hand-side results. In this case, the repumping barrier beam lacks the intensity to successfully pump atoms to the reflecting state, such that the barrier ceases to reflect atoms effectively. In contrast to the left-hand-side results, however, the barrier's reflectivity improves and then saturates at higher repumping-barrier-beam intensities, suffering no decrease in efficiency. The small number of atoms observed on the left-hand side of the trap even at the highest intensities result from the atomic cloud extending to the left of the trap center when the barrier is turned on. The lack of dependence of

the barrier's performance on the increasing intensity of the repumping barrier beam reflects the fact that any intensity increase—beyond that necessary to optically pump all the atoms to the reflecting state—has no impact on the barrier's reflectivity. In fact, the repumping barrier beam *itself* becomes a formidable, low scattering barrier at high enough intensities, as it is blue detuned by 6.8 GHz from the $F = 2$ reflecting state of the trapped atoms.

To highlight the influence that the repumping-barrier-beam intensity has on the atomic dynamics, Figure 4.13 shows populations on both sides of the barrier as a function of time for the lowest and highest intensities starting on the left- [Fig.4.13(c)] and right-hand [Fig.4.13(d)] sides of the barrier. For comparison, the time series for the standard value of the repumping-barrier-beam intensity and the data collected with no barrier [Figs. 4.13(a) and 4.13(b)] are included as well. In Figure 4.13(c), we see that the minimum- and maximum-intensity data exhibit some oscillation of the population back and forth across the barrier, though the two curves never cross after the initial transmission through the barrier at $t \sim 13$ ms (unlike the no-barrier data, which crosses several times), demonstrating that the barrier retains some asymmetry even at the highest and lowest intensities. For the atoms starting on the right-hand side of the trap [Fig. 4.13(d)], only the minimum-intensity data display population oscillations, almost crossing at $t \sim 19$ ms, illustrating how the intensity of the repumping barrier beam compromises the barrier's performance at very small intensities while preserving its reflectivity at high intensities.
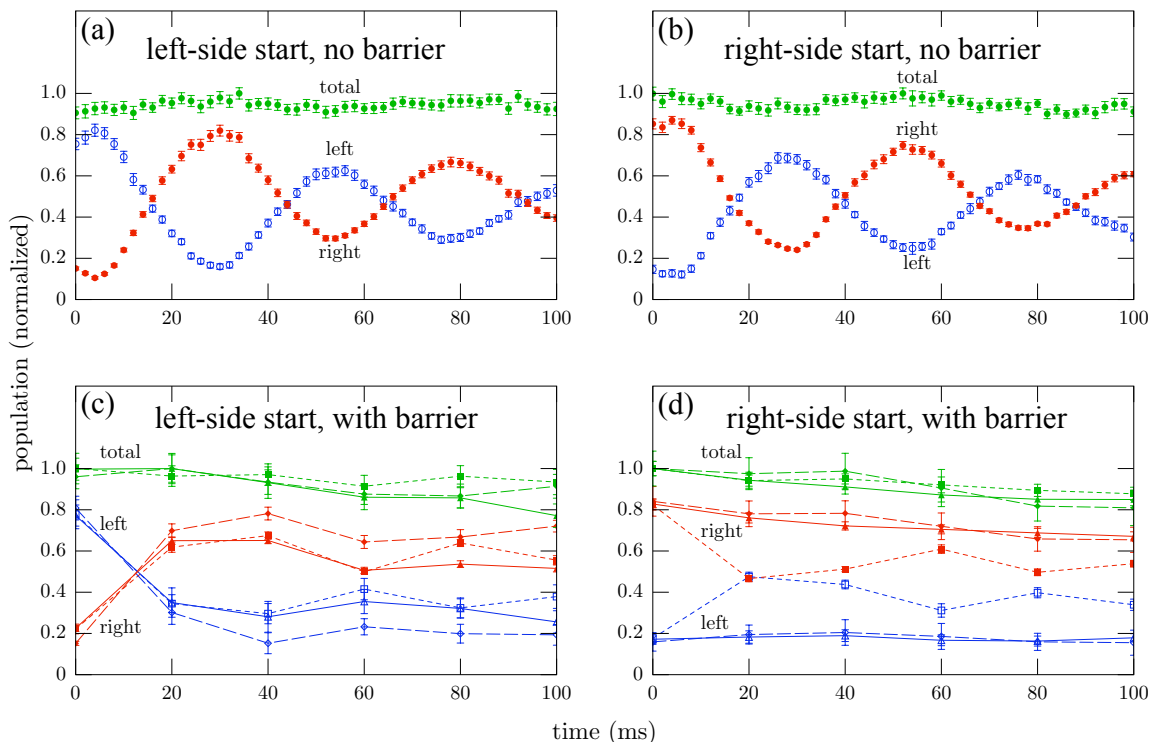
Figure 4.13. Populations on the left- and right-hand sides of the barrier as a function of time for: (a) Atoms starting in the $F = 1$ state on the left-hand side of the trap without the barrier. (b) Atoms starting in the $F = 1$ state on the right-hand side of the trap without the barrier. (c) Atoms starting in the $F = 1$ state on the left-hand side of the trap for the minimum (about 2 nW, dotted lines), maximum (about 9 μW, solid lines), and standard (0.36 μW, dashed lines) repumping-barrier-beam powers. (d) Atoms starting in the $F = 1$ state on the right-hand side of the trap for the minimum (dotted lines), maximum (solid lines), and standard (dashed lines) repumping-barrier-beam powers.

4.6.4. The Main-Barrier-Beam Detuning

Selecting an appropriate detuning for the main barrier beam that optimizes barrier performance while minimizing unnecessary scattering events was the main technical challenge associated with implementing the one-way barrier. In particular, choosing a detuning that minimized atom loss during transmission (Section 4.4) resulted in the standard 1.05(5) GHz detuning we employed for the barrier demonstration exper-

iments. Here we investigate how different choices of main-barrier-beam detuning affect losses for atoms starting on the right-hand (reflecting) side of the barrier.

We present data for three different, blue-detuned main-barrier-beam frequencies, each measured relative to the ^{87}Rb $F = 2 \rightarrow F' = 3$ MOT trapping transition: (1) The standard value of 1.05(5) GHz we utilized for the demonstration experiments, generated by locking the main barrier beam to the ^{85}Rb $F = 3 \rightarrow F' = 3, 4$ crossover transition; (2) A near-detuned value of 0.75(5) GHz, obtained by coupling a fraction of the main-barrier-beam and the MOT trapping beam into a 1.5 GHz Fabry-Perot cavity, then tuning the main-barrier-beam frequency half way between the MOT-trapping-beam transmission peaks; and (3) A far-detuned value of 3.97(7) GHz, produced by stabilizing the main barrier beam to the ^{85}Rb $F = 2 \rightarrow F' = 2$ transition. The values of these detunings relative to the MOT trapping transition are illustrated in Figure 4.14. For each detuning, we adjust the power of the main barrier beam to ensure that the height of the potential barrier presented to the reflecting atoms remains the same (Section 1.6). Changing the power and detuning of the main barrier beam impacts the number of scattering events we expect for an atom reflecting from the barrier. In particular, we selected the near-detuned value because it is much closer to the $F = 2 \rightarrow F' = 3$ transition than our standard value, but not so much as to substantially increase the expected number of scattering events, which should go up by about a factor of 2. The far-detuned value conveniently lies about halfway between the $F = 1$ and $F = 2$ resonances, and has been employed for atoms starting
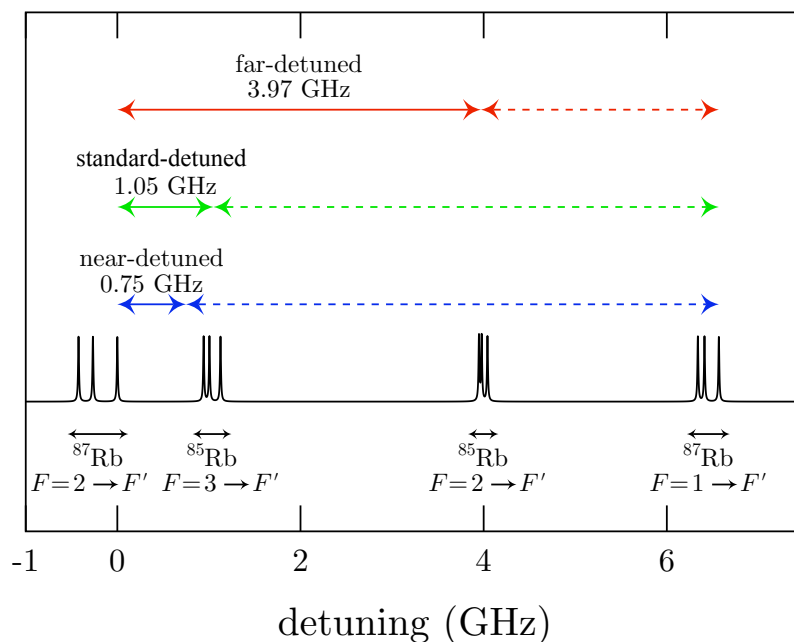
Figure 4.14. A schematic showing the ^{87}Rb D$_2$ emission spectrum and the three detunings used to test the reflectivity of the barrier. The horizontal axis displays the detunings relative to the ^{87}Rb $F = 2 \rightarrow F' = 3$ MOT trapping transition. The solid lines indicate the blue detunings of the barrier for atoms in the $F = 2$ reflecting state, while the dashed lines show the approximate red detunings of the barrier for atoms in the $F = 1$ transmitting state. Figure created by J. J. Thorn.

on the left-hand side of the barrier previously, producing significant trap losses during

transmission (Section 4.4).

Figure 4.15 presents the results, showing the populations on both sides of the

barrier for up to 500 ms as a function of time. The populations on the left-hand

side of the trap are nearly identical for all three detunings, indicating that the

barrier successfully prevents transmission of atoms regardless of its detuning. The

populations on the right-hand side of the trap remain similar for the near-detuned

and standard values; however, we observe a dramatic reduction in population for the
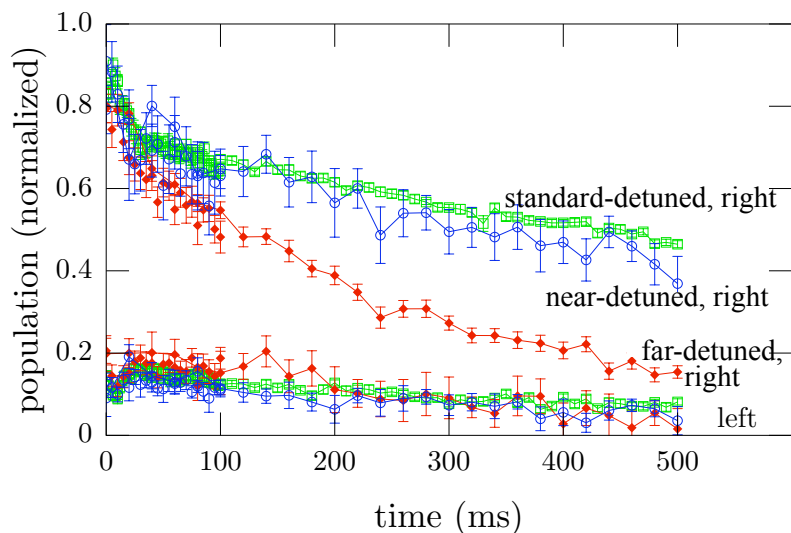
Figure 4.15. Populations on the right- and left-hand sides of the trap as a function of time for three different main-barrier-beam detunings. The atoms initially started in the $F = 1$ transmitting state on the right-hand side of the trap. The three main-barrier-beam-detunings were 0.75(5) GHz, 1.05(5) GHz, and 3.97(7) GHz blue of the ^{87}Rb MOT trapping transition for the near-detuned, standard-detuned, and far-detuned data, respectively. The error bars indicate statistical error for at least 28 repetitions of the experiment.

far-detuned value. We can explain these behaviors in the context of the state changes an atom can undergo when reflecting from the barrier. In particular, an atom that flips from the $F = 1$ transmitting state to the $F = 2$ reflecting state in the presence of the main barrier beam under goes a devastating state change, as it experiences a substantial *increase* in potential energy, and will likely be ejected from the barrier at high speed. On the other hand, and atom that changes from the $F = 2$ reflecting state to the $F = 1$ transmitting state undergoes a relatively harmless state change, as it experiences a *reduction* in potential energy, which cools the atom.

An atom reflecting from the near-detuned and standard-detuned barriers will have a very similar experience, in that for both detunings, the main barrier beam easily pumps reflecting atoms to the $F = 1$ transmitting state due to its proximity to the $F = 2 \rightarrow F' = 3$ resonance—a relatively harmless state change. These detunings, however, do not effectively pump atoms *back* to the $F = 2$ reflecting state, which minimizes these devastating state changes. An atom that has been pumped to the transmitting state during a reflection will nearly exit the main barrier beam before encountering the repumping barrier beam to correct the state change. At this position, near the edge of the main barrier beam, the potential energy increase from flipping back to the reflecting state is minimal. The data in Figure 4.15 suggest that heating solely from scattering barrier-beam photons (that produce relatively harmless state changes) is not a primary source of atom loss, since the near-detuned data, which should suffer about twice as many scattering events, exhibit only slightly more loss.

The situation changes, however, for the far-detuned barrier, for which atoms in either state scatter similar amounts of light. Under these circumstances, an atom reflecting from the barrier may initially undergo a relatively harmless state change to the $F = 1$ transmitting state, but is much more likely to experience a subsequent, devastating state change to the $F = 2$ reflecting state. This devastating state change will likely occur near the center of the main barrier beam due to the atom's reduced speeds during reflection, maximizing the accompanying potential energy

increase. The heating associated with the larger number of devastating scattering events manifests in the considerable trap losses observed in Figure 4.15.

CHAPTER V

COOLING WITH THE ONE-WAY BARRIER

Figures 5.2 and 5.4-5.7 were published in the coauthored work, Ref. [103].

5.1. Introduction

The field of atom optics has risen to prominence on the shoulders of a few, robust laser-cooling techniques that are astonishingly effective on a handful of atomic species [36]. Though duly celebrated, these techniques generally require multiple scattering events to reduce the kinetic energy of an atom, necessitating a cycling optical transition. In the absence of a reliable cycling transition, atoms decay into states that are inaccessible to the cooling laser, failing to undergo further cooling. With a few exceptions [104–109], only a small subset of atoms have an electronic structure simple enough to meet this requirement, significantly limiting the breadth of ultra-cold physics research. This creates a need for new, innovative cooling tools that are applicable to more complex atoms and molecules to broaden the scope of the research.

One-way-barrier cooling schemes [79, 81, 85, 86, 88, 89, 103] emerge as an ideal candidate due to the small number of scattering events necessary to achieve cooling. In principle, only a single scattering event—one that switches the atom from the

transmitting to the reflecting state—is required to effect cooling, circumventing the difficulties arising from the complex electronic structure of many atoms and molecules [110]. In this chapter we will discuss how one-way-barrier cooling schemes work, describe our particular implementation, and present our results [103]. We will also examine the impact of experimental heating effects in general, as well as on the effectiveness of the cooling process.

5.2. How It Works

The cooling utility of the one-way barrier stems from its ability to compress the volume of a sample of gas, as described in Section 3.3. Once the barrier has achieved compression, increasing the volume by slowly translating the barrier cools the gas via adiabatic, reversible expansion (Fig. 5.1). The term "adiabatic" indicates that no heat transfer occurs during the expansion, while reversibility requires that the translation speed of the barrier must be slow compared to the average speed of the gas particles. For particles in potentials, this is sometimes referred to as adiabatic translation, since the translation is slow enough that the change in potential experienced by the atom does not significantly increase its kinetic energy. The expansion cools the gas for the same reason that adiabatic compression raises the temperature (Section 3.3): The net entropy change for an adiabatic process is zero, so the entropy increase associated with the larger volume must be counteracted by an equivalent entropy decrease, which is manifest in the lower temperature of the gas.
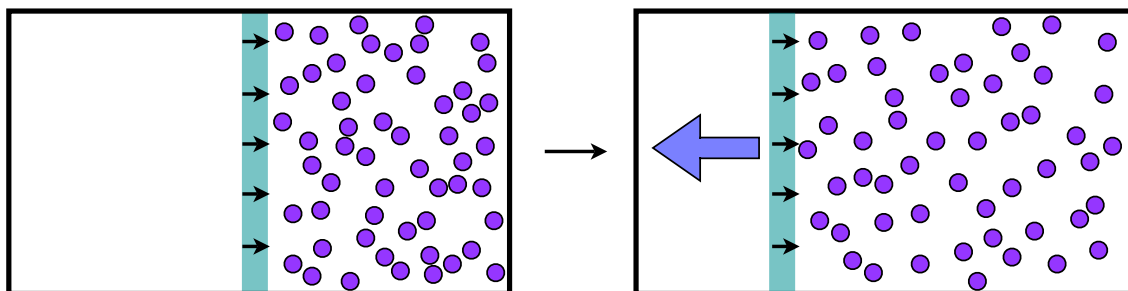
Figure 5.1. Illustration of how to use the one-way barrier to cool a sample of gas via adiabatic expansion, modified from an original created by J.J. Thorn.

Though simple in concept, this two-step process (spatial compression followed by adiabatic expansion) does not speak to the viability of one-way-barrier cooling schemes. In particular, if the temperature increase suffered during the compression step is too large, it will negate any cooling benefit derived from the expansion. The success of this cooling method hinges on the barrier's ability to decrease the phase-space volume of the gas during compression. The phase-space volume, which takes into account changes in both volume and temperature (Section 1.8), will decrease during the compression process if the effect of the volume compression outweighs any heating that occurs. Indeed, phase-space volume compression has been demonstrated with one-way barriers [89, 90, 111], with our results reported in Section 4.5, and the best result achieved so far yielding a factor of 350 compression from the initial conditions [111].

A more elegant approach to cooling with the one-way barrier involves combining the compression and adiabatic expansion steps by confining the gas in a harmonic potential and sweeping the barrier through the sample (Fig. 5.2) [85]. In this scheme,
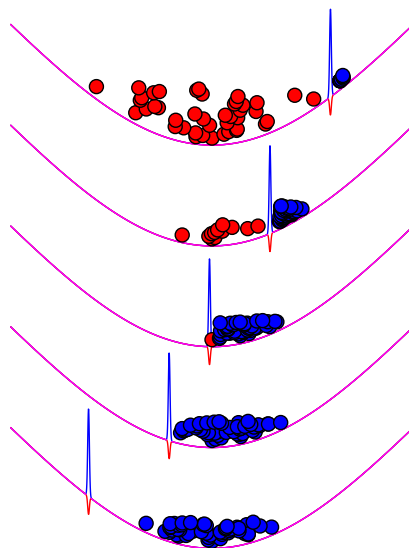
Figure 5.2. Schematic representation of the one-way-barrier cooling process for a gas confined in a harmonic potential. Gas particles near their turning points pass through the barrier and become trapped on the right-hand side, then reduce their potential energy by following the barrier to the bottom of the potential. This figure was created by J.J. Thorn.

the harmonic potential governs the motion of the gas particles, which regularly exchange kinetic and potential energy as they oscillate back and forth in the harmonic trap. As the one-way barrier is translated from one side of the trap to the other, gas particles encounter the barrier near their turning points—when they have very little kinetic energy—becoming trapped by the slowly moving barrier. The trapped particles proceed to follow the moving barrier to the bottom of the potential, reducing their potential energy with minimal increase in kinetic energy, cooling the sample of gas.

The translation speed of the barrier plays a critical role in the effectiveness of this cooling scheme. For the sweep to be adiabatic, the distance the barrier travels

during one oscillation period of the gas particles must be small compared to their oscillation amplitude. Sweeping the barrier too quickly limits the minimum achievable temperature of the process by trapping particles away from their turning points, when they have greater amounts of kinetic energy. It also contributes to unnecessary heating by increasing the kinetic energy of the already-trapped particles as they "fall" toward the receding barrier. Treating the particles classically and assuming they "see" a linear change in the potential over a small translation step of the barrier, the temperature of a particle when it "catches up" with the barrier is proportional to v_0^2, where v_0 is the translation speed. This implies that the cooling technique becomes more effective as the translation speed of the barrier is reduced, ignoring spontaneous emission.

5.3.   Experimental Setup

The bulk of the experimental apparatus and procedures for the cooling experiment remain the same as for the barrier-demonstration experiment (Chapter 4), except for a few substantial differences which we will detail below.

The primary difference arises from the need to translate the barrier to implement the cooling scheme. We conveniently mounted the output of the dipole-trap laser on the air cart (Section 2.5), which allows us to sweep the dipole trap (with the atoms) through the barrier beams. Translating the barrier beams through the dipole trap—the approach used in describing the cooling method—would have required

considerable changes to the apparatus that were not conducive to its future uses. Except for the force the atoms experience due to the acceleration and deceleration of the trapping potential, these two configurations are equivalent, however, provided the translation is adiabatic.

We originally aligned the dipole-trap beam to intersect the MOT and one of the dumping mirrors (Section 2.5, Fig. 2.25), which produced a beam that was not parallel to the table nor to the translation direction of the air cart due to the geometry of our apparatus. Though this setup sufficed for our one-way barrier experiments, it proved inadequate for the cooling experiment because translating the air cart shifted the dipole-trap beam off the dumping mirror and moved the focus of the dipole trap in all three dimensions (as opposed to just axially), misaligning it with the barrier beams. In order to implement the cooling experiment, we realigned the dipole-trap beam parallel to the table and angled the air cart parallel to the beam path that intersected the dumping mirror (Fig. 5.3).

These changes enabled us to translate the dipole-trap without compromising its alignment with the barrier beams or the dumping mirror; however, they produced a new set of technical challenges. In particular, the low height of the dumping mirrors forced the dipole-trap beam to pass far below the standard MOT position near the center of the Hellma cell (Fig. 5.3), requiring us to load the dipole trap uncomfortably close to the bottom of the cell (about 4.2 mm above it). So close, in fact, that there was insufficient MOT-trapping and repump light to form a MOT at that low of a
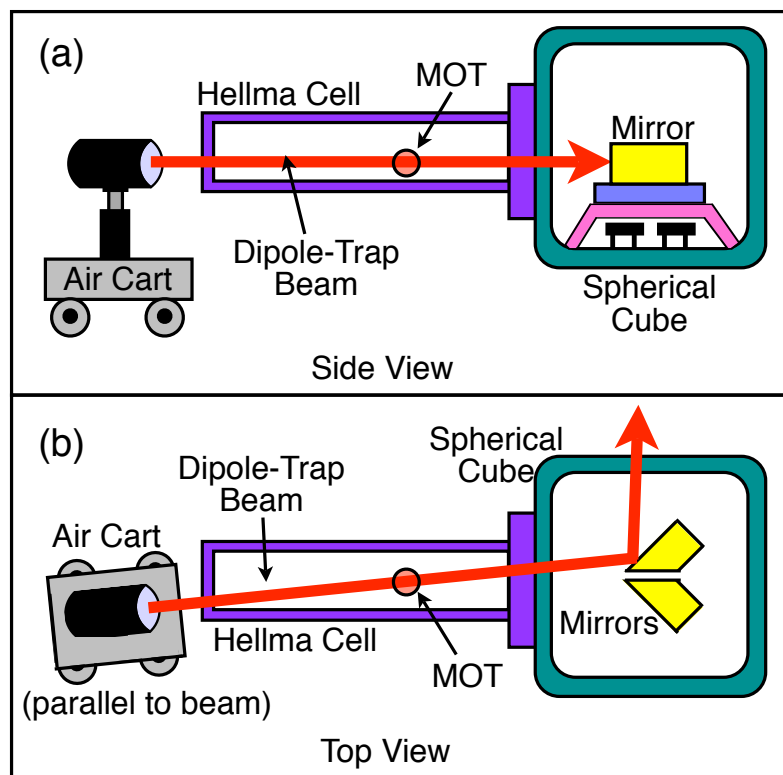
Figure 5.3. Schematic diagram showing the alignment of the dipole-trap beam with the MOT and the dumping mirrors for the one-way-barrier cooling experiments, including the air cart, dipole-trap beam, Hellma cell, MOT, spherical cube and dumping mirrors. Figure 2.25 shows the previous alignment for the one-way-barrier demonstration experiments. (a) Side view illustrating how the dipole-trap beam must pass close to bottom of the Hellma cell to be parallel with the optical table. (b) Top view illustrating the orientation of the air cart to ensure the translation direction is parallel to the dipole-trap-beam direction.

position. To remedy this, we shifted the MOT beams down by $3/16''$, and adjusted

the Helmholtz and anti-Helmholtz coil values to form a strong, fast-loading MOT

lower in the cell (referred to as the "new position"), though still higher than the

dipole-trap position.

Changing the beam positions affected several other aspects of the experiment.

First, to image the atoms effectively, we had to lower the height of the absorption

imaging beam and the camera. Second, we had to angle the barrier beams downwards using the steering mirror (mirror 2) to overlap them with the dipole-trap focus. The most significant effect, however, was on the MOT and dipole-trap loading procedures. In the case of the MOT, we were no longer able to use the trick of loading the MOT up high in the atomic beam (Section 4.2) to bolster the atom numbers, as the MOT beams were now too low to form a MOT at that height. Unfortunately, this reduced the number of atoms we were able to load into the dipole trap. For loading the dipole trap, the lowered MOT beams provided enough light to form a MOT near its focus, but the MOT was too weak to efficiently load the dipole trap. As a result, we loaded the MOT in the new position (which was still much higher than the position of the dipole trap), then rapidly shifted the MOT to the dipole-trap position with the magnetic bias fields for loading. Though the size of the MOT decayed at this lower position, the time scale for the decay was much longer than the loading time of the dipole trap.

Aside from the lower position, the dipole-trap parameters remained the same as reported previously (Section 4.2). This includes the operating power, beam waist, trap depth, and oscillation frequencies.

To carry out the cooling experiment, we load the MOT for 7 s at the new position, trapping approximately 1.4×10^5 atoms at about 30 μK. We then shift the MOT 0.95(5) mm left of the dipole-trap focus with the magnetic bias fields for loading. Loading off to the side improves the loading efficiency as well as effectively

increases the initial temperature of the dipole-trapped atoms. Heating the atoms prior to the measurement ensures the initial ensemble is much warmer than the lowest temperature achievable with our setup, which is significantly limited by experimental constraints and heating effects (see Sections 5.6 and 5.7). We load the dipole trap for 110 ms, filling it uniformly with about 8×10^4 atoms at a temperature of approximately 110 μK, then leave the MOT light on for an extra 15 ms to optically pump the atoms to the $F = 1$ ground state. Next we modulate the intensity of the dipole-trap laser using a square wave with a 24 ms period, switching between 100% and 120% of the nominal operating power for 100 periods. The modulation heats the atoms further via parametric excitation [112], resulting in approximately 4×10^4 atoms at a temperature of about 170 μK in the dipole trap.

The geometry of the one-way barrier remains largely intact (Section 3.4), except we increased the beam separation to 36(1) μm to minimize heating on the reflecting side of the barrier. We also reduced unwanted heating by lowering the power of the main barrier beam to 24(2) μW, since the atoms trapped by the barrier have very little kinetic energy and therefore do not require as high a potential barrier. The repumping-barrier-beam power remains relatively unchanged at 0.34(3) μW. Both beams were left linearly polarized perpendicular to the dipole-trap axis, and the other barrier-beam parameters remain the same as reported previously (Section 3.5).

As mentioned in Section 5.2, the adiabatic-translation requirement dictates that the sweep speed of the barrier must be slow compared to the average speed of the

oscillating atoms. After heating, the average speed of an atom in the dipole trap during one oscillation period is roughly 100 mm/s, so we want a translation speed at least an order of magnitude smaller. Additionally, we remained cognizant of the limited trap lifetimes in the presence of the barrier (about $700-900$ ms), which inhibit us from selecting an arbitrarily slow sweep speed. These considerations informed our choice of a 5 mm/s translation speed, which we reasoned would provide a balance between improved cooling and atom loss due to scattered light from the barrier beam. Section 5.5 examines how the translation speed affects the performance of the cooling scheme in detail.

The series of steps to execute the cooling experiment is as follows: First, the atoms are loaded into the dipole-trap and optically pumped to the $F = 1$ transmitting state with the air cart at the location where the dipole-trap focus intersects the main barrier beam. Next, we translate the trap 2.5 mm to the left of the barrier position (as seen by the camera) at 5 mm/s (Fig. 5.4). During this movement, we heat the atoms via dipole-trap intensity modulation for 2400 ms then turn on the barrier beams. At time $t = 0$, we translate the air cart 1.5 mm to the right of the barrier position at a speed of 5 mm/s. We begin recording images 290 ms after the sweep starts, just as the atomic cloud starts to pass through the barrier. We continue to record images every 30 ms until about 500 ms after the air cart has come to rest (Fig. 5.4). We note that the atoms are still in motion when many of the images are taken, and that each measurement is destructive, so we repeat the series of events for each image.
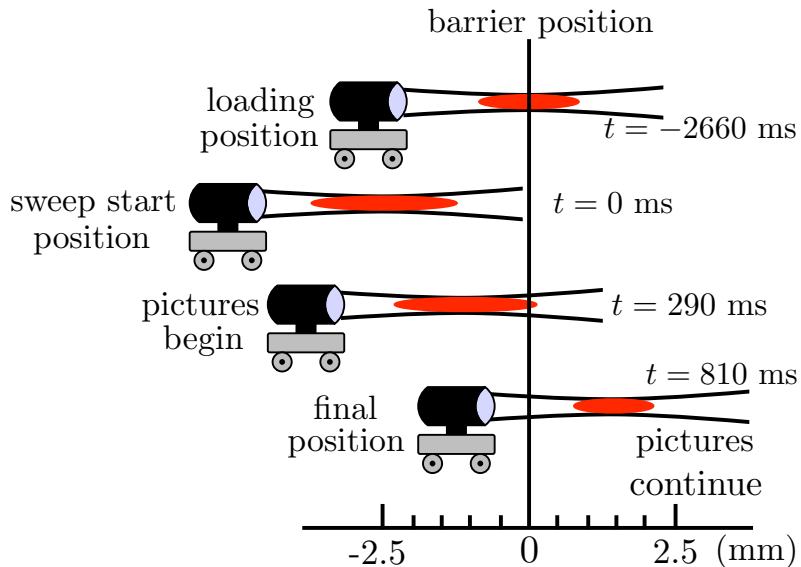
Figure 5.4. Illustration of the dipole-trap translation and imaging sequence. The times shown correspond to a translation speed of 5 mm/s.

5.4. Demonstrating Cooling

The atomic spatial distributions in the dipole trap during the sweep in the presence and absence of the one-way barrier are presented in Figure 5.5. The barrier is located at the origin of the plot and the hot atomic distributions are translated through the barrier from left to right. At time $t = 290$ ms, the warmest atoms in the sample just start to encounter the barrier, becoming trapped on its right-hand side. These trapped atoms appear as a small peak in the data with the barrier, visible to the right of the barrier position. The peak continues to grow as the translation progresses, since more atoms become trapped near their turning points, evidenced by the larger peak in the atomic distribution at time $t = 440$ ms. The trapped atoms reduce their potential energy by adiabatically following the barrier to the bottom of the potential,

with minimal increase in their kinetic energy. All the atoms have become trapped by the time the center of the dipole-trap passes through the barrier, which slowly expands the cooled, asymmetric distribution in the harmonic potential. This stage of the cooling process is captured in the atomic distribution with the barrier at time $t = 590$ ms. It is important to note that the width of the spatial distributions does not accurately reflect the temperature when the barrier is in contact with the atoms (as it is for the data at $t = 440$ ms and 590 ms), because the harmonic dipole-trap potential is effectively cut in half by the one-way barrier potential. The spatial distributions at $t = 740$ ms and 890 ms demonstrate the cooling effect of the sweep, manifest in their narrower widths as compared to the distributions without the barrier. We believe several possible heating mechanisms are responsible for the slow increase in temperature (width) observed at times $t = 1040$ ms and $t = 1190$ ms, where the cooling effect of the barrier becomes less obvious. Section 5.7 contains an in-depth discussion of the possible heat sources contributing to this warming effect.

Figure 5.6 shows the width of the atomic ensemble before, during and after the cooling process with and without the barrier, measured as the FWHM of the spatial distributions presented in Figure 5.5. The vertical line marks the time when the translation has finished. Prior to this time, the width is not an appropriate indicator of temperature for the distributions with the barrier because it is still interacting with the atoms, as mentioned previously. After completing the sweep, the atoms are cooled to about 100 μK, reflecting a factor of 1.7 reduction in the temperature after
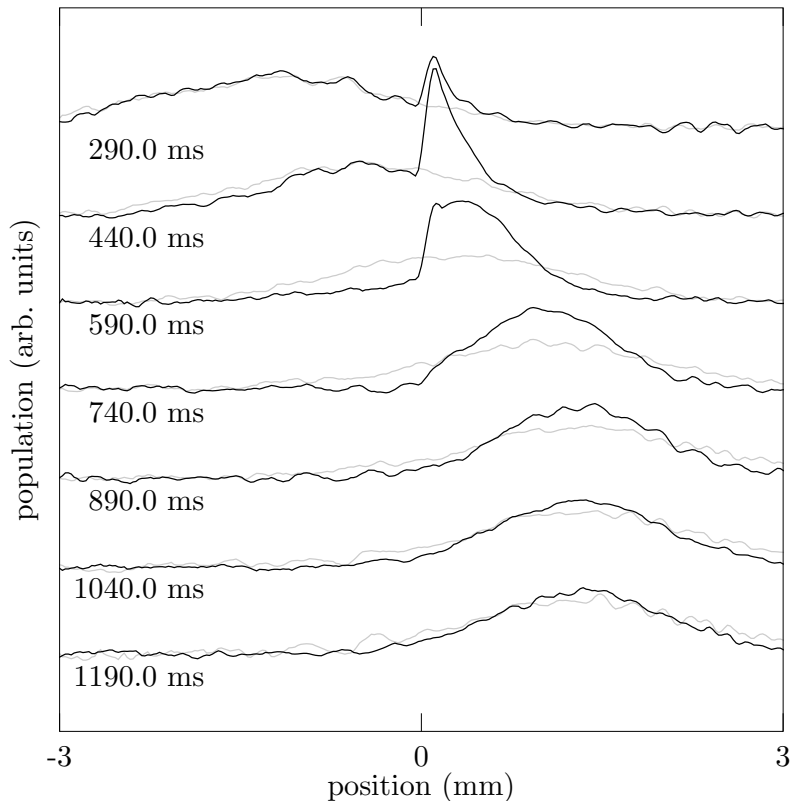
Figure 5.5. Atomic distributions in the dipole trap during translation with (black curves) and without (gray curves) the one-way barrier. The barrier beams are located at position zero. Each curve is an average of 16 repetitions of the experiment, smoothed slightly for clarity.

cooling in one dimension. This corresponds to a factor of 1.7 reduction in the phase-space volume when accounting for the spatial compression and temperature change. Previous work for an earlier one-way-barrier cooling scheme reported greater phase-space compression [111], however, we note that the two experimental realizations are substantially different. First, Bannerman *et al.* employed a magneto-optical configuration, transferring atoms from a magnetic trap into an optical trap, while we demonstrated an all-optical realization, which requires higher powers and more
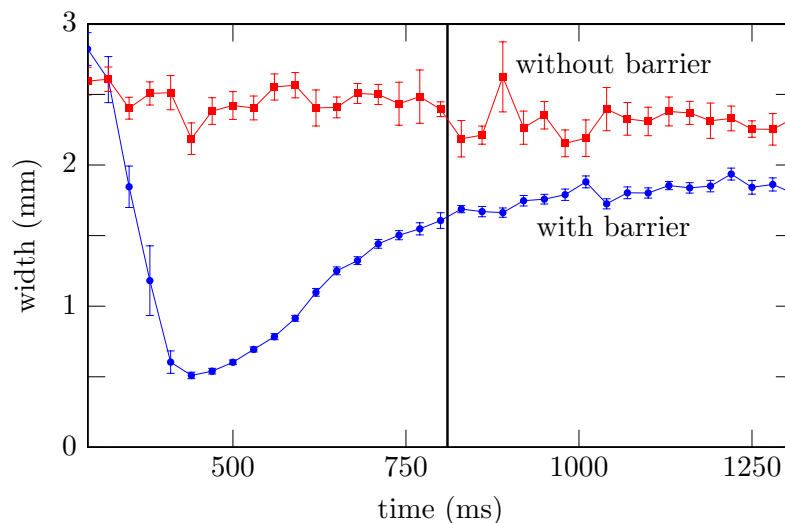
Figure 5.6. The FWHM of the spatial distribution in the dipole trap as a function of time during the translation with (squares) and without (circles) the one-way barrier. The times are measured from the start of the sweep and the vertical line delineates the time when the sweep has finished. The error bars indicate the standard deviation for the average of 16 repetitions of the experiment.

scattering events. Second, we cool nearly 100% of the atoms initially loaded into the dipole trap, while they report a 0.3% transfer efficiency between the magnetic trap and the optical trap [111]. Our implementation ought to perform better, though, as simulations of the cooling process reveal that a factor of nine cooling should be achievable. We believe the origin of this discrepancy comes from the previously mentioned heating effects counteracting the cooling process, which are also manifest in the slow increase in temperature observed in Figure 5.6 after the sweep has ended.

5.5. Effect of Translation Speed

As discussed earlier (Section 5.3), we expect the efficiency of the cooling scheme to improve as we reduce the barrier's translation speed through the trap. However, experimental realities for our implementation also indicate that translating the barrier too slowly will result in increased heating due to scattering in the presence of the barrier (Section 4.4). Figure 5.7 shows the width of the atomic distribution after passing through the barrier for several different sweep speeds. The data appear in two different sets (circles and squares) due to the large deceleration distances that accompany the high translation speeds. In particular, we want to prevent the air cart from starting to decelerate while the barrier is in contact with the atomic sample to ensure that the entire sweep is completed at a constant velocity. As a result, the data represented by the circles were taken while the air cart passed 1.5 mm at constant velocity. The data represented by the squares have velocities slow enough that the images were taken as the air cart decelerated to rest at a position of 1.5 mm. These two data sets partially overlap, which raises some concerns about timing. In particular, to accurately compare the cooling effects at the same velocity under the different experimental conditions (constant velocity versus decelerating at the time of the image), it is imperative that the length of time between passing through the barrier and taking the image coincides as closely as possible for each velocity. This concern arises from the additional heating that occurs while the atoms reside in the dipole-trap after completing the sweep, which increases the width of the distributions

over time. To address this concern, the images represented by the squares were taken at times that matched the constant-velocity data (circles) as closely as possible. The overlap in the two data sets also provides us valuable insight into the effects of the air-cart motion on the temperature of the atoms. The good agreement between the overlapping data points indicate that no discernible heating can be attributed to the deceleration of the air cart. For velocities above 25 mm/s in Figure 5.7, we observe a rapid increase in the width of the atomic distribution, which is consistent with the expectation that at high speeds the translation ceases to be adiabatic. The width of the distribution after the sweep narrows at lower velocities, reaching a minimum at about 10 mm/s. Below this velocity, the widths begin to increase again as the atoms spend longer amounts of time trapped against the barrier, scattering more barrier-beam light that heats the atomic sample.

5.6.   Limitations

Several factors resulting from our particular implementation limit the effectiveness of this cooling scheme. First, we treat the system as effectively one-dimensional because the single-beam, far-detuned dipole trap results in disparate longitudinal and radial oscillation frequencies (Section 4.2). Simulations reveal, however, that the transverse dimensions can contain a substantial amount of kinetic energy [78]. Our work is limited by the fact that we exclusively cool the atoms in the longitudinal dimension.
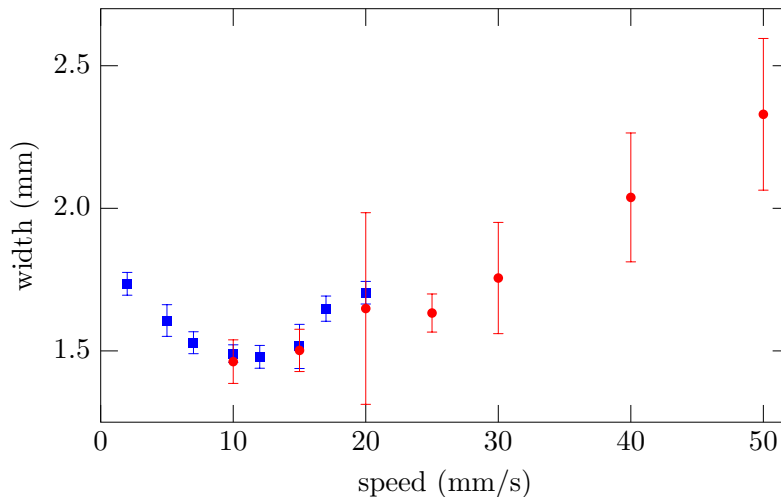
Figure 5.7. The width of the atomic distribution in the dipole trap as a function of translation velocity, measured after passing through the barrier. The circular data points represent measurements taken as the air cart passed 1.5 mm at constant velocity, while the square data points represent measurements taken as the air cart came to rest at 1.5 mm. Each square (circular) data point corresponds to the average of 16(6) repetitions of the experiment, with the error bars indicating the standard deviation.

The relatively small hyperfine ground-state splitting of ^{87}Rb, which constituted the main experimental challenge throughout our one-way barrier work, imposes the second, significant limitation inherent in our experiment. As discussed on several occasions (Section 3.4, 4.4, 4.6.1, and 4.6.4), the atoms undergo an excessive number of scattering events when interacting with the barrier due to the restricted detunings afforded by the hyperfine ground-state splitting, leading to heating and trap losses that limit the lifetimes in the presence of the barrier. For example, the moving barrier produces about 3 scattering events during transmission and around 4 scattering events during reflection. This has serious implications for the effectiveness of this cooling scheme, as it requires repeated reflections from the barrier to cool the atoms during

the adiabatic translation process. In particular, the excessive scattering prevents us from sweeping the barrier arbitrarily slowly, because at some point the heating and trap losses will overcome any cooling benefit derived from the slower translation speed. We observe evidence of this limit in Figure 5.7.

Increasing the frequency difference between the transmitting and reflecting states to allow for larger detunings stands out as the most obvious improvement to this cooling scheme. Section 4.4 mentions several ways to accomplish this, ranging from utilizing the fine structure of ^{87}Rb to realizing the cooling technique with a different atomic or molecular species that has a more versatile level structure. Clearly, applying this cooling method to a new atom or molecule warrants careful consideration of the atomic structure and the detuning of the main barrier beam.

5.7. Anomalous Heating

As alluded to in Section 5.4, our one-way-barrier cooling experiment successfully reduces the temperature of the atomic ensemble, only to have the cooling gains slowly eroded as the atoms reside in the dipole trap after the sweep. This increase in temperature, visible in Figures 5.5 and 5.6 as the widening of the atomic distributions, makes up most of the temperature difference between the cooled and uncooled samples in about the first 700 ms after the sweep has finished. Figure 5.8 shows the width of the atomic distribution as a function of time for atoms with and without the barrier for several seconds after a 10 mm/s sweep. It is clear that after their initial reduction
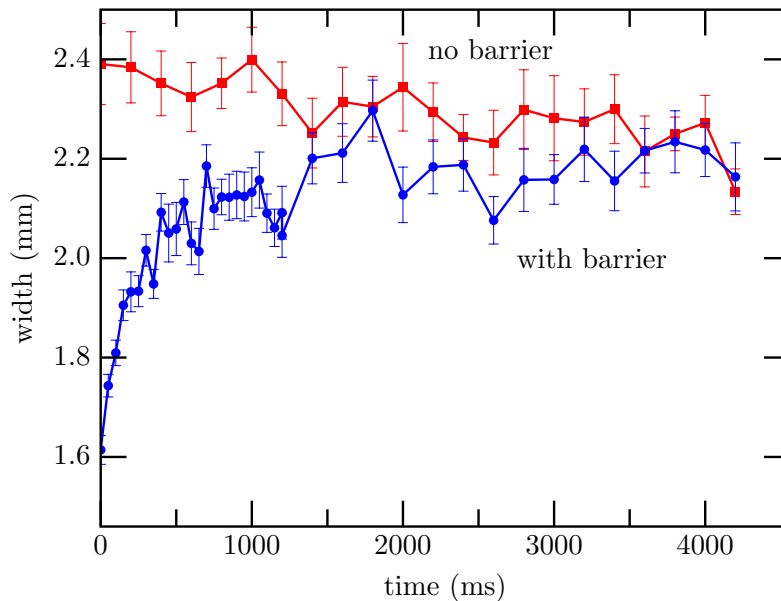
Figure 5.8. The width of the atomic distribution in the dipole trap for atoms translated at 10 mm/s with (blue) and without (red) the one-way barrier for several seconds after the sweep has finished. The error bars represent statistical error for 16 repetitions of the experiment.

in temperature, the atomic sample starts to warm, eventually reaching close to a steady-state temperature (there is a slow linear increase) almost equivalent to the uncooled sample after about 3.5 s. This perplexing behavior mandates that energy is either being added to the system or redistributed by some means, though the cause is not immediately obvious. Below we will detail our efforts to track down the source of this anomalous heating.

Examining our system, we determined three potential heating sources: the one-dimensional nature of our cooling scheme, the barrier, and the air-cart motion. In the case of the first, we know that significant amounts of energy can be present in the transverse dimensions [78], such that any anharmonic coupling between the

longitudinal and radial degrees of freedom could redistribute some of the transverse kinetic energy to the longitudinal dimension after the sweep. Should this be the case, sweeping the barrier through the atoms twice should reduce the final temperature of the ensemble, provided the sweep does not add the same amount of energy back into the system. Figure 5.9 shows the width of the atomic distribution as a function of time after one and two sweeps through the barrier at a velocity of 10 mm/s. We see that immediately after completing the sweep(s) (time $t = 0$), the ensemble that passes through the barrier twice is a little bit cooler, then quickly warms to a (near) steady-state temperature slightly lower than the one-sweep sample. It is important to note that the time the atoms reside in the dipole trap before the second sweep is about 600 ms, such that their temperature prior to the second sweep is close to the (near) steady-state value achieved after one sweep. These data suggest that a small amount of the heating can be attributed to anharmonic coupling between the cooled and uncooled degrees of freedom, evidenced by the slightly narrower width of the atomic distribution after completing two sweeps through the barrier (Fig. 5.9).

Our previous work with the one-way barrier indicates that the separation of the barrier beams and their depth of focus (z-direction, Fig. 3.11) alignment with the dipole-trap focus affect the number of expected scattering events, and thus heating due to contact with the barrier. To this end, we doubled the separation of the barrier beams to 65 μm, and repeated the experiment with the same parameters used to collect the data in Figures 5.5 and 5.6. Increasing the separation had no discernible
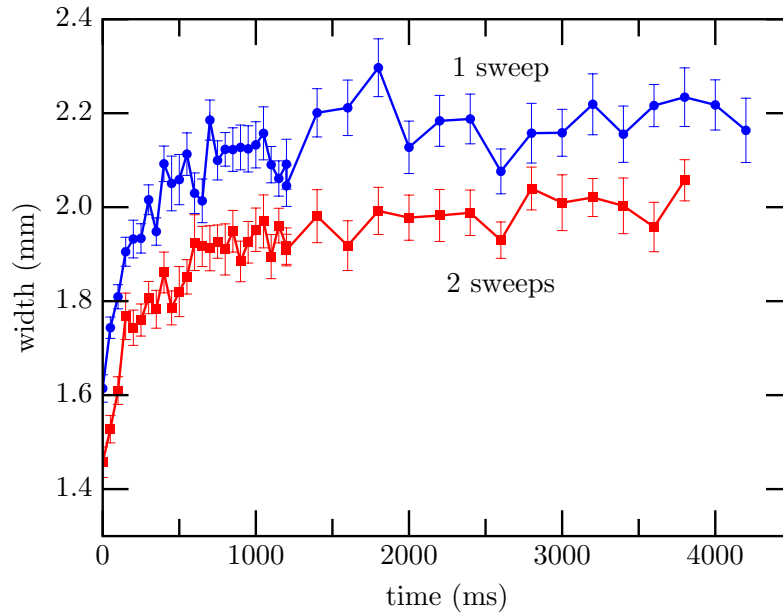
Figure 5.9. The width of the atomic distribution after completing one (blue) and two (red) sweeps through the barrier as a function of time for $v = 10$ mm/s. The error bars represent statistical error for 16 repetitions of the experiment.

impact on the width of the atomic distribution, as the data mimicked that collected

for the smaller separation.

To address the alignment issue, we meticulously realigned the foci of the barrier

beams with the dipole-trap focus using the method outlined in Section 3.7. We

calculated that about a 0.5 mm offset in the z-direction places the barrier foci about

one Rayleigh length ($\sim$0.53 mm) away from the dipole-trap focus due to their small

beam waists in the longitudinal direction. At one Rayleigh length away from the

foci, the waist of the barrier beams increases by about 40%, revealing that even

small displacements can substantially increase the width of the barrier beams at

the position where they intersect the dipole trap. We determined that we were off by

about 0.38 mm, likely resulting from the major repositioning of the air cart and dipole-trap beam necessary to perform the one-way-barrier cooling experiment. However, the data collected after the realignment showed no appreciable improvement in the final temperature of the atomic distributions despite the more precise alignment. We note, however, that some uncertainty in the overlap of the dipole-trap beam with the barrier beams persists as our alignment method limits us to a resolution of roughly 0.34 mm. Considering this, we cannot rule out the possibility that uncertainty in the alignment may contribute to the heating. It is worthwhile to acknowledge that there is no compelling reason to assume these possible heating mechanisms play a role in the heating that occurs *after* the sweep has concluded, when the atoms are no longer in contact with the barrier. However, in an effort to understand and characterize the problem, we felt it prudent to investigate all potential heating sources.

The motion of the air cart generates some concern in the context of the heating effects, particularly because we are actually moving the atoms as opposed to the barrier beams. Of particular concern is the deceleration of the air cart as it comes to rest after the sweep, which can potentially impart energy to the atoms, or vibrate the air cart or the affixed optics at a frequency that heats the atoms. Vibrations that could cause heating should have a period close to the longitudinal oscillation period of the atoms in the dipole trap (about 50 ms, or 20 Hz) [113], and must occur over a time period of several hundred milliseconds to account for the heating observed in Figure 5.8.

The nominal deceleration (and acceleration) of the air cart is 500 mm/s^2, though we have the ability to change it with the computer. We used the same method to test for longitudinal vibrations of both the air cart and the attached optics, which involved affixing a razor blade to the equipment of interest, which then partially intercepted a laser beam focused onto a photodiode as the air cart came to rest. Figure 5.10 shows the measured laser power as a function of time for two different accelerations ($a = 100$ and 500 mm/s^2) at three different velocities ($v = 5$, 10 and 20 mm/s), with the razor blade attached to the air cart. The two horizontal lines indicate the laser intensity for two different air-cart positions separated by 10 μm, which provide a scale for the amplitude of the vibrations. We observe a distinct vibration with a period of about 40 ms as the air cart comes to rest for all speeds and accelerations; however the amplitude is much greater when the acceleration is 500 mm/s^2. Though the vibration period falls in the range necessary for heating, we see that all the vibrations rapidly damp away after about one oscillation period, regardless of their amplitude. The data produced with the razor blade attached to the optics (as opposed to the air cart) look nearly identical, indicating that the optics are fixed rigidly to the air cart. These data suggest that neither longitudinal vibrations of the air cart nor the affixed optics are responsible for any significant heating over the time scale of interest.

To look for signs that the air cart imparts energy to the atoms during the deceleration process, we took images of the atoms in the dipole trap as the air cart came to rest (no barrier) for the same velocity and acceleration combinations used
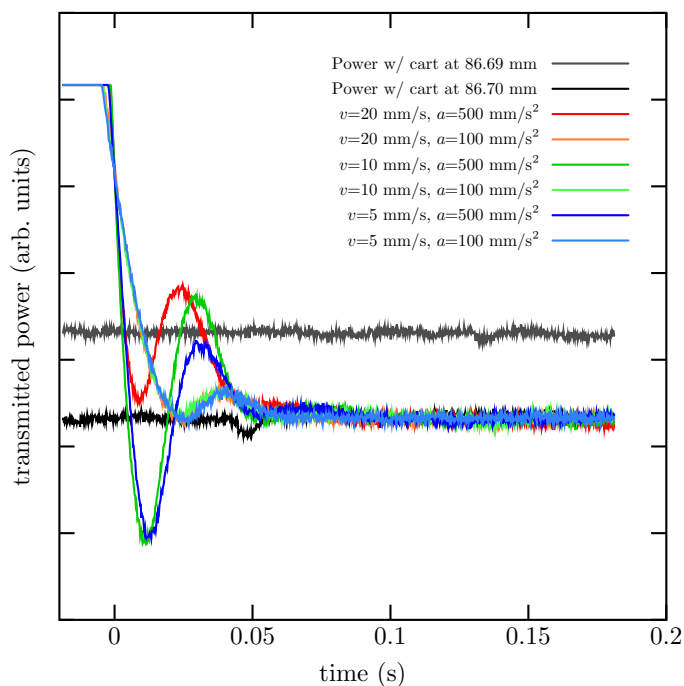
Figure 5.10. The power reaching a photodiode (measured on an oscilloscope) as the air cart comes to rest, partially blocking a laser beam with an attached razor blade. The data show all six combinations of the air-cart's velocity for $v = 5, 10$ and 20 mm/s and acceleration for $a = 100$ and 500 mm/s^2. The two horizontal traces delineate the power for two air-cart positions separated by 10 μm, which provides a distance scale for the observed vibrations.

in the vibration tests. Figure 5.11 presents the results, showing the position of the center of the atomic distributions as a function of time for 250 ms after the translation has ended. We observe that the atoms exhibit some collective oscillation about the center of the dipole trap for the 500 mm/s^2 acceleration at the higher velocities, which damps away after about 200 ms. This collective motion is markedly reduced for the slower-acceleration and lower-velocity data, however, indicating that the deceleration process does impart some energy to the atoms, the amount of which depends on the acceleration and velocity of the air cart. To assuage our concerns
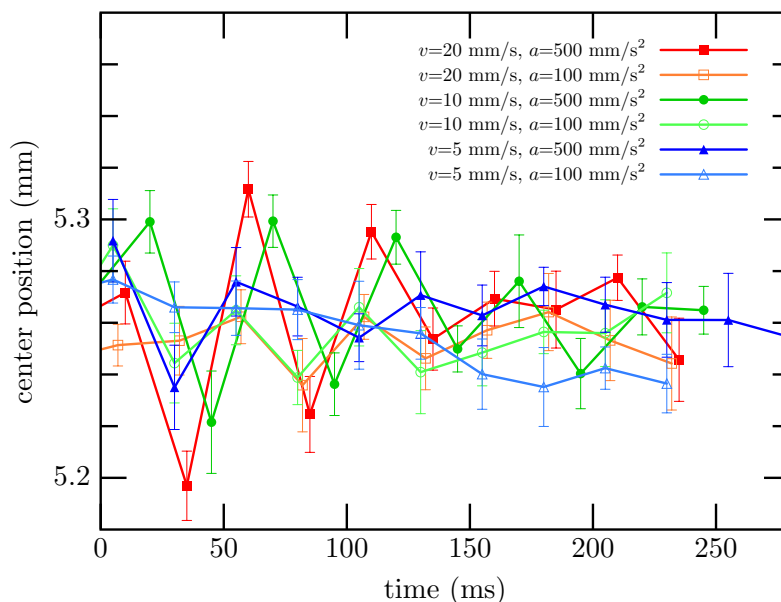
Figure 5.11. The center position of the atomic distribution in the dipole trap after the air cart has come to rest as a function of time. The data show all six combinations of the air-cart's velocity for $v = 5, 10$ and 20 mm/s and acceleration for $a = 100$ and 500 mm/s^2. The error bars represent statistical error for 14 repetitions of the experiment.

about the effects of the air-cart acceleration, we collected data on the width of the atomic distribution after the air cart came to rest from a velocity of 5 mm/s with an $a = 100$ and 500 mm/s^2 deceleration (Fig. 5.12). The two different sets of data are indistinguishable, leading us to conclude that the motion and acceleration of the air cart have no impact on the heating effects observed in our system.

While working on diagnosing the cause of the anomalous heating, we discovered that loading the atoms at the center of the dipole trap produced an ensemble with an initial width comparable to the width of the atomic sample immediately after passing through the barrier. To our surprise, we also discovered that these atoms
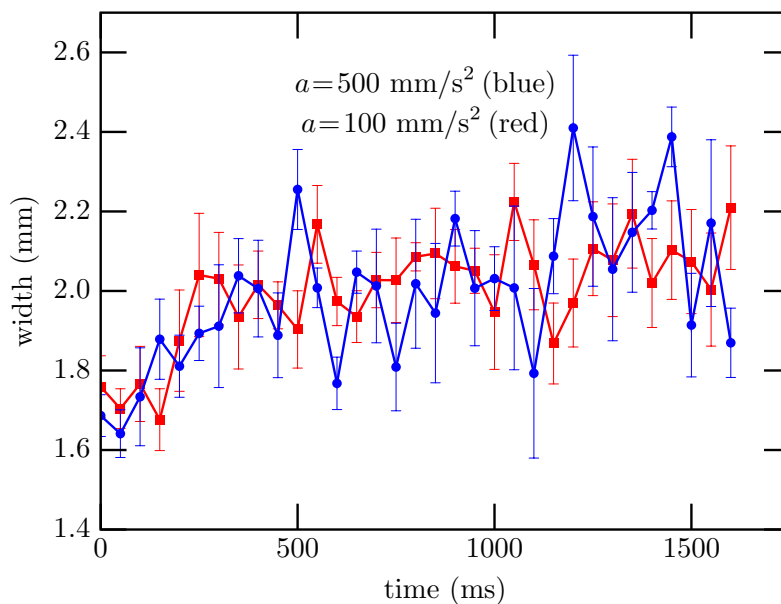
Figure 5.12. The width of the atomic distribution after the air cart has come to rest as a function of time for an acceleration of 100 (red) and 500 mm/s^2 (blue) and a velocity of 5 mm/s. The error bars represent statistical error for 12 repetitions of the experiment.

suffer a similar increase in temperature while residing in the dipole trap, despite the absence of the barrier or any air-cart motion. Figure 5.13 compares the width of the atoms as a function of time for a sample swept through the barrier once and a sample simply loaded in the center of the dipole trap. The time scale of the width increase for the center-loaded atoms is a little smaller (about 500 ms, measured from data not shown here), and the sample warms to a lower (near) steady-state temperature (it too, exhibits a slow, linear increase thereafter) than that of the atoms that interact with the barrier. This discovery reveals that while the barrier/air-cart motion does contribute some to the anomalous heating, a major component of this phenomenon must have nothing to do with the cooling process or its associated mechanics, but
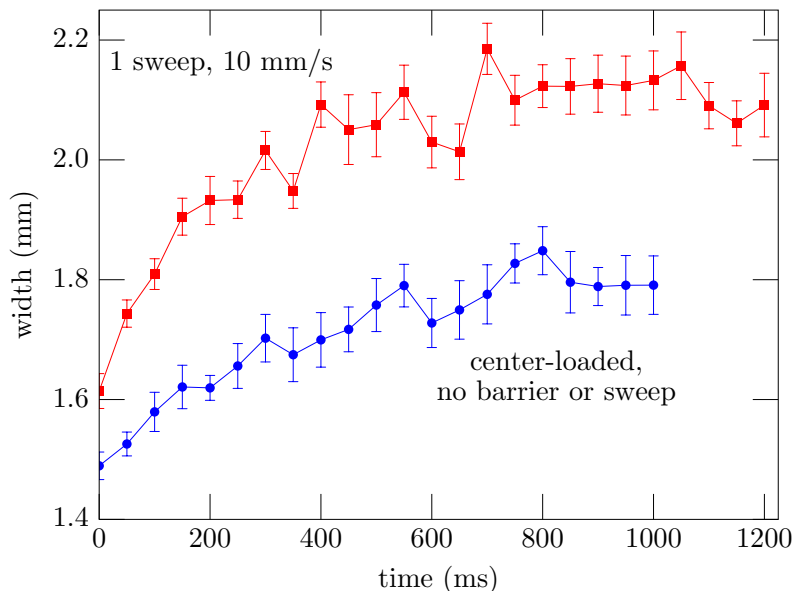
Figure 5.13. The width of the atomic distribution as a function of time for atoms loaded into the center of the trap with no barrier or air-cart movement (blue) and for atoms swept through the barrier once at 10 mm/s (red). The error bars for the no-sweep (sweep) data represent statistical error for 14 (16) repetitions of the experiment.

instead results from our general experimental setup or the dipole-trap laser and its interaction with the atoms. Indeed, several experiments using dipole traps have reported unexplained heating effects as well [114–117].

When considering heating sources associated with our experimental setup and the dipole-trap laser, several possibilities come to mind. These include vibrations of the fiber that connects to the dipole-trap laser's collimator, stray light, dipole-trap-laser intensity fluctuations, dipole-trap loading power, dipole-trap operating power, lensing through the Hellma cell due to heating of the fused silica by the dipole-trap laser, a fluctuating spatial-mode structure, and spectral components of the dipole-trap laser

that could drive the hyperfine transitions in ^{87}Rb. In the next several paragraphs we will outline our efforts to characterize the problem and test these possibilities, recalling that we are generally looking for vibrations, fluctuations, and oscillations with a period of about 50 ms (20 Hz) if they shift the position of the trap focus, or some multiple of that frequency for the intensity fluctuations [113]. Additionally, these disturbances must occur over a time scale of several hundred milliseconds.

It is also worth noting that we measured the lifetime of the atoms in the dipole-trap in its new configuration near the bottom of the Hellma cell to be about 5 s. This was substantially lower than the 20 s measured previously during the one-way-barrier demonstration experiments, causing us some concern. In particular, shifting the location of the dipole-trap beam ought to have no effect on the lifetimes, which should depend on the background pressure and the rate of light-induced collision losses. In an effort to improve the lifetimes, we sealed off the rubidium source for a while and ran the Ti-sublimation pump and getters several times. The lifetime showed a modest improvement from about 5 s to 12 s, which may have improved a little more had we purged the chamber longer, though it is not clear how close we would have gotten to 20 s. Additionally, the lifetime data clearly exhibited a slow, linear increase in the distribution widths after the much more rapid increase observed in the first 500 ms, as alluded to earlier. We consider this slow increase in width (about 12 μm/s) a result of the atoms scattering dipole-trap laser light [47], though pointing instabilities in the dipole-trap laser could contribute to this as well [113].

The main concern regarding vibrations of the dipole-laser's fiber arise from the HEPA air filter that is mounted above the optics table in an overhead platform. Though the platform is isolated from the optics table, it supports a metal rod that contacts the fiber, exposing the fiber to vibrations from the filter. The dipole-trap fiber was originally loosely Scotch taped to this metal bar, so we attempted to damp its contact with the bar by inserting some sorbothane for padding and suspending it with a string. This appeared to make the heating worse, increasing the width after 1 s by roughly 60 μm, so we tried turning the HEPA filter off altogether. This made matters worse yet, adding roughly another 15 μm to the width. Subsequent adjustments to the fiber contact never returned the resulting heating back to the levels seen before altering it, and we eventually settled on securing the fiber directly to the metal bar with masking tape (similar to the original arrangement), which produced data closer to what we had initially observed. Additionally, we also tested for transverse vibrations of the fiber by reflecting the beam onto a the edge of a photodetector. We observed no changes in the intensity over the time scales of interest, even when when tapping on the fiber housing, leading us to conclude that transverse vibrations are not a significant heating mechanism.

Next we blocked all sources of stray light from reaching the Hellma cell by shuttering all the lasers and surrounding the entire vacuum chamber with large pieces of cardboard. Unfortunately, this had no impact on the heating effects.

To measure fluctuations in the dipole-trap intensity while the atoms resided in the

dipole-trap, we picked off part of the beam before it entered the beam dump (after exiting the vacuum chamber) and sent it into a photodetector. This allowed us to document any intensity changes actually experienced by the atoms during the various steps of the experiment. We observed distinct, slow fluctuations during the first 2.5 s after turning the dipole-trap on, whose period lengthened from about 20 to 270 ms during that time before finally subsiding. To investigate if these slow fluctuations have any effect on the heating, we turned the dipole trap on during the 7 s MOT-loading time (the MOT loads above the location of the dipole trap, so this did not affect the loading MOT) to ensure these fluctuations had dissipated by the time the atoms were loaded into the dipole trap. This change, however, did not affect the observed heating phenomenon. Incidentally, this also provided a convenient test to determine if heating from the dipole-trap laser expands the fused-silica end of the Hellma cell, shifting the beam waist and focus: turning the dipole-trap laser on several seconds prior loading the atoms into the dipole-trap ensures that any expansion of the fused silica has reached a steady state. These data also confirm that this mechanism is not responsible for the observed heating.

We also examined the power spectrum of our dipole-trap-laser intensity data to look for suspicious frequency components. This analysis uncovered a small, troublesome peak at 40 Hz in the data collected after the atoms were heated via parametric excitation, significant enough to merit concern that it may contribute to the heating effects. The amplitude of this oscillation is quite small compared to the dipole-trap

operating power, however, so it likely does not contribute significantly to the heating. Unfortunately, we were unable to verify this experimentally, as controlling intensity fluctuations at this frequency would require us to implement a feedback-controlled intensity-stabilization scheme that we were not prepared to pursue.

We investigated the effects of the dipole-trap loading and operating power by observing the width of the atomic distribution for center-loaded atoms for all the combinations of $10, 15$, and 19 W loading and operating powers. Figure 5.14 presents the data, which reveal a couple of noteworthy results. First, it appears that the loading power has some influence on the initial temperature of the sample, with higher loading powers yielding warmer atoms. This intuitively makes sense in that at higher loading powers, atoms may enter the trap with larger transverse energies due to the greater trap depth in the radial dimensions, which then couples to the longitudinal dimension. We also observe that the atoms warm at similar rates despite the different loading and operating powers. Though the data indicate that the loading power can affect the initial temperature of the sample, it is not clear that it has any appreciable impact on the subsequent heating.

Our beam-waist measurements for the dipole-trap indicate a spatial profile similar to a Gaussian, though we did not collect any detailed data on the beam profile nor test its stability. As a result, we are unable to establish the existence and examine the effects of this potential heating mechanism.
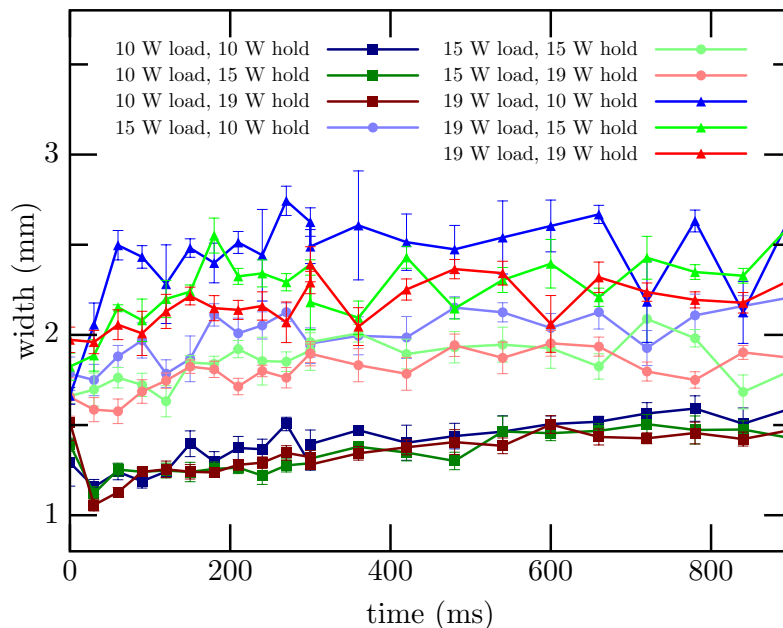
Figure 5.14. The width of the atomic distribution as a function of time for atoms loaded into the center of the trap for the nine combinations of $10, 15$, and 19 W dipole-trap loading powers and $10, 15$, and 19 W dipole-trap operating powers. The error bars represent statistical error for 6 repetitions of the experiment.

We attempted to test for a 6.8 GHz frequency component (the D_2 hyperfine ground state splitting) in the dipole-trap beam using a 25 GHz photodiode and a sampling oscilloscope, but the signal was too noisy to rule out the possibility. A spectrum analyzer would likely be a better tool for this measurement, however at that time we did not have access to one. As a result, we cannot eliminate the possibility that the dipole-trap laser drives transitions between the two ground states, though we acknowledge that the likelihood of this is low.

We conclude that several factors likely contribute to the anomalous heating of the atomic sample observed after completing the sweep, including anharmonic coupling

to the uncooled, transverse degrees of freedom, uncertainty in the overlap of the

dipole-trap focus with the foci of the barrier beams, dipole-trap intensity fluctuations,

scattering of dipole-trap light amplified by light-assisted collisions, and possibly spa-

tial mode fluctuations and non-trivial frequency components in the dipole-trap laser.

CHAPTER VI

CONCLUSION

In summary, we implemented and demonstrated an all-optical one-way barrier with the ability to direct atomic motion and compress the phase-space volume of a sample of neutral alkali atoms. We investigated its response to variations of several key experimental parameters, concluding that the barrier remains quite robust to mechanical and optical changes. We also implemented a novel cooling scheme that involved translating the barrier through a warm sample of atoms and demonstrated its effectiveness at cooling and compressing the atomic sample.

We addressed the limitations of the one-way barrier and the related cooling scheme, noting that the main obstacles stem from an anomalous heating effect and our particular implementation with ^{87}Rb. For this atom, the relatively small ground-state splitting results in an excessive amount of scattering in the presence of the barrier, limiting the trap lifetimes. We also examined several improvements to address the scattering problem, which generally involved increasing the detuning between the main barrier beam and the atomic states.

The future directions of this work are two-fold, with one aspect focusing on mitigating the scattering problem, while the other aspect is more application oriented. Possible avenues for improving the barrier's performance involve implementation

utilizing the fine structure of ^{87}Rb, as well as implementation with a different atomic or (possibly) molecular species. Progress on this front will bolster the application-oriented work, making the one-way barrier a more attractive tool for use in atom-chip technology. Additionally, demonstration of a one-way barrier with a previously uncooled atom or molecule opens the door for applications as a new cooling tool for atoms and molecules not amenable to standard laser-cooling techniques.

BIBLIOGRAPHY

[1] J. C. Maxwell, *A Treatise on Electricity and Magnetism* (1st Ed, Oxford, 1873).

[2] P. N. Lebedev, "The Experimental Study of the Pressure of the Light," *Annalen der Physik* **4**, 29 (1901).

[3] E. F. Nichols and G. F. Hull, "A Preliminary Communication on the Pressure of Heat and Light Radiation," *Physical Review (Series I)* **13**, 307 (1901).

[4] E. F. Nichols and G. F. Hull, "The Pressure Due to Radiation. (Second Paper.)," *Physical Review (Series I)* **17**, 26 (1903).

[5] E. F. Nichols and G. F. Hull, "The Pressure Due to Radiation. (Second Paper.)," *Physical Review (Series I)* **17**, 91 (1903).

[6] D. J. Wineland and H. G. Dehmelt, "Proposed 1014 Delta Upsilon Less Than Upsilon Laser Fluorescence Spectroscopy on T1+ Mono-ion Oscillator Iii," *Bulletin of the American Physical Society* **20**, 637 (1975).

[7] T.W. Hnsch and A.L. Schawlow, "Cooling of gases by laser radiation," *Optics Communications* **13**, 68 (1975).

[8] A. Ashkin, "Trapping of Atoms by Resonance Radiation Pressure," *Physical Review Letters* **40**, 729 (1978).

[9] J. P. Gordon and A. Ashkin, "Motion of atoms in a radiation trap," *Physical Review A* **21**, 1606 (1980).

[10] Steven Chu, "Nobel Lecture: The manipulation of neutral particles," *Reviews of Modern Physics* **70**, 685 (1998).

[11] Claude N. Cohen-Tannoudji, "Nobel Lecture: Manipulating atoms with photons," *Reviews of Modern Physics* **70**, 707 (1998).

[12] William D. Phillips, "Nobel Lecture: Laser cooling and trapping of neutral atoms," *Reviews of Modern Physics* **70**, 721 (1998).

[13] M. H. Anderson, J. R. Ensher, M. R. Matthews, C. E. Wieman, and E. A. Cornell, "Observation of Bose-Einstein Condensation in a Dilute Atomic Vapor," *Science* **269**, 198 (1995).

[14] K. B. Davis, M. O. Mewes, M. R. Andrews, N. J. van Druten, D. S. Durfee, D. M. Kurn, and W. Ketterle, "Bose-Einstein Condensation in a Gas of Sodium Atoms," *Physical Review Letters* **75**, 3969 (1995).

[15] C. C. Bradley, C. A. Sackett, J. J. Tollett, and R. G. Hulet, "Evidence of Bose-Einstein Condensation in an Atomic Gas with Attractive Interactions," *Physical Review Letters* **75**, 1687 (1995).

[16] Paul D. Lett, Richard N. Watts, Christoph I. Westbrook, William D. Phillips, Phillip L. Gould, and Harold J. Metcalf, "Observation of Atoms Laser Cooled below the Doppler Limit," *Physical Review Letters* **61**, 169 (1988).

[17] J. Dalibard and C. Cohen-Tannoudji, "Laser cooling below the Doppler limit by polarization gradients: simple theoretical models," *Journal of the Optical Society of America B* **6**, 2023 (1989).

[18] A. Aspect, E. Arimondo, R. Kaiser, N. Vansteenkiste, and C. Cohen-Tannoudji, "Laser Cooling below the One-Photon Recoil Energy by Velocity-Selective Coherent Population Trapping," *Physical Review Letters* **61**, 826 (1988).

[19] Mark Kasevich and Steven Chu, "Laser cooling below a photon recoil with three-level atoms," *Physical Review Letters* **69**, 1741 (1992).

[20] J. Lawall, S. Kulin, B. Saubamea, N. Bigelow, M. Leduc, and C. Cohen-Tannoudji, "Three-Dimensional Laser Cooling of Helium Beyond the Single-Photon Recoil Limit," *Physical Review Letters* **75**, 4194 (1995).

[21] D. W. Keith, M. L. Schattenburg, Henry I. Smith, and D. E. Pritchard, "Diffraction of Atoms by a Transmission Grating," *Physical Review Letters* **61**, 1580 (1988).

[22] O. Carnal, M. Sigel, T. Sleator, H. Takuma, and J. Mlynek, "Imaging and focusing of atoms by a fresnel zone plate," *Physical Review Letters* **67**, 3231 (1991).

[23] T. Sleator, T. Pfau, V. Balykin, and J. Mlynek, "Imaging and focusing of an atomic beam with a large period standing light wave," *Applied Physics B: Lasers and Optics* **54**, 375 (1992). 10.1007/BF00325383.

[24] Philip E. Moskowitz, Phillip L. Gould, Susan R. Atlas, and David E. Pritchard, "Diffraction of an Atomic Beam by Standing-Wave Radiation," *Physical Review Letters* **51**, 370 (1983).

[25] T. Pfau, Ch. Kurtsiefer, C. S. Adams, M. Sigel, and J. Mlynek, "Magneto-optical beam splitter for atoms," *Physical Review Letters* **71**, 3427 (1993).

[26] O. Carnal and J. Mlynek, "Young's double-slit experiment with atoms: A simple atom interferometer," *Physical Review Letters* **66**, 2689 (1991).

[27] David W. Keith, Christopher R. Ekstrom, Quentin A. Turchette, and David E. Pritchard, "An interferometer for atoms," *Physical Review Letters* **66**, 2693 (1991).

[28] Ernst M. Rasel, Markus K. Oberthaler, Herman Batelaan, Jörg Schmiedmayer, and Anton Zeilinger, "Atom Wave Interferometry with Diffraction Gratings of Light," *Physical Review Letters* **75**, 2633 (1995).

[29] David M. Giltner, Roger W. McGowan, and Siu Au Lee, "Atom Interferometer Based on Bragg Scattering from Standing Light Waves," *Physical Review Letters* **75**, 2638 (1995).

[30] G. Santarelli, Ph. Laurent, P. Lemonde, A. Clairon, A. G. Mann, S. Chang, A. N. Luiten, and C. Salomon, "Quantum Projection Noise in an Atomic Fountain: A High Stability Cesium Frequency Standard," *Physical Review Letters* **82**, 4619 (1999).

[31] Masao Takamoto, Feng-Lei Hong, Ryoichi Higashi, and Hidetoshi Katori, "An optical lattice clock," *Nature* **435**, 321 (2005).

[32] Maciej Lewenstein, Anna Sanpera, Veronica Ahufinger, Bogdan Damski, Aditi Sen, and Ujjwal Sen, "Ultracold atomic gases in optical lattices: mimicking condensed matter physics and beyond," *Advances in Physics* **56**, 243 (2007).

[33] B. DeMarco and D. S. Jin, "Onset of Fermi Degeneracy in a Trapped Atomic Gas," *Science* **285**, 1703 (1999).

[34] M. Greiner, C. A. Regal, and D. S. Jin, "Emergence of a molecular Bose-Einstein condensate from a Fermi gas," *Nature* **426**, 537 (2003).

[35] C. Monroe, "Quantum information processing with atoms and photons," *Nature* **416**, 238 (2002).

[36] H. J. Metcalf and P. van der Straten, *Laser Cooling and Trapping* (Springer, 1999).

[37] D. A. Steck, "Quantum and Atom Optics," course notes available online at `http://steck.us/teaching` (2006).

[38] L. Allen and J. H. Eberly, *Optical Resonance and Two-Level Atoms* (Dover Publications, 1987).

[39] Marlan O. Scully and M. Suhail Zubairy, *Quantum Optics* (Cambridge University Press, 2002).

[40] P. D. Lett, R. N. Watts, C. E. Tanner, S. L. Rolston, W. D. Phillips, and C. I. Westbrook, "Optical Molasses," *Journal of the Optical Society of America B* **6**, 2084 (1989).

[41] D. J. Wineland and W. M. Itano, "Laser cooling," *Physics Today* **40**, 34 (1987).

[42] John S. Townsend, *A Modern Approach to Quantum Mechanics* (University Science Books, 2000).

[43] E. L. Raab, M. Prentiss, Alex Cable, Steven Chu, and D. E. Pritchard, "Trapping of Neutral Sodium Atoms with Radiation Pressure," *Physical Review Letters* **59**, 2631 (1987).

[44] C. S. Adams and E. Riis, "Laser cooling and trapping of neutral atoms," *Progress in Quantum Electronics* **21**, 1 (1997).

[45] Steven Chu, J. E. Bjorkholm, A. Ashkin, and A. Cable, "Experimental Observation of Optically Trapped Atoms," *Physical Review Letters* **57**, 314 (1986).

[46] Steven L. Rolston, Christoph Gerz, Kristian Helmerson, P. S. Jessen, Paul D. Lett, William D. Phillips, R. J. Spreeuw, and C. I. Westbrook, "Trapping atoms with optical potentials," in *1992 Shanghai International Symposium on Quantum Optics*, vol. 1726, p. 205 (SPIE, 1992).

[47] Rudolf Grimm, Matthias Weidemller, and Yurii B. Ovchinnikov, "Optical Dipole Traps for Neutral Atoms," in *Advances In Atomic, Molecular, and Optical Physics*, Benjamin Bederson and Herbert Walther, Eds., vol. 42, p. 95 (Academic Press, 2000).

[48] C. J. Myatt, N. R. Newbury, R. W. Ghrist, S. Loutzenhiser, and C. E. Wieman, "Multiply loaded magneto-optical trap," *Optics Letters* **21**, 290 (1996).

[49] K. I. Lee, J. A. Kim, H. R. Noh, and W. Jhe, "Single-beam atom trap in a pyramidal and conical hollow mirror," *Optics Letters* **21**, 1177–1179 (1996).

[50] J. A. Kim, K. I. Lee, H. R. Noh, and W. Jhe, "Atom trap in an axicon mirror," *Optics Letters* **22** (1997).

[51] Carl E. Wieman and Leo Hollberg, "Using diode lasers for atomic physics," *Review of Scientific Instruments* **62**, 1 (1991).

[52] J. C. Camparo, "The diode laser in atomic physics," *Contemporary Physics* **26**, 443 (1985).

[53] Amnon Yariv, *Optical Electronics in Modern Communications* (Oxford University Press, 1997).

[54] K. B. MacAdam, A. Steinbach, and C. Wieman, "A narrow-band tunable diode laser system with grating feedback, and a saturated absorption spectrometer for Cs and Rb," *American Journal of Physics* **60**, 1098 (1992).

[55] D. A. Steck, *Quantum Chaos, Transport, and Decoherence in Atom Optics*, Ph.D. thesis, University of Texas, Austin, Texas (2001).

[56] B. G. Klappauf, *Experimental Studes of Quantum Chaos with Trapped Cesium*, Ph.D. thesis, University of Texas, Austin, Texas (1998).

[57] W. H. Oskay, *Atom Optics Experiments in Quantum Chaos*, Ph.D. thesis, University of Texas, Austin, Texas (2001).

[58] T. Li, *Manipulation of Cold Atoms Using an Optical One-Way Barrier*, Ph.D. thesis, University of Oregon, Eugene, Oregon (2008).

[59] Patrick McNicholl and Harold J. Metcalf, "Synchronous cavity mode and feedback wavelength scanning in dye laser oscillators with gratings," *Applied Optics* **24**, 2757 (1985).

[60] M. de Labachelerie and G. Passedat, "Mode-hop suppression of Littrow grating-tuned lasers," *Applied Optics* **32**, 269 (1993).

[61] M. de Labachelerie, H. Sasada, and G. Passedat, "Mode-hop suppression of Littrow grating-tuned lasers: erratum," *Applied Optics* **33**, 3817 (1994).

[62] Conoptics Inc., "Product Notes, Optical Isolators," `http://www.conoptics.com/Optical-Isolators-Products.html`.

[63] P. G. Pappas, M. M. Burns, D. D. Hinshelwood, M. S. Feld, and D. E. Murnick, "Saturation spectroscopy with laser optical pumping in atomic barium," *Physical Review A* **21**, 1955 (1980).

[64] D. W. Preston, "Doppler-free saturated absorption: Laser spectroscopy," *American Journal of Physics* **64**, 1432 (1996).

[65] G. C. Bjorklund, M. D. Levenson, W. Lenth, and C. Ortiz, "Frequency modulation (FM) spectroscopy," *Applied Physics B* **32**, 145 (1983).

[66] J. J. Arlt, O. Marag, S. Webster, S. Hopkins, and C. J. Foot, "A pyramidal magneto-optical trap as a source of slow atoms," *Optics Communications* **157**, 303 (1998).

[67] A. Camposeo, A. Piombini, F. Cervelli, F. Tantussi, F. Fuso, and E. Arimondo, "A cold cesium atomic beam produced out of a pyramidal funnel," *Optics Communications* **200**, 231 (2001).

[68] James M. Kohel, Jaime Ramirez-Serrano, Robert J. Thompson, Lute Maleki, Joshua L. Bliss, and Kenneth G. Libbrecht, "Generation of an intense cold-atom beam from a pyramidal magneto-optical trap: experiment and simulation," *Journal of the Optical Society of America B* **20**, 1161 (2003).

[69] Rob Williamson, P. Voytas, R. Newell, and Thad Walker, "A magneto-optical trap loaded from a pyramidal funnel," *Optics Express* **3**, 111 (1998).

[70] SG Cox, PF Griffin, CS Adams, D DeMille, and E Riis, "Reusable ultrahigh vacuum viewport bakeable to 240°C," *Review of Scientific Instruments* **74**, 3185 (2003).

[71] K. M. Birnbaum and The Quantum Optics Group, "Ultra-High Vacuum Chambers," (2005). URL http://www.its.caltech.edu/~qoptics/Vacuum/UHV_chambers.pdf.

[72] Y. T. Sasaki, "A survey of vacuum material cleaning procedures: A subcommittee report of the American Vacuum Society Recommended Practices Committee," *Journal of Vacuum Science & Technology A* **9**, 2025 (1991).

[73] A. Mosk, *Tutorial on Experimental Physics of Ultracold Gases* (Wiley-VCH Verlag GmbH & Co. KGaA, 2005).

[74] M. Bernardini, S. Braccini, R. De Salvo, A. Di Virgilio, A. Gaddi, A. Gennai, G. Genuini, A. Giazotto, G. Losurdo, H. B. Pan, A. Pasqualetti, D. Passuello, P. Popolizio, F. Raffaelli, G. Torelli, Z. Zhang, C. Bradaschia, R. Del Fabbro, I. Ferrante, F. Fidecaro, P. La Penna, S. Mancini, R. Poggiani, P. Narducci, A. Solina, and R. Valentini, "Air bake-out to reduce hydrogen outgassing from stainless steel," *Journal of Vacuum Science & Technology A* **16**, 188 (1998).

[75] J. F. O'Hanlon, *A User's Guide to Vacuum Technology* (John Wiley & Sons, Inc., 2003).

[76] M. Fuchs, *Development of a High Power Stabilized Diode Laser System*, Master's thesis, University of Oregon, Eugene, Oregon (2006).

[77] Peter E. Gaskell, Jeremy J. Thorn, Sequoia Alba, and Daniel A. Steck, "An open-source, extensible system for laboratory timing and control," *Review of Scientific Instruments* **80**, 115103 (2009).

[78] Jeremy J. Thorn, Elizabeth A. Schoene, Tao Li, and Daniel A. Steck, "Dynamics of cold atoms crossing a one-way barrier," *Physical Review A* **79**, 063402 (2009).

[79] M. G. Raizen, A. M. Dudarev, Qian Niu, and N. J. Fisch, "Compression of Atomic Phase Space Using an Asymmetric One-Way Barrier," *Physical Review Letters* **94**, 053003 (2005).

[80] A. Ruschhaupt and J. G. Muga, "Atom diode: A laser device for a unidirectional transmission of ground-state atoms," *Physical Review A* **70**, 061604(R) (2004).

[81] A. M. Dudarev, M. Marder, Q. Niu, N. J. Fisch, and M. G. Raizen, "Statistical mechanics of an optical phase space compressor," *Europhysics Letters* **70**, 761 (2005).

[82] Sang Wook Kim and Mahn-Soo Choi, "Decoherence-Driven Quantum Transport," *Physical Review Letters* **95**, 226802 (2005).

[83] A. Ruschhaupt and J. G. Muga, "Adiabatic interpretation of a two-level atom diode, a laser device for unidirectional transmission of ground-state atoms," *Physical Review A* **73**, 013608 (2006).

[84] A. Ruschhaupt, J. G. Muga, and M. G. Raizen, "Improvement by laser quenching of an 'atom diode': a one-way barrier for ultra-cold atoms," *Journal of Physics B: Atomic, Molecular and Optical Physics* **39**, L133 (2006).

[85] A. Ruschhaupt, J. G. Muga, and M. G. Raizen, "One-photon atomic cooling with an optical Maxwell demon valve," *Journal of Physics B: Atomic, Molecular and Optical Physics* **39**, 3833 (2006).

[86] G. N. Price, S. T. Bannerman, E. Narevicius, and M. G. Raizen, "Single-photon atomic cooling," *Laser Physics* **17**, 965 (2007).

[87] A. Ruschhaupt and J. G. Muga, "Three-dimensional effects in atom diodes: Atom-optical devices for one-way motion," *Physical Review A* **76**, 013619 (2007).

[88] A. Ruschhaupt and J. G. Muga, "Control of atomic motion with an atom-optical diode on a ring," *Journal of Physics B: Atomic, Molecular and Optical Physics* **41**, 205503 (2008).

[89] G. N. Price, S. T. Bannerman, K. Viering, E. Narevicius, and M. G. Raizen, "Single-Photon Atomic Cooling," *Physical Review Letters* **100**, 093004 (2008).

[90] J. J. Thorn, E. A. Schoene, T. Li, and D. A. Steck, "Experimental Realization of an Optical One-Way Barrier for Neutral Atoms," *Physical Review Letters* **100**, 240407 (2008).

[91] Ron Folman, Peter Krüger, Donatella Cassettari, Björn Hessmo, Thomas Maier, and Jörg Schmiedmayer, "Controlling Cold Atoms using Nanofabricated Surfaces: Atom Chips," *Physical Review Letters* **84**, 4749 (2000).

[92] R. Folman, P. Krüger, J. Schmiedmayer, J. Denschlag, and C. Henkel, "Microscopic Atom Optics: From Wires to an Atom Chip," *Advances in Atomic, Molecular, and Optical Physics* **48**, 263 (2002).

[93] J. C. Maxwell, *Theory of Heat* (Longmans, Green, and Co., New York, 1871).

[94] Charles H. Bennett, "Demons, Engines and the Second Law," *Scientific American* **257**, 108 (1987).

[95] R. J. Scully and M. O. Scully, *The Demon and the Quantum* (Wiley-VCH, Weinheim, 2007).

[96] Kilian Singer, Selim Jochim, Marcel Mudrich, Allard Mosk, and Matthias Weidemuller, "Low-cost mechanical shutter for light beams," *Review of Scientific Instruments* **73**, 4402 (2002).

[97] J. Dalibard and C. Cohen-Tannoudji, "Laser cooling below the Doppler limit by polarization gradients: simple theoretical models," *Journal of the Optical Society of America B* **6**, 2023 (1989).

[98] S. J. M. Kuppens, K. L. Corwin, K. W. Miller, T. E. Chupp, and C. E. Wieman, "Loading an optical dipole trap," *Physical Review A* **62**, 013406 (2000).

[99] P. S. Julienne and Jacques Vigué, "Cold collisions of ground- and excited-state alkali-metal atoms," *Physical Review A* **44**, 4464 (1991).

[100] P. D. Lett, K. Mølmer, S. D. Gensemer, K. Y. N. Tan, A. Kumarakrishnan, C. D. Wallace, and P. L. Gould, "Hyperfine structure modifications of collisional losses from light-force atom traps," *Journal of Physics B: Atomic, Molecular and Optical Physics* **28**, 65 (1995).

[101] J. D. Miller, R. A. Cline, and D. J. Heinzen, "Photoassociation spectrum of ultracold Rb atoms," *Physical Review Letters* **71**, 2204 (1993).

[102] Alan Gallagher and David E. Pritchard, "Exoergic collisions of cold Na*-Na," *Physical Review Letters* **63**, 957 (1989).

[103] Elizabeth A. Schoene, Jeremy J. Thorn, and Daniel A. Steck, "Cooling atoms with a moving one-way barrier," *Physical Review A* **82**, 023419 (2010).

[104] T. Kuwamoto, K. Honda, Y. Takahashi, and T. Yabuzaki, "Magneto-optical trapping of Yb atoms using an intercombination transition," *Physical Review A* **60**, R745 (1999).

[105] C. C. Bradley, J. J. McClelland, W. R. Anderson, and R. J. Celotta, "Magneto-optical trapping of chromium atoms," *Physical Review A* **61**, 053407 (2000).

[106] J. J. McClelland and J. L. Hanssen, "Laser Cooling without Repumping: A Magneto-Optical Trap for Erbium Atoms," *Physical Review Letters* **96**, 143005 (2006).

[107] K.-A. Brickman, M.-S. Chang, M. Acton, A. Chew, D. Matsukevich, P. C. Haljan, V. S. Bagnato, and C. Monroe, "Magneto-optical trapping of cadmium," *Physical Review A* **76**, 043411 (2007).

[108] H. Hachisu, K. Miyagishi, S. G. Porsev, A. Derevianko, V. D. Ovsiannikov, V. G. Pal'chikov, M. Takamoto, and H. Katori, "Trapping of Neutral Mercury Atoms and Prospects for Optical Lattice Clocks," *Physical Review Letters* **100**, 053001 (2008).

[109] Mingwu Lu, Seo Ho Youn, and Benjamin L. Lev, "Trapping Ultracold Dysprosium: A Highly Magnetic Gas for Dipolar Physics," *Physical Review Letters* **104**, 063001 (2010).

[110] E. Narevicius, S. T. Bannerman, and M. G. Raizen, "Single-photon molecular cooling," *New Journal of Physics* **11**, 055046 (2009).

[111] S. T. Bannerman, G. N. Price, K. Viering, and M. G. Raizen, "Single-photon cooling at the limit of trap dynamics: Maxwell's demon near maximum efficiency," *New Journal of Physics* **11**, 063044 (2009).

[112] S. Balik, A. L. Win, and M. D. Havey, "Imaging-based parametric resonance in an optical dipole-atom trap," *Physical Review A* **80**, 023404 (2009).

[113] T. A. Savard, K. M. O'Hara, and J. E. Thomas, "Laser-noise-induced heating in far-off resonance optical traps," *Physical Review A* **56**, R1095 (1997).

[114] Charles S. Adams, Heun Jin Lee, Nir Davidson, Mark Kasevich, and Steven Chu, "Evaporative Cooling in a Crossed Dipole Trap," *Physical Review Letters* **74**, 3577 (1995).

[115] H. J. Lee, C. S. Adams, M. Kasevich, and S. Chu, "Raman Cooling of Atoms in an Optical Dipole Trap," *Physical Review Letters* **76**, 2658 (1996).

[116] M. Zielonkowski, I. Manek, U. Moslener, P. Rosenbusch, and R. Grimm, "Manipulation of spin-polarized atoms in an optical dipole-force trap," *Europhysics Letters* **44**, 700 (1998).

[117] Vladan Vuletić, Cheng Chin, Andrew J. Kerman, and Steven Chu, "Degenerate Raman Sideband Cooling of Trapped Cesium Atoms at Very High Atomic Densities," *Physical Review Letters* **81**, 5768 (1998).